Internal Transport Barrier in Tokamak and Helical Plasmas

K. Ida[1,2] and T. Fujita[3]

[1]*National Institute for Fusion Science, Toki, Gifu 509-5292, Japan*
[2]*The Graduate University for Advanced Studies, 322-6 Oroshi, Toki, Gifu 509-5292, Japan*
[3]*Graduate School of Engineering, Nagoya University, Nagoya 464-8603, Japan*
(Dated: October 6, 2017)

The differences and similarities of Internal Transport Barrier (ITB) between tokamak and helical plasmas are reviewed. By comparing the characteristics of ITBs in tokamak and helical plasmas, the physics mechanism for the ITB formation and dynamics are clarified. The ITB is defined as the appearance of discontinuity of temperature, flow velocity, or density gradient in radius. From the radial profiles of temperature, flow velocity and density the ITB is characterized by three parameters of normalized temperature gradient, R/L_T, the location, ρ_{ITB}, and the width, W/a and can be expressed by 'weak' ITB (small R/L_T) or 'strong' (large R/L_T), 'small' ITB (small ρ_{ITB}) or 'large' ITB (large ρ_{ITB}), and 'narrow' (small W/a) or 'wide' (large W/a). Three key physics elements for the ITB formation, radial electric field shear, magnetic shear, and rational surface (and/or magnetic island) are described. The characteristics of electron and ion heat transport and electron and impurity transport are reviewed. There are significant differences in ion heat transport and electron heat transport. The dynamics of ITB formation and termination is also discussed. The emergence location of ITB is sometime far inside the ITB foot in the steady state phase and the ITB region shows the radial propagation during the formation of ITB. The non-diffusive terms in momentum transport and impurity transport become more dominant in the plasma with ITB. The reversal of the sign of non-diffusive terms in momentum transport and impurity transport associated with the formation of ITB reported in helical plasma is described. The non-local transport plays an important role in determining the radial profile of temperature and density. The spontaneous change in temperature curvature (second radial derivative of temperature) in the ITB region is described. In addition, the key parameter of internal transport barrier control and future prospects is discussed.

PACS numbers: 52.55.Fa, 52.55.Hc, 52.25.Fi, 52.50.Gj, 52.50.Qt, 52.50.Sw, 52.30.-q

Contents

I. INTRODUCTION

A. Transport in toroidal plasmas

A toroidal plasma confined by a strong magnetic field with torus topology is one of the most promising concept for nuclear fusion reactor in future, because torus topology has no magnetic field connecting to the vacuum vessel and there is no loss channel along the magnetic field except at the plasma edge, In this system, the energy loss from the plasma is perpendicular to the torus surface, which is called magnetic flux surface, and finite gradients of the plasma parameter such as density

and temperature are sustained by the particle and heat flux which is supplied by fueling and heating or nuclear fusion reaction in future device. Therefore the understanding of the relation between particle/heat flux and density/temperature gradient is crucial to give a good prospect for the performance of nuclear fusion reactor in future. This flux-gradient relations between particle, momentum, electron/ion heat flux and density, toroidal rotation velocity, and electron/ion temperature gradient are called as particle, toroidal momentum, and electron/ion heat transport, and have been intensively studied in experiment and theory [1]. Although these transports are not independent, a simple diffusion model for each relation, particle flux vs density gradient, toroidal momentum flux vs toroidal velocity gradient, electron heat flux vs electron temperature gradient, ion heat flux vs ion temperature gradient is adapted for simplicity. The coupling between the transport is considered as additional terms, which are the so-called convection or non-diffusive term of the transport, or is included as a parameter dependence of transport coefficients of diffusion (D), perpendicular viscosity ($\mu_\perp$) and electron thermal diffusivity (χ_e), and ion thermal diffusivity (χ_i).

The radial fluxes of particle (Γ), momentum (P_ϕ), and electron and ion heat transport (Q_e, Q_i) can be expressed with these transport coefficients as

$$\frac{\Gamma(r)}{n} = -\left[\frac{D\nabla n}{n} - V_{conv}\right] \qquad (1)$$

where n is electron density and V_{conv} is convention velocity [2].

$$\frac{P_\phi(r)}{m_i n} = -\mu_\perp \nabla V_\phi + V_{\text{pinch}} V_\phi + \Gamma_\phi^{RS} \qquad (2)$$

where m_i, V_ϕ, V_{pinch} , and Γ_ϕ^{RS} are ion mass, toroidal rotation velocity, momentum pinch velocity, and radial flux due to residual stress [3, 4]. (The perpendicular viscosity ($\mu_\perp$) is often expressed as toroidal momentum diffusivity (χ_ϕ).)

$$\frac{Q_{e,i}(r)}{n} = -\chi_{e,i} \nabla T_{e,i} \qquad (3)$$

where T_e and T_i are electron and ion temperature, respectively. These fluxes are determined by integrating the particle source, S, toroidal torque, T, and heating power to electrons and ions, $P_{e,i}$ per unit volume as

$$\Gamma(r) = \frac{1}{r}\int_0^r r'\left(S(r') - \frac{d[n(r')]}{dt}\right) dr' \qquad (4)$$

$$P_\phi(r) = \frac{1}{r}\int_0^r r'\left(T(r') - \frac{d[m_i n_i(r')V_\phi(r')]}{dt}\right) dr'(5)$$

$$Q_{e,i}(r) = \frac{1}{r}\int_0^r r'\left(P_{e,i}(r') - \frac{d[n(r')T_{e,i}(r')]}{dt}\right) dr'(6)$$

In general, there are significant contribution of non-diffusive term in particle and toroidal momentum transport. The convection terms in the particle transport can be inward (pinch) or outward (exhaust) by turbulence [2], and the physics mechanism causing non-diffusive term of toroidal momentum transport is complicated [4]. In contrast, the non-diffusive terms of electron/ion heat transport are not so visible, although there were experimental results suggesting heat pinch for electron transport [5, 6]. When the density, velocity, and temperature gradient become large due to the decrease of the diffusion coefficient, D, viscosity, $\mu_\perp$, and thermal diffusivity, $\chi_{e,i}$, the region in the plasma is called transport barrier. Although the increase of the gradients results from the reduction of transport coefficients due to the change in turbulence amplitude and phase, the direct measurements of these transport coefficients from turbulence amplitude and phase are extreamely challenging in experiment especially for the viscosity, $\mu_\perp$, and thermal diffusivity, $\chi_{e,i}$. Therefore, the transport coefficients are derived from the ratio of the radial flux determined with the equations of (4), (5), and (6) and the gradients measured using the equations of (1), (2), and (3) in experiment. This is in contrast to the transport coefficients directly calculated from the gradients in the theory and simulation (the radial flux is the output not the input of simulation). Many varieties of plasmas with an internal transport barrier (ITB) have been discussed in previous review papers [7–10] and the definition of ITB has not been unified because of its variety. In this review paper, the discontinuity of transport inside the plasma, which results in the discontinuity of temperature or density gradient in radius, is used to define the ITB plasma.

B. Edge transport barrier

The edge transport barrier (ETB) is characterized by the abrupt reduction of thermal diffusivity near the plasma edge. Because the reduction of edge thermal diffusivity contributes to the formation of sharp temperature and density gradients at the plasma edge, which is called pedestal structure, the plasma kinetic energy significantly increases associated with the formation of ETB. Therefore the abrupt reduction of edge thermal diffusivity is called as the transition from low confinement mode (L-mode) to high confinement mode (H-mode) [11, 12]. The radial electric field was found to play an important role in the transition from L-mode to H-modes [13, 14] and the turbulence suppression by the $E \times B$ shear, so-called radial electric field (E_r) shear, was recognized to be the most important mechanism for the transition [15, 16].
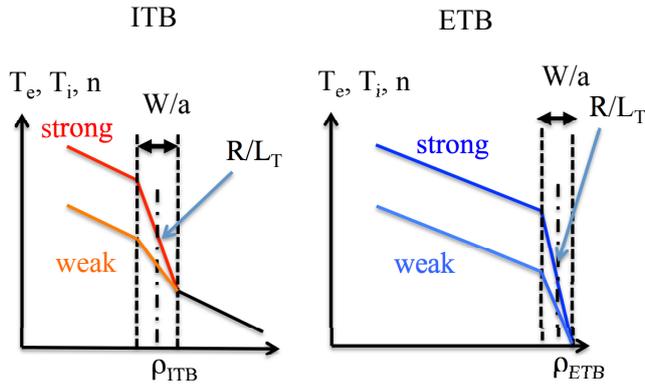
FIG. 1: Radial profiles of density and temperature in the plasma with (a) internal transport barrier (ITB) and (b) edge transport barrier (ETB). Here W/a is ITB and pedestal width, ρ_{ITB} and ρ_{ETB} is normalized minor radius of ITB and ETB region, respectively and R/L_T is normalized temperature gradient.
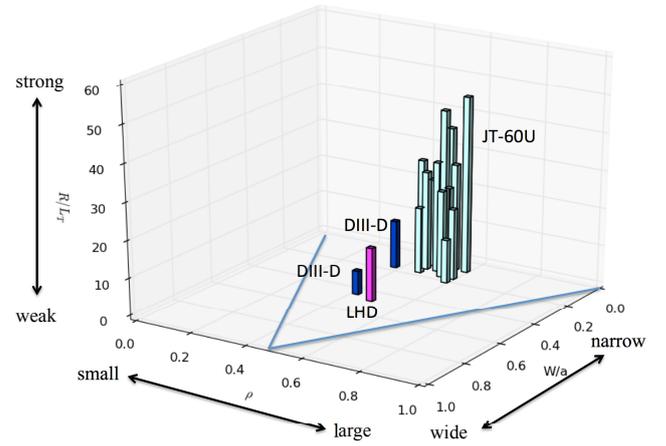

FIG. 2: Normalized temperature gradient, R/L_T, in the parameter space of the ITB location (ρ_{ITB}) and ITB width (W/a) as defined in figure 1(a).

In the L-mode plasma, the thermal diffusivity increases as the temperature and its gradient are increased. Because of the contribution of pressure gradient to the radial electric field, the radial electric field becomes larger as the temperature gradient is increased. Then the larger radial electric field and its gradient contribute to the suppression of turbulence, reduction of thermal diffusivity, and further increase of temperature gradient for given heat flux. Because of this strong feedback process the thermal diffusivity becomes smaller even with higher temperature gradient during the formation of pedestal after the transition from L-mode to H-mode. This feedback process has been recognized to be a key physics mechanism to explain the simultaneous increase of radial electric field and pressure gradient after the L to H-mode transition.

C.   Internal transport barrier

The radial profile of the plasma with ITB is characterized by three parameters of normalized temperature gradient, R/L_T, the location, ρ_{ITB}, and the width, W/a as seen in figure 1. Here R, a, and ρ are major radius, minor radius, and normalized averaged minor radius of the toroidal plasmas, respectively, and L_T is a scale length of temperature gradient defined by $-T/\nabla T$. When the discontinuity of temperature gradient is large enough the shoulder normalized minor radius, $\rho_{shoulder}$ and the foot point normalized minor radius ρ_{foot} can be determined by the radial profile of temperature. Then the normalized minor radius width of reduced transport, W/a, is determined by the distance between the shoulder and foot point as ρ_{foot} - $\rho_{shoulder}$ and the location, ρ_{ITB} and ρ_{ETB}, is defined by the center of ITB and ETB region as $(\rho_{shoulder}+\rho_{foot})/2$. When the discontinuity of temperature gradient is small, the shoulder and foot point locations can be determined by studying the sign of the temperature gradient dependence of thermal diffusivity, because the sign becomes negative, $\partial\chi/\partial(-\nabla T) < 0$ only in the reduced transport region of $\rho_{shoulder} < \rho < \rho_{foot}$. In the ITB plasma where there is no clear shoulder observed, the $\rho_{shoulder}$ is set to be zero.

There are wide variations of the width and location where the transport is reduced as $0.1 < W/a < 0.5$ and $0.1 < \rho_{ITB} < 0.6$ in ITB plasma as seen in figure 2. This is because there are various mechanisms which determine the width and location of the reduced transport region in the plasma core. In this review paper, the characteristics of the ITB is expressed by 'narrow' or 'wide', 'small' or 'large', and 'weak' or 'strong'. The ITB plasmas with small or large W/a are expressed by 'narrow' ITB or 'wide' ITB, the ITB plasmas with small or large ρ_{ITB} are expressed by 'small' ITB or 'large' ITB, and the ITB plasmas with small or large R/L_T are expressed by 'weak' ITB or 'strong' ITB. The 'wide', 'large' and medium R/L_T (not too strong) ITB is most preferable from the view point of good confinement, high MHD stability, and weak impurity accumulation [9].

The ITB plasma with large R/L_T is not always good performance as fusion device, because the 'strong' ITB plasma often suffers collapse or termination due to the large pressure gradient which exceeds the MHD stability limit. Moreover, the ITB width tends to be 'narrow' as the ITB becomes 'strong', as seen in figure 2. Therefore, the central temperature in the plasma with 'strong' ITB is not always high and sometimes is comparable to that in the plasma with 'wide', 'large', and 'weak' ITB. In order to optimize the ITB plasma, it is important to understand the physics mechanisms that determine the ITB characteristics (R/L_T, W/a, and ρ_{ITB}).
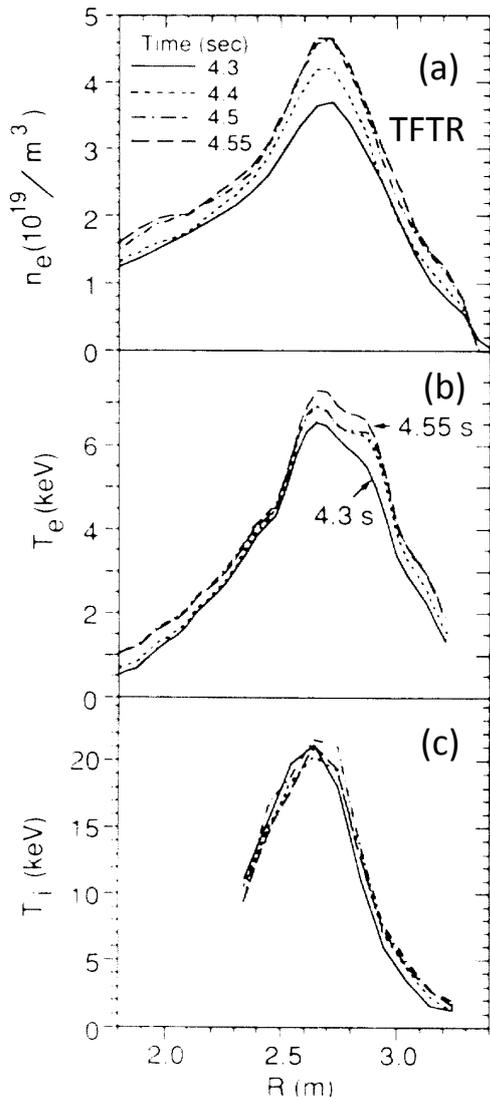
FIG. 3: Radial profile of (a) electron density, (b) electron temperature, and (c) ion temperature in supershot in TFTR (from figure 2(a)(b)(c) in [17]).

FIG. 4: Radial profile of (a) soft x-ray emission in JT-60 and (b) safety factor q profile, and (c) electron pressure in the PEP mode plasma in JET (from figure 4(a) in [18], figure 5(a)(d) in [20]).

D. Discovery of internal transport barrier

Although a density peaking in the plasma with central fueling due to beam fueling or pellet injection was observed in tokamaks in the early 1990s, the formation of internal transport barrier (ITB) was not recognized and the peaking was explained by the improved confinement in the plasma core region [17–20]. Figure 3 shows the radial profiles of electron density, temperature, and ion temperature in the 'supershot' in TFTR. The 'supershot' discharge is characterized by highly peaked density and pressure profile obtained by the core beam fueling with low-recycling environment [17]. The density peaking produced by the core beam fueling results in the confinement improvement similar to the discharge with pellet injection. The global energy confinement time in the 'supershot' is 2.5 times of L-mode and the enhancement factor is comparable to that of H-mode plasma. Therefore, this plasma was recognized as a new confinement mode different from the H-mode. The feature of the transport in the 'supershot' is almost identical to that observed in the 'small' ITB, which was identified subsequently.

Figure 4 shows the radial profile of soft X-ray emission as an indication of electron pressure in the improved confinement mode with pellet injection in JT-60 [18] and radial profiles of safety factor q and pressure in the Pellet Enhanced Performance (PEP) mode in JET [19, 20]. The increase of pressure gradient after the pellet injection clearly suggests the reduction of heat diffusivity only

FIG. 5: Radial profile of (a) particle diffusion coefficient and (d) ion thermal diffusivity and (c) safety factor q in TFTR (from figure 5(a)(b) and figure 2 in [21]).

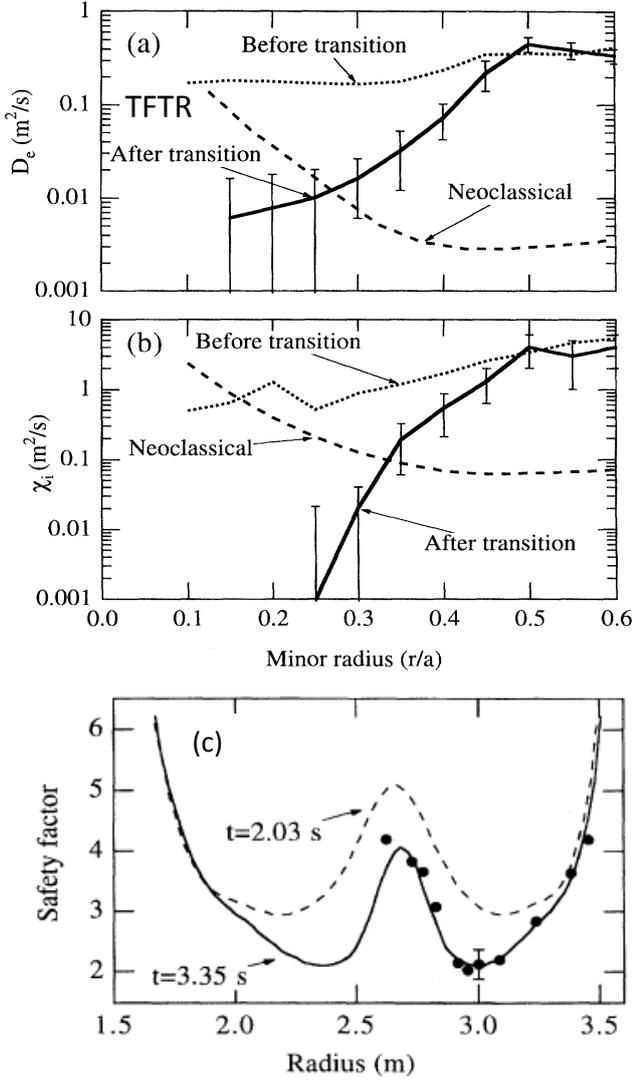FIG. 6: Time evolution of (a) radial profiles of ion temperature, (b) effective of thermal diffusivity at normalized minor radius of 0.7 and (c) the relation between transport barrier location and inverse of effective safety factor in JT-60U (from figure 3(a)(b) and figure 4 in [22]).

in the plasma core region. Although a discontinuity of density or pressure gradient as seen in figure 1 is clearly observed in JT-60 and JET plasma, it is not identified as a foot point of internal transport barrier due to a lack of transport analysis. It should be noted that the relation between the foot point location and q profile is already discussed and the role of rational surface and reversed shear is pointed out. Peaked pressure profile is observed inside the $q = 1$ surface in JT-60 and in the region of reversed shear with $q = 1$ minimum in JET. These plasmas are characterized by the peaked density and temperature profiles with the ITB foot located at $\rho \sim 0.3$ ($q = 1$ rational surface) and are categorized to the 'small' and

'wide' ITB. There are no clear ITB shoulders observed because the ITB region extends to the magnetic axis of the plasma.

Both the particle diffusion and ion heat diffusivity show a significant reduction near the plasma core ($\rho < 0.5$) in TFTR as seen in figure 5(a)(b) [21]. In this discharge, magnetic shear is derived from the the q profiles measurements using motional stark effect (MSE) spectroscopy. As demonstrated in figure 5(c), the negative magnetic is observed only near the magnetic axis and q_{min} locates at $R = 3.0$m ($\rho \sim 0.3$). In this discharge, the

ITB foot appears outside the q_{min} location, which suggests that both negative shear and weak positive shear contribute to the reduction of transport. This improved mode plasma was called enhanced reverse shear (ERS) confinement mode. In this ERS discharge, high poloidal rotation velocity and radial electric field are observed near the $q = 3$ rational surface during the formation of internal transport barrier, which is described in section II-B.

The formation of internal transport barrier was recognized after the finding of abrupt reduction of ion heat diffusivity in the discharge where a clear transition from L-mode to improved mode characterized by peaked ion temperature profile was observed [22]. Sudden increase of ion temperature gradient and reduction of ion thermal diffusivity at the $q = 3$ rational surface were observed in the high beta poloidal (β_p) H-mode discharge in JT-60U as seen in figure 6(a)(b). This is a discharge in which the formation of the internal transport is recognized for the first time. It is important that ITB foot locates at $\rho = 0.5 \sim 0.7$ because the $q = 3$ rational surface locates at larger normalized minor radius than $q = 1$ rational surface. The reduction of thermal diffusivity just inside the foot point ($\rho \sim 0.7$) is extremely large (one-tenth in magnitude of thermal diffusivity). As seen in figure 6(c), the transport barrier location (foot point of ITB) move outward as the edge safety factor q is decreased. It was found that the ITB foot location is consistent with the location where the safety factor q is 3. The ITB plasma observed in this experiment is categorized as 'large' ITB and 'strong' ITB.

The foot point of ITB often appears at the rational surface ($q = 1, 2, 3$) and q minimum location near the rational surface. Therefore, the ITB foot moves depending on the rational surface. The ITB foot appears near the magnetic axis ($\rho \sim 0.3$) for $q = 1$ surface, while it appears further outside ($\rho \sim 0.5$ and $\rho \sim 0.7$) for the rational surfaces of $q = 2$ and $q = 3$. The ITB plasma with the foot point at $q = 1$ surface becomes 'small' ITB, while the ITB plasma with the foot point at higher q values becomes 'large' ITB. Historically, only the 'large' and 'strong' ITB was recognized to be an 'internal transport barrier' and the 'small' and 'weak' ITB was categorized in the core transport improvement.

II. KEY PHYSICS OF INTERNAL TRANSPORT BARRIER FORMATION

In this section the key physics of internal transport barrier formation are discussed. The early experiment on ITB strongly suggests the importance of rational surface and minimum q location in the formation of ITB. There have been many experimental studies that demonstrate the strong impact of safety factor q profile on the formation of ITB. Radial electric field shear can contribute to the suppression of the turbulence and reduction of transport. For the given heat flux, the increase of temperature
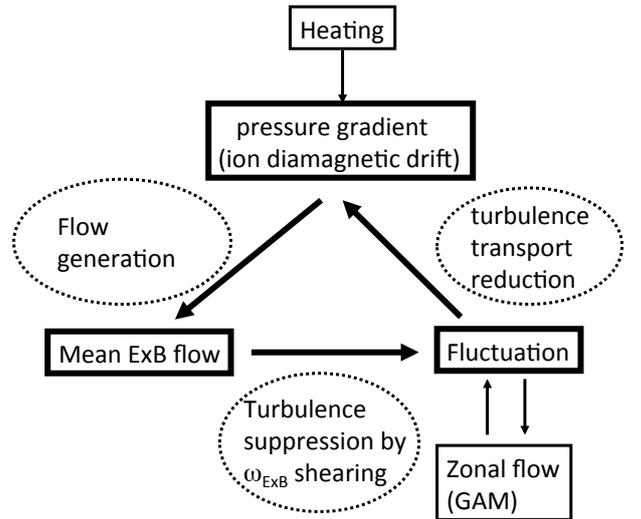

FIG. 7: Feedback process among the $E \times B$ flow, turbulence, and pressure gradient in the transport barrier formation.

and pressure gradient due to the reduction transport then contribute to the increase of radial electric field. Therefore the radial electric field and its shear are the important elements of the feedback process of ITB formation.

A. $E \times B$ shear flow and zonal flow

It is experimentally confirmed that the $E \times B$ flow shear $\partial \omega_{E \times B}/\partial r$, where $\omega_{E \times B} = V_{E \times B}/r$, contributes to the reduction of transport. Therefore, the $E \times B$ flow shear, the fluctuation level, and the ion diamagnetic drift velocity can be important elements of the feedback loop for transport reduction as seen in figure 7. The $E \times B$ flow shear appears near the foot point of ITB and it causes the reduction of fluctuation levels ($\omega_{E \times B}$ shearing effect). As a result, the ion pressure gradient increases in the region where the $E \times B$ flow shear is large enough to reduce the turbulent transport. The increase of the ion diamagnetic drift velocity contributes to the further increase of the $E \times B$ flow. Therefore, either a slight increase of $E \times B$ shearing rates or a slight decrease of linear growth rates for the given temperature gradient can trigger this feedback process. In the L-mode phase, both $E \times B$ shearing rate and linear growth rates are low level in the L-mode plasmas. Once the ITB is triggered, both $E \times B$ flow shear and pressure gradients are simultaneously increased with the condition that $E \times B$ shearing rate exceeds the linear growth rates ($\gamma_{E \times B} > \gamma_{lin}$). Then $E \times B$ shearing rates exceeding linear growth rates can be a cause or a result of the ITB formation depending the trigger mechanism.

$E \times B$ flow shear also plays an important role in the

ITB formation as well as H-mode formation as one of the element of feedback process plotted in figure 7. The change in radial electric field is inferred from the poloidal rotation velocity and motional stark effect (MSE) spectroscopy in the reversed magnetic shear discharge in TFTR [23–25]. Figure 8 shows that the poloidal rotation velocity changes to electron diamagnetic direction, which indicates the strong negative electric field E_r at the transition from L-mode to the enhanced revered shear (ERS) mode. This poloidal rotation in the electron diamagnetic direction and the negative electric field appears only transiently at the transition phase when the confinement mode changes to ERS. It is also an important finding that there is no change in poloidal rotation in the reversed shear (RS) discharge where there is no improvement of confinement. As seen in figure 8, the large poloidal rotation velocity shear and radial electric field shear appears just inside the minimum q location and the ITB foot where the carbon density gradient starts to increase. These experimental results indicate the importance of radial electric field shear in the formation of ITB and that the reversed magnetic shear with the minimum q at the rational surface are not enough to trigger the transition to the ITB plasma. The short scale turbulent fluctuations of these plasmas have been investigated with microwave reflectometry in the ERS plasma in TFTR [26]. In the state with better confinement, it has been found that the level of fluctuations is very small throughout most of the region with negative shear.

The role of $E \times B$ flow shear is also confirmed in the experiment in many tokamaks (TFTR [27], JET [28], DIII-D [29] and JT-60U [30, 31]). The linear microturbulence growth rates of the fastest growing (most unstable) toroidal modes with high toroidal mode number are calculated using the GS2 and FULL gyrokinetic codes [32, 33]. The $E \times B$ flow shear rate was found to be close to the linear growth rate of the ion temperature gradient (ITG) modes at the time of barrier formation when compared with several tokamaks [34]. The comparison of the measured poloidal rotation velocity with the prediction by neoclassical theory was also investigated in JET [35]. It was found that the measured poloidal rotation velocities are an order of magnitude higher than the neoclassical predictions for thermal particles in the ITB region. Correlation of density turbulence suppression and reduced plasma transport is observed in the internal transport barrier (ITB) region of JET tokamak.

Correlation of density turbulence suppression and reduced plasma transport was investigated in the internal transport barrier (ITB) region of JET tokamak discharges with optimized magnetic shear [36]. Two stages of turbulence suppression was reported. First, low frequency turbulence and ion transport are reduced across the plasma core by a toroidal velocity shear generated by intense auxiliary heating. Then with the ITB formation, high frequency turbulence and electron transport are reduced locally within the steep pressure gradient region of the ITB. The 75GHz reflectometer cutoff layer
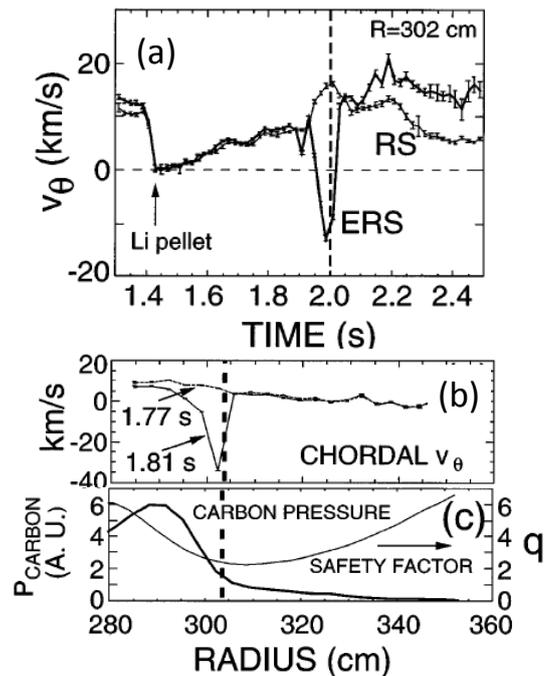

FIG. 8: (a) Time evolution of poloidal rotation velocity for the reversed shear (RS) and enhanced reversed shear (ERS) discharge, and radial profiles of (b) poloidal rotation velocity and (c) carbon pressure and safety factor in the ERS discharge (from figure 1(b) and figure 2(a)(c) in [23]).

was swept through the ITB region to the outboard edge. Figure 9(a)(b) show turbulence spectra inside and outside the ITB region. Fluctuation power inside the ITB region is lower than that outside the ITB region by one order of magnitude. This experiment suggests the following positive feedback loop process in the formation and development of ITB. A significant reduction of high frequency turbulence level inside the ITB region causes an increase of electron and ion pressure gradient, and leads to an increase in the $E \times B$ shear, which contributes to the further reduction of the high frequency turbulence.

The particle flux density evaluated from the simultaneous measurements of density and potential turbulence using a heavy ion beam probe (HIBP) was reported in ITB plasma in CHS Heliotron [37]. Figure 9(c)(d)(e) show an image plot of particle flux density, particle flux density at 60 kHz, and the total particle flux integrated over all frequency up to 200 kHz. The result indicates that the particle flux density from ~ 50 to ~ 100 kHz has the most dominant contribution to the particle transport in both L-phase and ITB-phases and both the particle flux density at 60 kHz and total (< 200 kHz) increase after the back-transition to L-phase. It is an important finding that increase of the particle flux shows the nature of intermittent bursts. These intermittent bursts indicate the Self-Organized Criticality (SOC) behavior [38] rather than the diffusive behavior. These experiments on JET
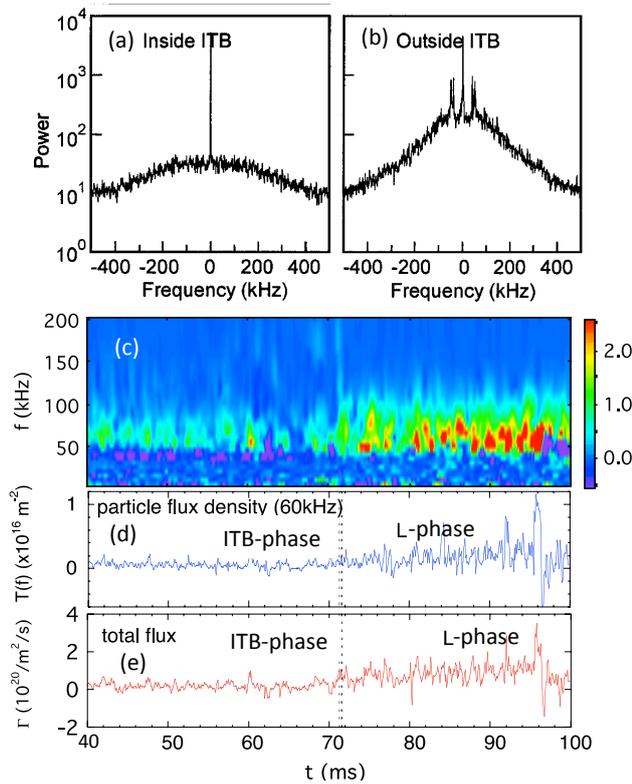
FIG. 9: Density turbulence spectra measured with reflectometer (a) inside ITB and (b) outside ITB in JET, and (c) particle flux density in time and frequency space, (d) particle flux density at 60 kHz, and (e) the total particle flux integrated over all frequency up to 200 kHz measured with HIBP inside the ITB region of $\rho < 0.34$ before and after the back transition from ITB-phase to L-phase in CHS. (From figure 3(c)(d) in [36] and figure 4(a) in [37]).

FIG. 10: Time evolution of (a) density fluctuation and (b) zonal flow amplitude, and (c) the relation between turbulence amplitude and zonal flow amplitude in the plasma with and without ITB in CHS (from figure 31 in [46]).

and CHS demonstrate strong correlation between the turbulence suppression by $E \times B$ shear and the formation of ITB

The theoretical model for the generation mechanism of ITB in the negative magnetic shear was proposed [39]. Negative magnetic shear is theoretically predicted to reduce geodesic curvature drive of micro instabilities, such as the toroidal ion temperature gradient (ITG) driven mode, various trapped particle modes, and high-n ballooning modes. Once these micro instabilities are suppressed, the pressure gradients and poloidal ($E \times B$) flow start to increase. The generation mechanism of this large poloidal flow is one of the important mechanisms in understanding the formation of ITB. This $E \times B$ flow shear reduces the turbulence level by the shear suppression of turbulence. In the transition from the L-mode phase to the ITB phase, a synergism between turbulence suppression by $E \times B$ flow shear and the suppression of the geodesic curvature driven micro instabilities by negative magnetic shear is an important process.

The model is based on the bifurcation of the paral-

lel (or poloidal) viscosity in the plasma where the thermal and fast ion loss are induced by the toroidal magnetic field ripple [40]. The other generation mechanism of $E \times B$ flow is the Reynolds stress. Observation of the generation of $E \times B$ sheared flows via Reynolds stress at the ion Bernstein resonance layer has been reported in TJ-II plasmas [41]. The location of the natural 8/5 resonance coincides with a flattening in the edge plasma profiles and there is a significant variation in the floating and plasma potential just outside the flattening region in TJ-II. This result can be interpreted as an increase of the sheared $E \times B$ flow linked to the radial location of the 8/5 rational surface. These experimental results illustrate the impact of the rational surfaces on the $E \times B$ sheared flows, which could explain the spontaneous formation of transport barriers near the rational surfaces.

Although there are many reports on the relation between the $E \times B$ flow shear and turbulence for ITB plasma, there are few reports on the role of zonal flow

[42, 43] on turbulence suppression and ITB formation. The relation between the zonal flow amplitude and turbulence amplitude was investigated in ITB plasmas in CHS heliotron [44–46]. Figure 10 (a)(b) show a change in density fluctuation amplitude, and a change in zonal flow amplitude before and after a transition at the foot point of ITB. The potential profiles before and after the transition are shown in the insets. The arrow in the left inset indicates the observation point of the fluctuations and zonal flow. The solid vertical line indicates the transition time. It is clearly seen that the zonal flow amplitude suddenly decreases at the back transition from ITB phase to L-mode phase. Figure 10 (c) shows difference in energy partition between zonal flow and turbulence inside the barrier with and without a barrier. The turbulence is normalized by electron temperature gradient in order to remove the effect of the change in the driving force before and after the transition. In the plasma with ITB, the turbulence amplitude is much lower than that in the L-mode (no ITB) and magnitude of zonal flow is larger. This result clearly shows the important role of zonal flow on the suppression of turbulence and formation of ITB. Recently, the second derivative of radial electric field (E_r curvature) was found to play an important role on the suppression of turbulence and reduction of transport rather than the radial electric field shear in the H-mode plasma [47]. The finding of the importance of the radial electric field curvature is a paradigm shift of turbulence suppression mechanism for both ETB and ITB plasmas. Although the $E \times B$ flow shear plays an important role in the formation of ITB because of the feedback process among the $E \times B$ flow, turbulence, and pressure gradient, there is experimental evidence which demonstrates that Ion energy transport is insensitive to reductions in the $E \times B$ flow shear stabilization in the high β_p ($q(0) \sim 4$) plasma [48, 49]. In these discharges, the transport is dominated by the neoclassical ion energy transport even with low $E \times B$ flow shear [50]. These experimental results show the important roles of other mechanisms besides the $E \times B$ flow shear suppression, which is described in the next sub-section.

B.   Role of rational surface on ITB formation

As discussed in the previous section, the location of ITB foot strongly depends on the location of rational surface. The dependence of ITB foot on rational surface is clearly observed in the q scan experiment in JET and ASDEX Upgrade [51]. In JET, lower hybrid heating and current drive (LHCD) was applied before the main heating pulse to modify the q profiles. The results suggest that q profile modification using an LHCD prelude can be useful tool to reduce the heating power level required for the generation of ITB [52, 53]. Figure 11 shows radial profile of safety factor and ion temperature for various ITB plasmas with ITB foot of $q = 1, 2, 3$ [54]. The foot point of ITB is located at the rational surface ($q = 1$,
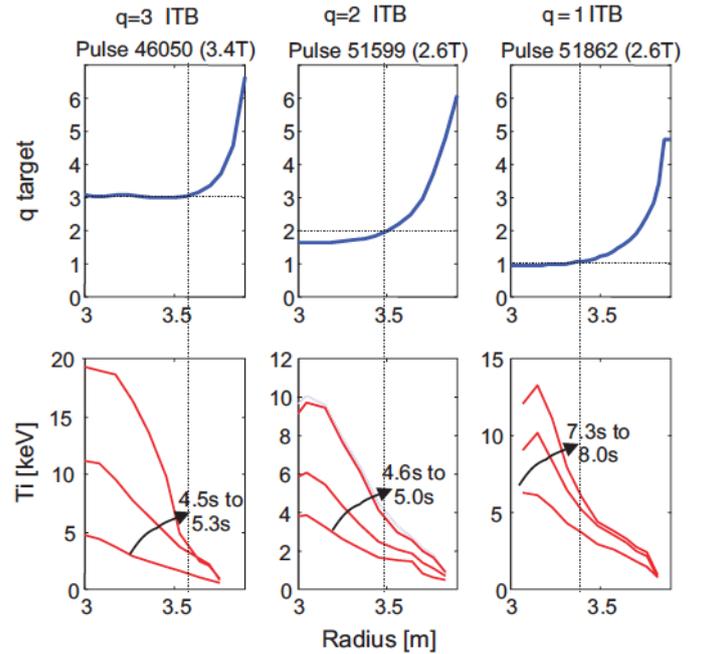

FIG. 11: Radial profiles of safety factor and ion temperature for various ITB plasmas with ITB foot at $q = 1, 2, 3$ in JET (from figure 1 in [54].)

2, and 3) and large temperature gradients are observed inside the rational surface where the magnetic shear is weak. These results also show the importance of rational surface and weak shear in the core for the formation of ITB in tokamaks [55].

The ITB foot of toroidal rotation velocity has been observed inside the rational surface in JT-60U [56] and more recentrly in HL-2A [57] and KSTAR [58]. Both ion temperature and toroidal rotation velocity profiles are peaked in the absence of sawtooth in JT-60U or during the sawtooth oscillation period in HL-2A and KSTAR. These experimental results show the simultaneous reduction of ion heat diffusivity and perpendicular viscosity in the heat and momentum transport, respectively. When the ITBs both in heat transport and momentum transport co-exist, the feedback process between the turbulence suppression due to the flow shear and driving plasma flow by the increase of ion temperature gradient may also play a role.

C.   Minimum q at rational surface (integer q)

There have been many experimental results that demonstrate the significant role of minimum q at the rational surface. The relation between rational surface and access power to the ITB regime has been studied in JET and ASDEX Upgrade [59]. It was found that the emerging time of the ITB in the negative shear plasma is strongly correlated with the minimum q reaching the
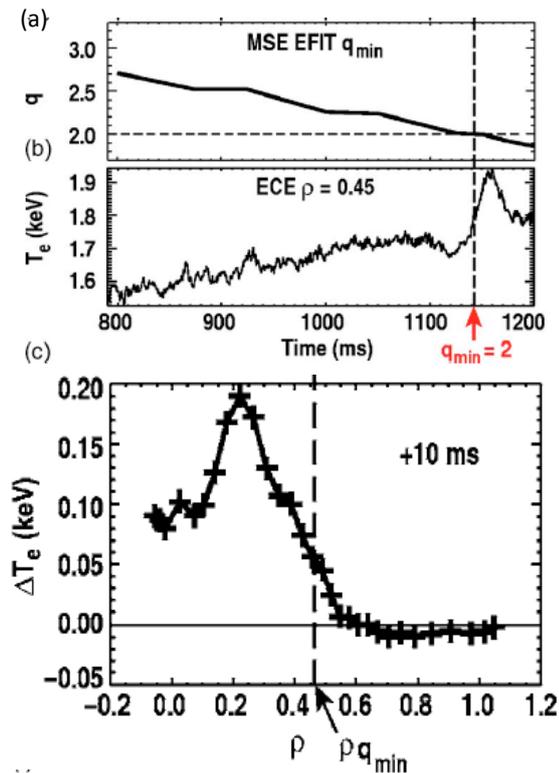
FIG. 12: Time evolution of (a) safety factor, (b) temperature, and (c) radial profiles of increase of electron temperature after the formation of ITB in DIII-D (from figure 2(b)(c) and figure 4(f) in [60].)

FIG. 13: The relation between the transport barrier location in JT-60U (from figure 2(c) in [63]).

integer rather than the input power level.

In experiment, location of ITB where the large temperature gradient appears is found to be strongly correlated to the rational surface. Figure 12(a)(b) shows the time evolution of minimum safety factor q and electron temperature at $\rho \sim 0.45$ in the discharge with reversed magnetic shear in DIII-D [60]. When the minimum q value decreases to 2, the electron temperature shows a rapid increase. The location of the largest temperature gradient often appears just inside the so-called ITB foot. The ITB foot locates at the rational surface both for the normal shear plasma and the reversed shear plasma. In the case of the reversed magnetic shear, the ITB appears when the minimum q crosses the rational surface. After the minimum q cross the rational surface, the large increase of electron temperature appears just inside the minimum q location and decreases of electron temperature gradient at the rational surface as seen in the DIII-D experiment shown in figure 12(c). This result clearly shows the discontinuity of transport at the minimum q location. The global gyrokinetic code simulates this increase of electron temperature gradients [61] and the strong $E \times B$ shear layers appear just interior to the 2/1 singular surface which triggers ITB.
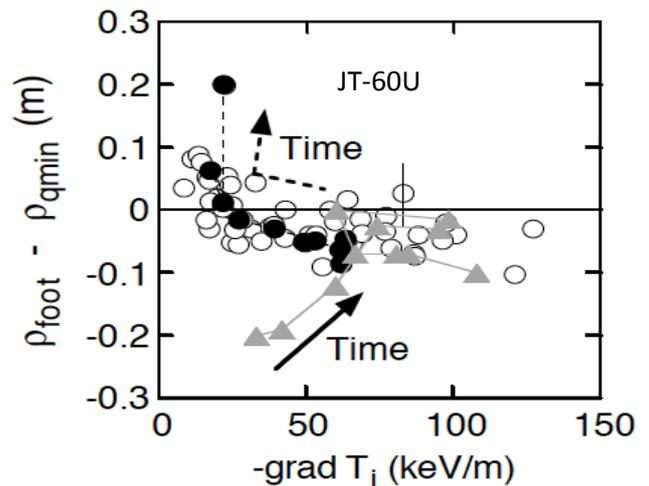
The relation between the foot point of the transport barrier and minimum q location has been studied in JET [62] and JT-60U [63]. Figure 13 shows the difference between ITB foot point location and minimum q location as a function of ion temperature gradient. The ITB foot locations are slightly inside the minimum q location and the differences between two locations are 0.05 of the normalized minor radius for large ion temperature gradients. In some discharges, the ITB foot location can be outside of minimum q location or further inside the minimum q location by 0.2 of normalized minor radius. It should be noted that the distance between ITB foot location and minimum q location changes from negative value to positive value in time, which indicates that the ITB foot location moves outward in time in respect to the minimum q location.

The theoretical study to explain the reduction of transport near the minimum q surface has been developed. The ion temperature gradient (ITG) mode simulation has been applied to the plasma which has minimum q surface [64]. This simulation predicts the suppression of turbulent transport around the minimum q surface due to a discontinuity of the phase relation in the global wave structure across the minimum q and this discontinuity is more efficiently established as flow shear increases and curvature of q at minimum q decreases [65]. More recently the interplay between magnetic shear and resonance at the rational surface was investigated using Hamiltonian model [66].

It should be noted that the abrupt increase of temperature due to the reduction of transport is not always observed only in integer q. The reduction of transport is also observed in half integer q ($q = 3.5$ in JT-60U [67]) and also there is no reduction of transport observed at integer q in similar discharge [68]. This experiment sug-

gests that rational surface itself may not be enough to trigger the transition to ITB phase and additional mechanism is required to explain the observations. One of the candidates for the mechanisms to explain these observations is a small magnetic island, because magnetic island can exist at half integer q location and also magnetic island at the rational surface may disappear by plasma response.

D. Magnetic island

In general, the electron temperature and pressure profile inside magnetic island is flat in the steady state. This is due to the lack of heat flux inside magnetic island and not due to the enhancement of transport. Good particle transport was observed in the plasma where the impurity is accumulated inside the magnetic island in PBX [69] or the pellet is injected into the O-point of magnetic island in JET [70]. The peaked ion temperature due to the low ion thermal diffusivity inside magnetic island was observed after the back transition from H-mode to L-mode phase in JT-60U [71]. The electron cross-field thermal diffusivity at the O-point of magnetic island was investigated in DIII-D [72]. It was reported that the thermal diffusivity is decreased at the O-point at least by a factor of 3 compared to the background plasma. The reduction of turbulence at the O-point of the magnetic island is also reported in DIII-D [73].

The reduction of transport inside magnetic island is clearly observed in the perturbation transport experiment by the slow pulse propagation inside the magnetic island in LHD [74]. More recently the self-regulated bifurcation between slow and extremely slow heat pulse propagation inside magnetic island was reported in DIII-D [75]. These experiments demonstrate that the reduction of transport inside magnetic island, which is evaluated as the effective thermal diffusivity, exceeds an order of magnitude (10 - 40). Because the reduction of transport inside the magnetic island is so large, most of the heat flux concentrates at the X-point and the heat flux which has been treated as flux averaged quantity has a strong poloidal asymmetry. Therefore, the magnetic island could contribute to the increase of local heat flux at X-point above the threshold of the transition from L-mode to ITB.

In order to distinguish the role of magnetic island and rational surface, the resonant magnetic perturbation (RMP) field, which produces $m/n = 2/1$ magnetic island, is applied to the plasma where the heating power is slightly below the threshold power to ITB formation in LHD [76]. Figure 14 shows the time evolution of the electron temperature in the plasma with and without magnetic island produced by RMP. When there is no RMP, the electron temperature increases after the on-axis ECH, and then it saturates in the energy confinement time of 15 ms. However, when the RMP field is applied, the electron temperature keeps increasing after the onset of
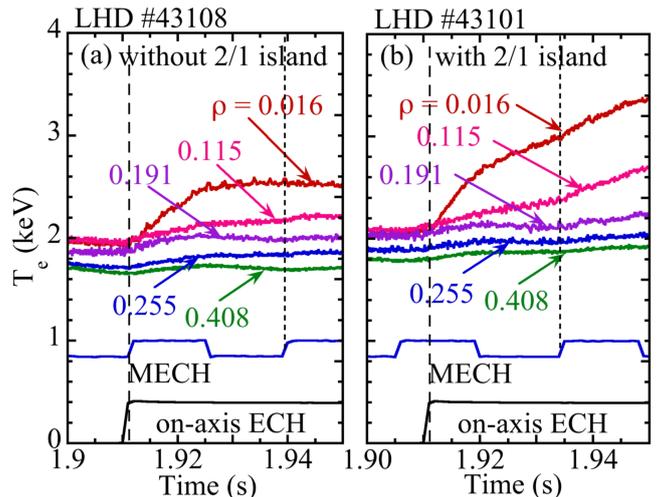

FIG. 14: Time evolution of the electron temperature measured with ECE at various radii for the plasma (a) without a 2/1 island and (b) with a 2/1 island (from figure 7 in [76]).

on-axis ECH, which is a clear indication of the formation of ITB. This RMP experiment in LHD helical plasmas clearly shows that existence of 2/1 magnetic island reduces the threshold heating power for the transition from L-mode to ITB phase. This experiment supports the idea that magnetic island at the rational surface contributes to the transition from L-mode to ITB rather than the rational surface itself.

E. Bootstrap plasma current

Bootstrap current is an important issue in sustaining the ITB plasma in the steady-state. The reversed magnetic shear is initiated by the hollow inductive current at the startup phase of the discharge. Because the hollow current profiles will relax to take the shape of a peaked profile in the steady-state phase, additional plasma current to sustain the hollow current and reversed magnetic shear is necessary. The bootstrap current driven by the steep gradient of pressure in the ITB region could contribute to the sustainment of the reversed magnetic shear [77–80].

The fraction of the bootstrap current can be 80 % of the total plasma current in the high β_p reversed shear plasma in JT-60U [78]. Figure 15 shows radial profiles of ion and electron temperature, safety factor and toroidal plasma current measured. In this discharge, the sharp temperature gradients are observed in the region of reversed magnetic shear and ITB foot locates at $\rho = 0.7$ where the safety factor q has a minimum value. The measured current profile has a peak at $\rho = 0.6$ just inside the minimum q location and the ion and electron tempera-
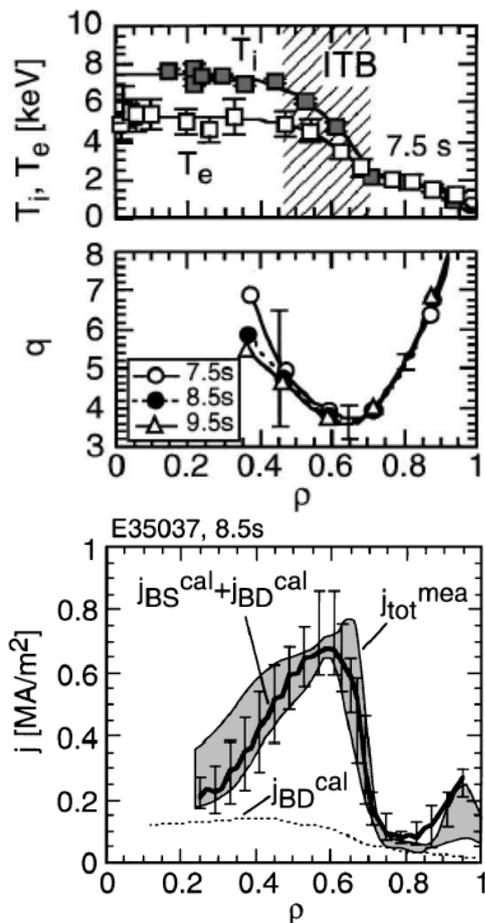
FIG. 15: Radial profiles of (a) ion and electron temperature (b) safety factor q and (c) bootstrap (BS) current and beam driven (BD) current in JT-60U (From figure 4 in [78]).

III. CHARACTERISTICS OF INTERNAL TRANSPORT BARRIERS IN TOKAMAK AND HELICAL PLASMAS

The internal transport barrier is observed both in tokamak and helical plasmas. There are different characteristics between them. In general. the ion transport barrier is most significant in tokamak, while the electron transport barrier is most visible in helical plasmas. The simultaneous achievement of ion and electron heat and particle transport barrier is often observed in tokamaks, while it has not been observed in helical plasmas. In many cases only electron heat, ion heat, or particle transport barrier is observed in helical plasmas. In this section, electron, ion, and particle transport barrier both for tokamak and helical plasmas are discussed. The physics mechanism causing the different characteristics is to be well understood. The magnetic shear is one of the candidates of the mechanism causing the different characteristics of ITB. In general, the magnetic shear is negative in heliotron plasmas, while the magnetic shear can be positive or negative depending on the discharge in tokamak plasmas.

A. Electron internal transport barrier

The strong electron ITB was usually observed in the plasma with reversed magnetic shear in tokamak plasmas [86–88]. Figure 16 is an example of electron ITB in JT-60U NBI heated plasma [86]. Jump of electron density and temperature appears just inside minimum q. The reduction of effective thermal diffusivities of electrons, χ_e sharply drops by a factor of 20 within 5 cm and while the thermal diffusivity of ion, χ_i is smaller than the conventional neoclassical value by a factor of 4 or more. The ratio of electron temperature to ion temperature was ~ 0.7 inside the ITB. The ITB lies in the negative shear region and extended beyond 60 % of the plasma minor radius. Both the ITB foot of electron heat transport and the particle transport locate at ρ of 0.6 just inside minimum q of 3.5. It should be noted that reduced electron heat transport and particle transport are more significant than that in ion heat transport, although the additional heating is NBI alone (no ECH nor ICH). The formation of electron and ion ITB was systematically studied by scanning NBI power and ECH power in JT-60U [87]. In reversed magnetic shear plasmas the electron ITB was observed even with small heating power or small Er shear, while the ion ITB was gradually formed with increase in the heating power. In positive shear plasmas, on the other hand, both the electron ITB and the ion ITB were gradually formed with increase in the heating power. Simultaneous improvement in electron and ion heat transport and particle transport is often observed in NBI-heated tokamak plasmas as will be shown later in the next subsection.

The comparison of electron internal transport barrier between tokamak and helical plasmas was studied in JT-60U tokamak and LHD helical plasmas. One of the sig-

ture gradients have maximum values. The radial profiles of toroidal current measured agree with the sum of bootstrap (BS) current and beam driven (BD) current calculated. In the steady-state phase (t = 8.5 sec), the beam driven (BD) current is peaked with the current density of 0.15 MA/m^2. The bootstrap (BS) current is extremely hollow because of the sharp pressure gradient with the peak current density of f 0.6 MA/m^2. This experiment shows that the shrinkage of reversed shear region was suppressed by the bootstrap current peaked at the internal transport barrier (ITB) layer and that the ITBs at a large radius were sustained The hollow toroidal current and negative magnetic shear are also sustained in the ITB plasma with LHCD in Tore Supra [81], JT-60U [82], and JET [83–85]. The feedback process between the bootstrap current and sharp pressure gradient just inside the ITB region is essential for the sustainment of the ITB.
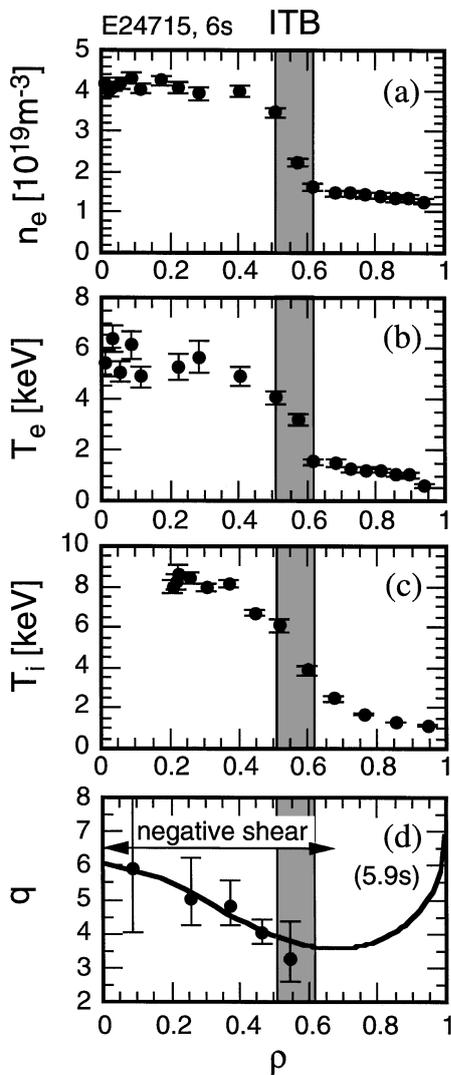
FIG. 16: Radial profiles of (a) electron density (b) electron temperature (c)ion temperature and (d) safety factor q of electron ITB plasma in JT-60U (From figure 3 in [86]).

FIG. 17: Radial profiles of (a) electron temperature, (b) ion temperature, and (c) electron density and rotational transform in LHD (From figure 2(b)(c)(a) in [92]).

nificant differences is a location of ITB foot ($\rho \sim 0.6$ in tokamak and at $\rho \sim 0.3$ in helical). The electron ITB in LHD helical plasma is 'small' ITB, while the electron ITB in JT-60U tokamak is 'large' ITB [89]. The difference in cold pulse propagation shows that electron thermal diffusivity has no temperature dependence in JT-60U tokamak, while it has a negative temperature dependence (thermal diffusivity decreases as the temperature is increased) in LHD helical plasmas [90]. The improvement of electron heat transport is commonly observed in heliotron plasmas [91–99]. Because of the large electron temperature gradients in the ITB region, the transition of neoclassical transport from ion root (small negative electric field) to electron root (large positive electric field) usually occurs simultaneously. Therefore there are two

transport reduction processes in helical plasma: one is a reduction of neoclassical transport due to large positive electric field and the other is a reduction of turbulent transport due to the large electric field shear in the boundary layer between electron root and ion root. Due to the complexity of the transport reduction process, these improved transport in helical plasmas were called as Internal Transport Barrier Triggered by Neoclassical Transport [100], neoclassical internal transport barriers [101–103], and Core electron-root confinement (CERC) [104, 105].

Figure 17 shows radial profiles of electron and ion temperature and electron density and rotational transform ($\iota = 1/q$, where q is the safety factor) with ECH power above the threshold (0.78 MW) and below the threshold (0.58 MW) of the electron ITB plasma in LHD [92]. The profiles of the plasma without additional ECH are also plotted as a reference (indicated with NBI). The central electron density drops slightly due to the poor confinement of perpendicularly accelerated electrons by

ECH (pump out effect) and central Te increases only less than 30 % (from 1.72 to 2.18 keV) for the ECH power of 0.58 MW. However, when the ECH power exceeds the power threshold, the central T_e increases significantly and a large temperature gradient appears near the plasma center at $\rho < 0.3$, while there is little change observed in the profiles in electron density, rotational transform, and ion temperature. Although there is a significant observed increase of T_e, no increases (or even slight decrease) of ion temperature and density are observed in the electron ITB plasma in LHD. These results imply that the turbulence suppression due to the increases of $E \times B$ shear is canceled by the enhancement of a long wavelength turbulence contributing the ion heat transport due to the increase of the T_e/T_i ratio. This observation is in contrast to that in which there are no increases of electron temperature and density in the plasma with ion heat transport barrier, which is discussed in section III-B. Transport analysis shows the clear reduction of χ_e associated with the formation of ITB by a factor of 5 at $\rho < 0.3$, which is consistent with the cold pulse propagation experiment, where the propagation speed of cold pulse is slower inside ITB by a factor of 5) [106]. It should be noted that the formation of the ITB is due to the reduction of the electron heat transport driven by a short wavelength turbulence not due to the neoclassical transport, although the neoclassical transport is reduced by the transition from ion-root to electron root.

The electron ITB is also observed in revised field pinch (RFP) plasma, where the several magnetohydrodynamic (MHD) instabilities cause an enhancement of transport and degrade the confinement performance. Associated with the spontaneous transition from multiple-helicity state to the single helical state, the region with a sharp gradient of electron temperature appears inside the interior of the plasma by increasing plasma current in RFP plasmas [107–109]. Figure 18 shows the reconstruction of the full 2D map of the temperature on the poloidal plane and temperature profile plotted as a function of normalized effective minor radius of ρ in RFX-mod. The 2D map of the electron temperature shows that the hot region is bean-shaped, and centred off the geometric axis, on the resonant surface of the $m/n = 1/7$ mode. The strong gradients marked by the shaded region indicate the formation of a transport barrier at $\rho = 0.25 - 0.45$. It should be noted that there are good agreement between the electron temperature values measured in the opposite side with respect to the helical magnetic axis, which indicates the validity of reconstruction of magnetic flux surface with the single helicity. The spontaneous formation of electron ITB with a single helical state sheds new light on the potential of the RFP configuration.

It is interesting experimental evidence that 1) the formation of ITB often is observed at the low order rational surface or at the integer minimum-q, 2) the existence of magnetic island contributes to the reduction of threshold power for the transition to ITB in helical plasma, and 3) the ITB appears associated with the transition
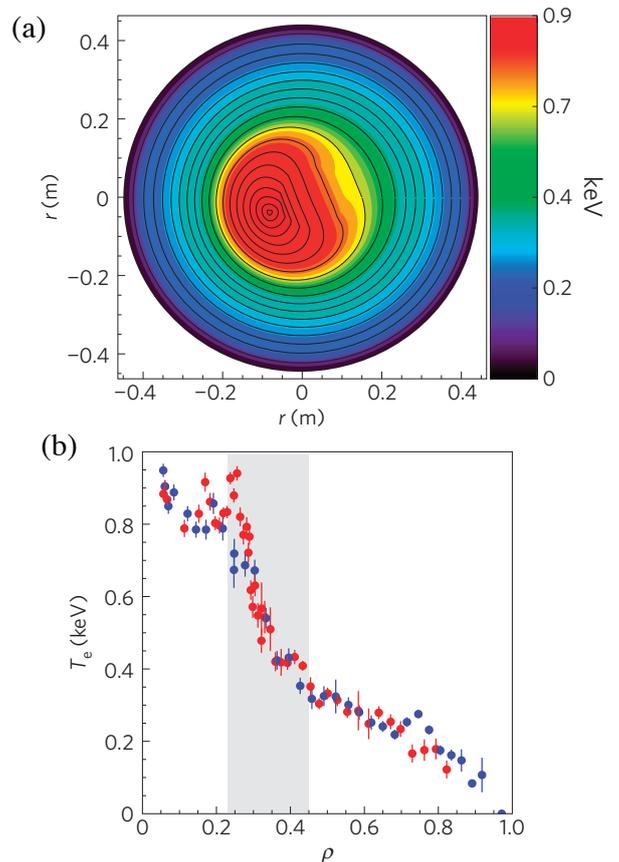
FIG. 18: (a) Reconstruction of the full 2D map of the temperature on the poloidal plane (b) temperature profile plotted as a function of ρ in RFX-mod, where red and blue refer to the two opposite sides with respect to the helical magnetic axis (From figure 3(b)(c) in [107]).

to single helical state in RFP plasma. All these results strongly imply the significant impact of helicity of magnetic topology on the suppression of magnetic and electrostatic turbulence in the plasma and the formation of ITB in toroidal plasma as a common physics mechanism.

B. Ion internal transport barrier

The ion internal transport barrier (ITB) has been widely observed in both tokamak and helical plasmas and various heating methods of ICRH [110–112], and LHCD [113], as well as NBI, which was discussed in section II. The LHCD is also used for q profile control before the strong heating as a prelude of formation of ITB [114]. There are various operation scenarios to trigger the ion internal transport barrier and the some of the names of the ion ITB are given by the scenarios rather than the physics mechanism. In this section, the characteristics of ion transport barrier, especially the relation to the

transport reduction in other transport channels (particle transport, electron transport, and momentum transport), is discussed rather than the scenarios to create the ion ITB plasma. Although the peaked ion temperature and reduction of ion thermal transport are observed in toroidal plasmas (helical and tokamak plasmas), there are clear differences in particle transport between helical plasma and tokamak plasmas.

Figure 19 shows the radial profiles of electron density, electron temperature, ion temperature, and toroidal angular velocity in the ITB plasmas in LHD [97] and DIII-D [115]). The carbon pellet is injected to trigger the ion-TB in LHD. Note that the y-axis for the electron temperature and ion temperature are identical, while the y-axis of electron density and toroidal angular velocity are different between LHD and DIII-D data. In this example, the radial profile of ion temperature is similar between LHD and DIII-D plasma and there is no ITB in electron heat transport in helical and tokamak plasmas [97, 110, 115]. There are significant differences in the radial profile of electron density and also the value of the density. The radial profiles of electron density, ion temperature, and toroidal angular velocity in figure 19(e)(g)(h) indicates clear ITBs of particle transport, ion heat transport, and momentum transport in tokamak. Here the locations of ITB foot locate at the same radii ($\rho = 0.5$). In contrast, only the ITBs of ion heat transport and momentum transport are observed in LHD plasma. In LHD, the discontinuity of ion temperature gradient is smaller than that in tokamak. Therefore, the location of ITB foot in ion heat transport can be identified to be $r_{\mathrm{eff}}/a_{99} = 0.7$ by the change in ion temperature gradient from L-mode phase as seen in figure 19(c). Here r_{eff} is an averaged minor radius and a_{99} is the averaged minor radius where 99 % of kinetic energy is confined inside. The location of ITB foot of momentum transport is found to be close to the plasma edge of $r_{\mathrm{eff}}/a_{99} = 0.8$ as seen in figure 19(d).

There is no ITB of particle transport observed in helical plasmas as seen in figure 19(a) The central electron density of ITB plasma in LHD is much lower than that in DIII-D by a factor of 6∼7 as seen in figure 19(a)(e). In LHD, simultaneous formation of ITB of particle and ion heat transport is not achieved, because the ion ITB usually disappears when the electron density is increased. Because ITB in particle transport and ion transport are simultaneously obtained in tokamak, the central electron density in the ion ITB in tokamak is relatively high. In contrast, the ion ITB is achieved in the low density regime in LHD [116]. The difference in particle transport between helical and tokamak plasmas is one of the mysteries which has not yet been solved.

The other difference between LHD and DIII-D plasmas is observed in the toroidal angular velocity. The toroidal angular velocity of ITB plasma in LHD is much smaller than that in DIII-D by a factor of 6∼7. The small toroidal angular velocity in LHD plasma is not due to the large perpendicular viscosity (momentum diffusivity) but rather to the parallel viscosity in toroidal direction
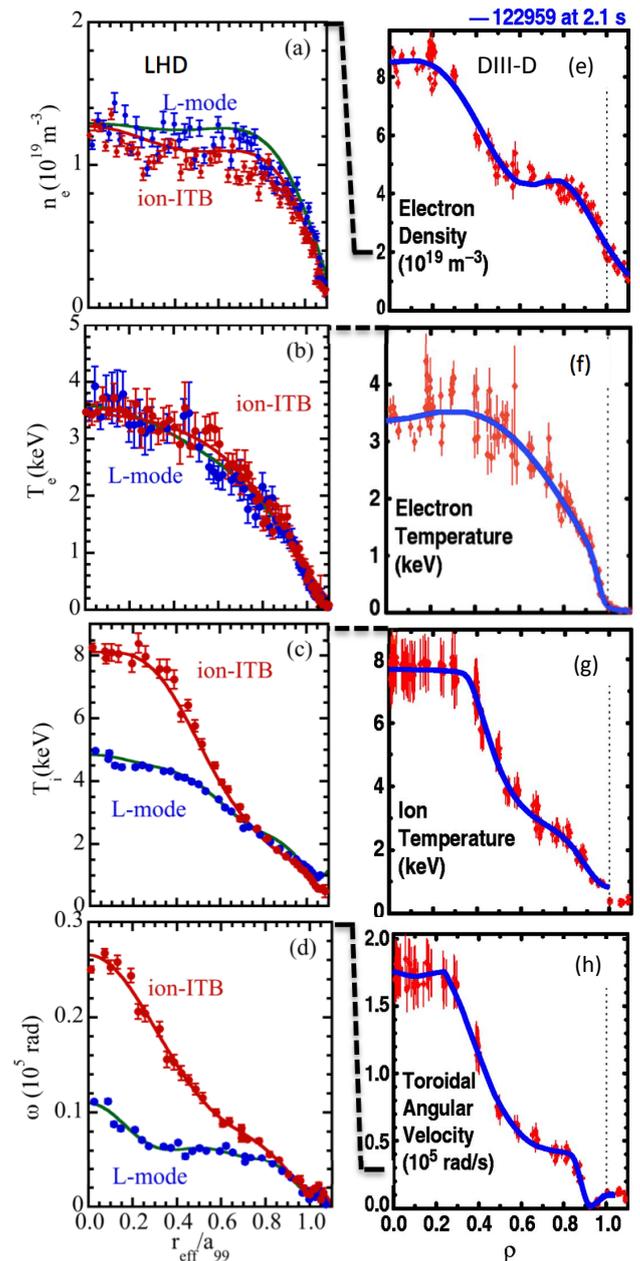
FIG. 19: Radial profile of (a)(e) electron density, (b)(f) electron temperature, (c)(g) ion temperature, and (d)(h) toroidal angular velocity in the L-mode and ion-ITB plasmas in LHD ((a)-(d)) and in the ion-ITB plasma in DIII-D ((e)-(h)) (from figure 4(c)(b)(a)(f) in [115]).

[117, 118] which does not exist in tokamak plasma. The Prantl number evaluated near the magnetic axis, where the damping of ExB flow due to the parallel viscosity is smaller than that perpendicular viscosity, is close to unity in LHD [119]. The increase of toroidal angular velocity in the codirection and its gradients is observed in the ITB
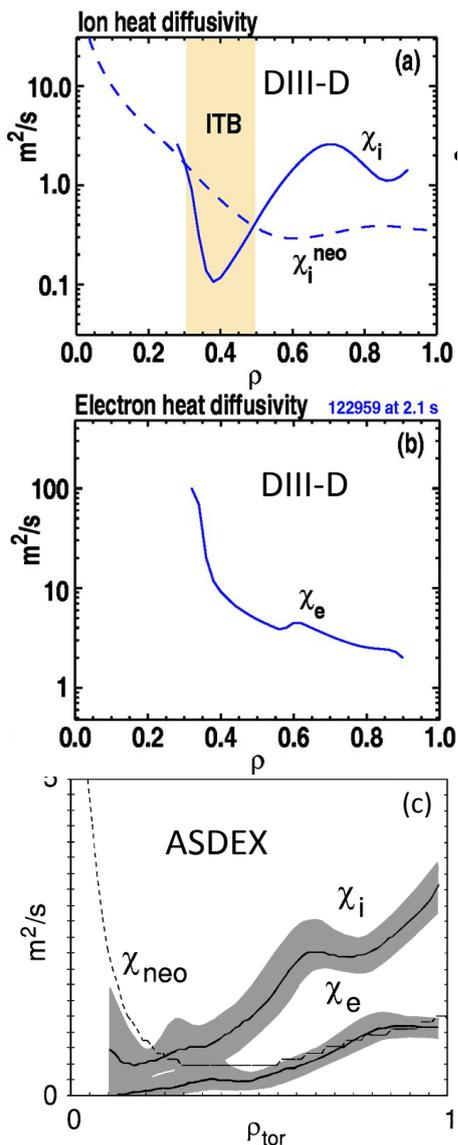
FIG. 20: Radial profile of (a) ion thermal diffusivity and (b) electron thermal diffusivity in the ITB plasma in DIII-D (From figure 6(a)(b) in [115]) and (c) ion and electron thermal diffusivity in the improved H-mode in ASDEX Upgrade (From figure 4 in [121]).

FIG. 21: Radial profile of (a)(b) ion temperature and (c)(d) safety q in the JT-60U plasmas with (a)(c) early ITB formation and (b)(d) delayed ITB formation (From figure 2(b) in [126]).

plasma in LHD and this is due to the increase of intrinsic torque in codirection [120] as well as the reduction of perpendicular viscosity (improvement of momentum transport). It should be noted that the foot point of ion temperature differs from that of toroidal angular velocity.

In tokamak, simultaneous formation of ITBs in electron and ion heat transport are often observed [121–124]. However, in some cases, the reduction of heat transport only in ion channel is observed. Figure 20(a)(b) shows examples of radial profiles of heat diffusivity in the ion ITB plasmas where ITB is observed in only ion transport in DIII-D. The ion heat diffusivity decreases from $\rho \sim 0.7$

going inward and drops below the level predicted by neoclassical theory at $\rho = 0.3 - 0.5$ in DIII-D as seen in figure 20(a)(b) [115]. The reduction of ion thermal diffusivity, χ_i, is observed near the q minimum region at $\rho \sim 0.5$, but the electron thermal diffusivity, χ_e shows a sharp increase towards the magnetic axis. The ion thermal diffusivity drops to the level near or below the standard neoclassical values, which indicates a strong reduction of only ion turbulent transport but not electron transport. In contrast, in the stationary discharges with the improved H-mode with hybrid scenarios, improved confinement for both ion and electron heat transport has been obtained on ASDEX Upgrade [121]. In this discharge, the safety factor q profile is flat in the central region of $\rho < 0.45$ and close to unity, which is just above the threshold of appearance of sawtooth. In this discharge, the plasma χ_i drops to neoclassical values in the central regions, and χ_e is at a low level indicating that the transport reduction is not limited to the ions as seen in figure 20(c).

Although there are many experimental results that suggest the role of integer q minimum in the formation of ITB, the relation of ion ITB location, ρ_{ITB} (see figure 1 for the definition of ITB location) to the q minimum location is unclear and thus is also an interesting topic for study [125, 126]. Figure 21 shows the radial profiles of ion temperature (T_i) and safety factor (q) in two ITB plasmas in JT-60U. Figure 21(a)(c) show the T_i and q profiles in the ITB plasma where the ion ITB locates at the q minimum location. Figure 21(b)(d) show the T_i and q profiles in the ITB plasma where the ion ITB locates at deep inside the q minimum location [126]. In the
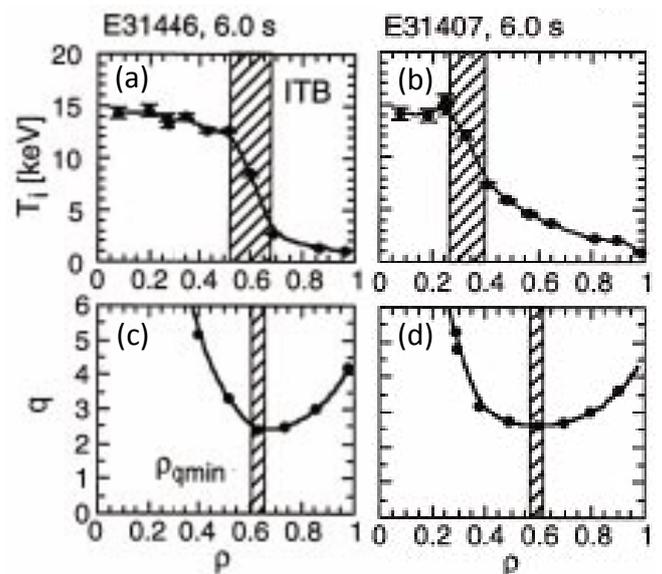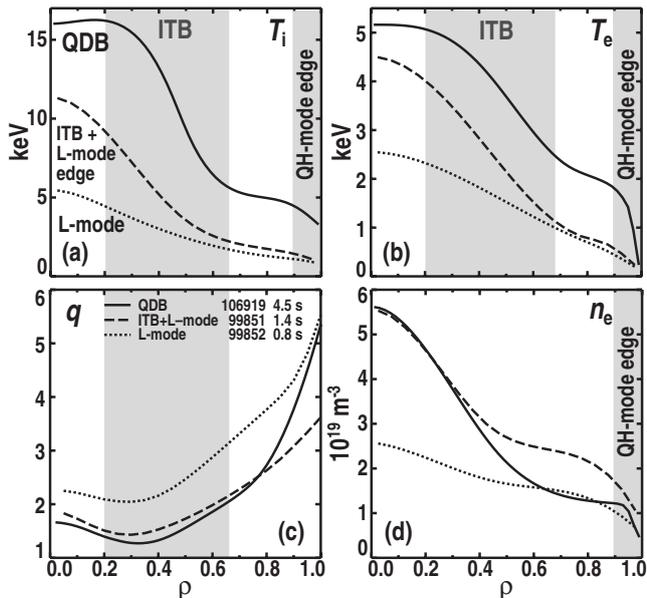
FIG. 22: Radial profile of (a) ion temperature, (b) electron temperature, (c) safety factor q, and (d) electron density in the L-mode, ITB, quiescent double barrier (QDB) plasmas in DIII-D (From figure 2(b) in [131]).

discharge with early ITB formation, the ITB is formed around $\rho = 0.6$ or just inside the q minimum radius. In contrast, the ITB radius is small ($\rho = 0.3$) and far inside the q minimum radius in the discharge with delayed ITB formation.

Here in the discharge with delayed ITB formation, the beam power was reduced to prevent early formation of ITB. This experiment demonstrates that formation of ITB, in particular, the location, is sensitive to the waveform of beam power. Although it is quite an important issue to understand how the location of ITB is determined, it is not clarified yet.

The combination of edge transport barrier (Edge Localized Mode (ELM)-free H-mode or H-mode without large ELM) and ITB was also demonstrated in various tokamak plasmas. The transition from L-mode to H-mode was observed after the formation of ITB plasma in JT-60U [22]. Note that the sudden increase of edge ion temperature is observed at the transition from L-mode phase (I) to H-mode phase (II) in figure 7(a). Simultaneous achievement of ITB plasma and grassy ELM H-mode plasma was also reported in JT-60U [127]. The combination of H-mode and negative central magnetic shear was proposed as one of the high performance scenarios [128] from the point of view to access the second stability regime [129, 130] in the core plasma. Experiments on the DIII-D tokamak have identified a simultaneous formation of transport barrier at interior and edge of plasma,

termed the quiescent double barrier (QDB) regime [131].

Figure 22 shows the radial profile of ion temperature, electron temperature, safety factor q, and electron density in the L-mode, ITB, and QDB plasmas. In the ITB and QDB plasma, the reduction of transport are observed both in ion and electron heat transport. The ITB foot locates at $\rho = 0.65$ which is far outside the q minimum radius of $\rho = 0.35$, which is in contrast to the small radius ITB foot with the delayed ITB formation discharge in JT-60U in figure 21. The QDB regime combines internal transport barriers (ITBs) with a quiescent, edge localized mode (ELM)-free H-mode edge, termed QH-mode, giving rise to separate core and edge transport barriers. In these QDB plasmas ELMs are replaced by continuous benign MHD activity in the edge, which enhances particle transport and retains the density and impurity control in the long-pulse, high-performance H-mode plasmas

Double transport barrier plasmas comprised of an edge enhanced D_α (EDA) H-mode pedestal and an internal transport barrier (ITB) have been observed in Alcator C-Mod [132]. In this discharge, the ITB formation is produced with off-axis ICRF heating locating the wave resonance near $\rho \sim 0.5$ in the Ohmic H-mode discharges with a relatively high density above $\sim 1.4 \times 10^{20} m^{-3}$. The ITB foot is located near $\rho \sim 0.5$, regardless of how the barrier was produced. The formation of the barrier appears in conjunction with a decrease or reversal in the central (impurity) toroidal rotation velocity. In the JFT-2M tokamak, the ITB formation was observed in the high recycling steady (HRS) H-mode regime with the boron coated first wall, regardless of the direction of neutral beams (co-, balanced-, or counter-injection) [133]. The HRS is characterized by good energy confinement ($H_{89P} \sim 1.6$) at a high density ($n_e/n_{GW} \sim 0.7$, where n_{GW} is the Greenwald density), low radiation loss power fraction ($P_{rad}^{main}/P_{in} \sim 0.2$), and the complete disappearance of large ELMs. Accompanying the HRS H-mode transition, the coherent magnetic fluctuations in the frequency range of the order of 10 - 100 kHz with significant variation are seen on magnetic probes on the vessel wall. It is interesting that the combination of edge and interior transport barrier has been achieved by eliminating the large ELM events.

Comparison of ITB plasma in the deuterium target with deuterium neutral beam injection (D-D) plasma and the deuterium target with tritium neutral beam injection (D-T) plasma was performed in JET [134]. The locations of ITBs both in D-D and D-T plasmas are linked to the position of $q = 2$ rational surface at $\rho = 0.4$ and weak magnetic shear inside. The values of ion thermal diffusivity at $\rho = 0.4$ is reduced to the 0.2 m²/s both in the D-D and the D-T ITB plasmas, which is close to the neoclassical level. There are no significant differences in the value of ion thermal diffusivity and the location of ITB foot between D-D and D-T plasmas. The global energy confinement and local thermal transport are analyzed for deuterium and tritium fueled plasmas to quantify their dependence on the average mass of the hydrogenic

ions in the supershot in TFTR [135]. The inferred isotopic scalings of confinement with average isotopic mass $<A>$ was found to be quite strong of $\tau_E \propto <A>^{0.85}$, $\chi_i^{tot} \propto <A>^{-2.6}$, $D_e \propto <A>^{-1.4}$, at fixed injection power. The reason for the difference in JET and TFTR results has not been clarified.

In tokamak, the toroidal ion temperature gradient (ITG) driven turbulence is expected to play a central role in determining the core ion temperature profile because the ion thermal transport produced by toroidal ITG driven turbulence increases very strongly with the temperature gradient after the critical gradient is exceeded. Therefore the formation of ITB is due to the suppression of ITG driven turbulence by $E \times B$ shear in tokamak [123]. After the formation of ion ITB, the trapped electron mode (TEM) turbulence is expected to be more unstable due to the sharp density gradient in the ITB region [136]. However, the formation of ion ITB in helical plasmas is not due to the reduction of ITG driven turbulence by $E \times B$ shear, because ITG mode is expected to be more unstable and the TEM is considered to be stabilized due to the increase of ion temperature gradient and flattening of electron density profile after the formation of ion ITB in LHD [137].

C.   Particle internal transport barrier

The internal transport barrier in particle transport was achieved in the discharge with pellet injection [18–20, 138–141] or with negative magnetic field shear configuration [142] in tokamak and in the discharge with the repetitive pellet injection in helical plasmas [143–145]. Peaked density profiles are also observed in the plasma with weak positive shear with significant beam fueling as seen in TFTR supershot [17], in the high β_p mode plasma in JT-60U [22], and in the ELMy H-mode plasma with flat central q profile ($q(0) \sim 1$) in EAST [146, 147].

Figure 23 shows the radial profiles of electron density, electron temperature in the PEP mode in DIII-D tokamak [140] and IDB-SDC mode with repetitive pellet injection in LHD [145]. Central particle deposition by the pellet is needed for the formation of the PEP-mode on DIII-D. The density profile for the non-pellet ITB comparison is also shown in figure 23 (a). Similar to the ion-ITB plasma, both electron density and ion temperature shows the ITB profiles and q profiles is revered inside the core region of $\rho < 0.5$. This implies that the strong pressure gradient at the ITB in the PEP-mode acts as feedback to maintain the strong negative central shear at the foot of the ITB. Both the ions and electrons have low thermal diffusivities that approach ion neoclassical levels in the core where the strong gradient region exists. In LHD, three neutral beams with a total heating power of ~ 10 MW were injected to heat and sustain the plasma after the repetitive pellets injection. A core region with $\sim 5 \times 10^{20}$ m^{-3} and temperature of 0.85 keV is maintained by internal transport barrier in particle transport
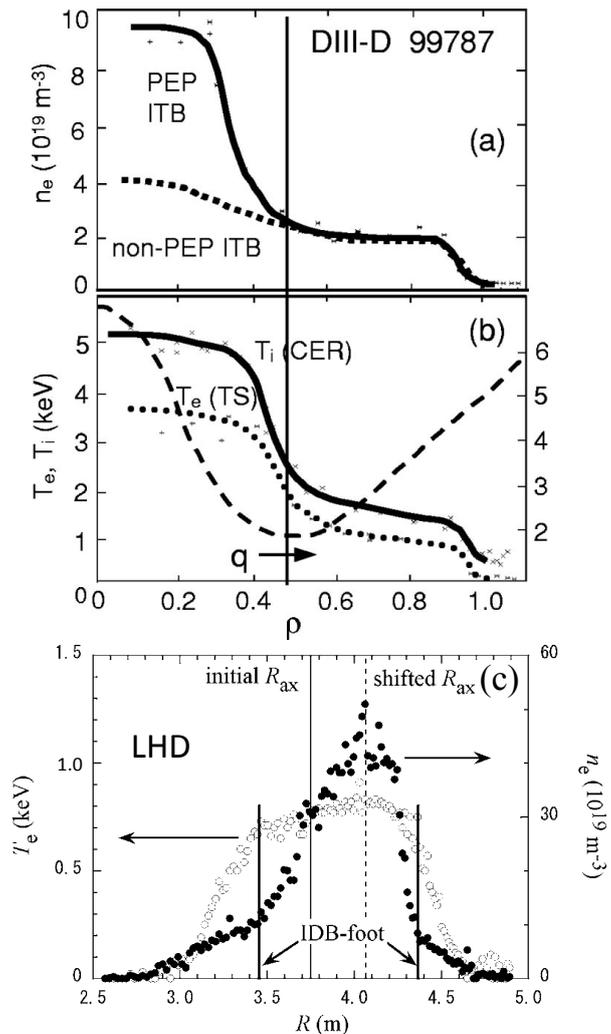
FIG. 23: Radial profile of (a) electron density, (b) electron and ion temperature and safety factor q in PEP mode in DIII-D plasma (figure 6 in [140]) and (c) electron density and temperature in IDB-SDC mode in LHD plasma. (From figure 3 in [145]).

termed internal diffusion barrier super dense core IDB-SDC mode. The density gradient at the IDB at ρ of 0.6 is very high and the particle confinement time in the core region is 0.4 s. Because of the increase in the central pressure, a large Shafranov shift up to 0.3 m is observed. The critical ingredients for IDB formation are a strongly pumped divertor to reduce edge recycling, and multiple pellet injections to ensure efficient central fueling.

There are important differences in characteristics of heat transport inside the particle internal transport barrier between tokamak and helical plasmas. Sharp gradients of both electron density and ion and electron temperature are observed in the mid radius of $0.3 < \rho < 0.5$, which indicates the reduction of particle diffusion and

thermal diffusivity in the PEP mode in tokamak. However, the electron temperature gradient decreases significantly in the core region inside the IDB-foot and only the reduction of particle diffusion is observed in the IDB-SDC mode in helical plasma. No reduction of thermal diffusivity in the high density plasma with pellets is consistent with the fact that ion ITB disappears as the electron density is increased. It is a mystery why there is no simultaneous reduction of particle and thermal diffusivity in helical plasma, which is commonly observed in tokamak plasmas. Further study for the qualitative difference of ITB characteristics between helical and tokamak plasma is important to understand the underlying mechanism of ITB formation in toroidal plasma, which is required for the more precise prospect of ITB characteristics for future devices with nuclear fusion reactions, where thermal ITB without particle ITB is more desirable in order to exhaust the helium ash. The difference in the characteristics of particle transport in ITB plasmas in helical and toroidal plasmas is related to the significant difference in the impurity transport in the ITB plasma, which will be discussed in section V.

IV. DYNAMICS OF INTERNAL TRANSPORT BARRIER

A. Trigger mechanism of internal transport barrier

It is very important to understand the trigger mechanism of internal transport barrier (ITB). There are two possible mechanisms which trigger the formation of internal transport barrier. One is q minimum and the other is the $E \times B$ shear. There is no doubt that both q profiles $E \times B$ shear have important roles in the formation of ITB, as we discussed in section II. However, it is not clear whether these mechanisms always trigger the internal transport barrier, because the $E \times B$ flow is driven by the pressure gradient via neoclassical effect and Reynolds stress, while the q profile is strongly affected by the bootstrap current due to the pressure gradient. Once the increase of pressure gradient starts by the reduction of turbulence, it has positive feedback to further increase through the change in $E \times B$ flow and q profile. Therefore, careful analysis of the formation of ITB is necessary to understand the trigger mechanism of ITB. One of the approaches to study the trigger mechanism is to study the initial state of ITB or weak ITB plasma where the feedback process contribution is small.

The ITB formation experiment in Joint European Torus (JET) demonstrates that ITB can be triggered by the q profile control without increasing the $E \times B$ flow shear. As seen in figure 24(a)(b), there is no ITB formation in the discharge (shot 51611) with monotonic q profile, while the clear ITB is observed at $R < 3.5$m after $t = 5.8$ sec in the discharge (shot 51613) with non-monotonic q profile in JET [148]. There is a clear difference in the radial profile of safety factor q measured with

motional stark effect (MSE) spectroscopy and Faraday rotation as seen in figure 24(c). Both the $E \times B$ shearing rate $\gamma_{E \times B}$ and linear growth rates γ_{lin} calculated by KINEZERO gyro kinetic simulation code are plotted in figure 24 (d)(e). It is reported that the $E \times B$ shearing rates significantly exceeding the linear growth rates γ_{lin} in the core region ($0.3 < \rho < 0.4$) contributed the formation of ITB. However, $E \times B$ shearing rates in the plasma with ITB (#51613) is even lower than that without ITB (#51611). In this plasma, the decrease of the linear growth rates rather than the increase of $E \times B$ shearing rates contributes the formation of ITB. It is also interesting observation that the $E \times B$ shearing rates are comparable to or exceed the $\gamma_{E \times B}$ in the entire region of the plasma both for the discharge with non-monotonic q profiles and with monotonic q profiles as a result of the feedback process described in section II. The reversed magnetic shear has a significant effect on the growth and decorrelation rate and contributes to the decrease of the linear turbulence growth rate, γ_{lin}, and to the increase of the ratio of $\gamma_{E \times B}$ to γ_{lin} as seen in the negative shear region ($\rho < 0.5$) in the plasma with non-monotonic q profile in figure 24(d). This is clear evidence that the q profile was the critical factor for the triggering of an ITB by reducing the growth rate of turbulence rather than increasing the $E \times B$ shearing rate, which is in contrast to the abrupt change in $E \times B$ which triggers the formation of ITB in the ERS discharge in TFTR plotted in figure 12. This observation also contradicts the experimental result indicating that the magnetic shear stabilization cannot be invoked to explain the ITB formation in the hybrid-scenario plasmas with monotonic safety factor profile in JET [149].

Results of stability analysis are presented for two types of plasma with good confinement: internal transport barriers (ITBs) on Tore Supra and the radiative improved (RI) mode on TEXTOR. The stability analysis has been performed with an electrostatic linear gyrokinetic code KINEZERO, evaluating the growth rates of micro instabilities [150]. For Tore Supra experiments, ITBs are found to be triggered by a central negative magnetic shear. The ITBs are then maintained in quasi-steady state (the current density relaxes to a monotonic profile) by an increase of the $E \times B$ shear rate, which exceeds the maximum growth rates. For RI modes in TEXTOR, the impurity seeding is globally stabilizing and thus triggers the improvement. Once the improved confinement is triggered, the simultaneous increases of temperature and density gradients imply an increase in both the growth rate and the $E \times B$ shearing rate. The $E \times B$ shear is found to be high enough to maintain an improved confinement through the stabilization of the large scale modes.

The comparison of the experimental observation with the calculation results with the time dependent transport codes PION-T [151], TRANSP [152], and Weiland transport models [153] has been performed. There are also various theoretical model and quasilinear simulation
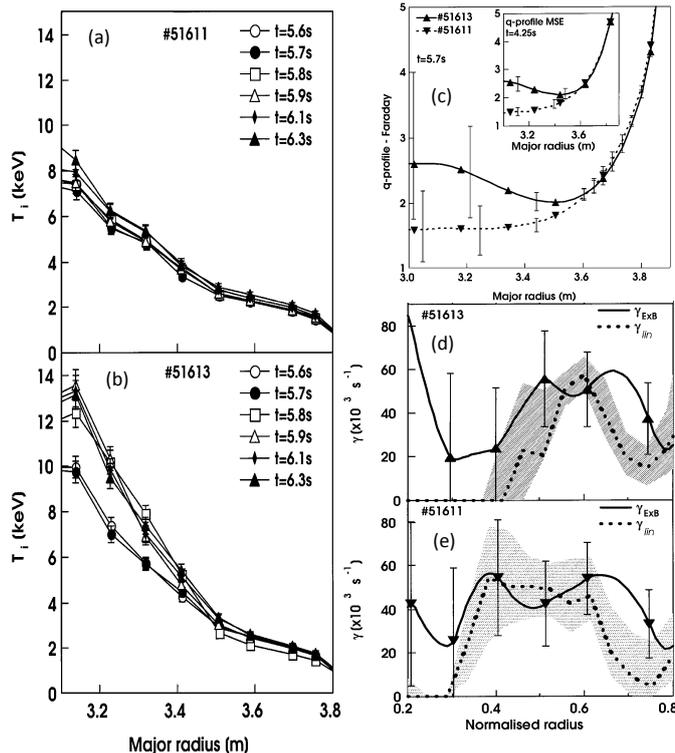
FIG. 24: Radial profiles of ion temperature in the plasma with (a) monotonic and (b) non-monotonic q profile, and (c) q profile for these two plasma and linear growth rate calculated by KINEZERO gyro kinetic simulation code for the plasma with (d) non-monotonic and (e) monotonic q profile in JET. (From figure 2, figure 4(b)(c) and figure 3 in [148]).

incorporating the nonlinear coupling between the turbulent fluctuations and the sheared radial electric field [154, 155]. A quasilinear simulation demonstrates that the sheared flows induced by the double tearing mode have desirable characteristics (lying just outside the magnetic islands), and sufficient levels required for ITB formation [156]. The strong poloidal flow shear forms and leads to strong $E \times B$ sheared flows at island boundaries in the process of tearing mode development. This may provide a physical understanding of why the ITB foot often appears at the location with integer q. Although this theory suggests that boundaries of an island represent a transport barrier, it is not clear whether there is a magnetic island at the rational surface in experiment. In order to investigate the role of magnetic island in triggering the formation of ITB, the detection of small size magnetic island should be necessary.

B. Dynamics of formation of internal transport barrier: emergence and movement

The formation of transport barriers has been studied through examination of mechanisms which can stabilize plasma turbulence and, thereby, reduce turbulence-driven transport [34, 157, 158]. The dynamic transport study of the formation of ITB, especially the location of the emergence of ITB, gives us insight into the trigger mechanism of ITB. The perturbative transport analysis using cold pulse propagation in the plasma with ITB provides a powerful test for the validation of theoretical transport models [159]. After the discovery of ion ITB in JT-60U, a clear radial outward propagation of ITB was observed in the time variation of ion temperature profile. It was already pointed out that this dynamic behavior yields clues to the mechanisms for ITB formation because regions of improved confinement are produced in succession [160]. Figure 25 shows the time evolution and radial profile ion temperature in the high β_p ITB in JT-60U [160] and time evolution and radial profile of ion temperature in the weak magnetic shear ITB in JET [161]. When the NBI power is just above the threshold value for the ITB formation in JT-60U, the steep ion temperature gradient appears near the magnetic axis at $\rho = 0.2$ and propagates to mid radius of $\rho = 0.45$ with the propagation speed of 0.3 m/s. However, in other discharges, a prompt ITB formation at $\rho = 0.6 - 0.7$ was observed in JT-60U. The radial propagation of steep ion temperature gradient is also observed in JET with the propagation speed of 0.1 m/s.

Figure 26 shows the time evolution of the ion temperature gradient at various normalized radii and the contour of ion temperature gradient in time and normalized minor radius of normal magnetic shear ITB in JT-60U and ion ITB in LHD [162, 163]. The increase of ion temperature gradient at $\rho = 0.39$ appears first and the location of the increase of ion temperature gradient moves outward to $\rho = 0.57$ in normal (positive) magnetic shear in JT-60U. The movement of ITB region is clearly indicated in the contour of ion temperature gradients. The region of large ion temperature gradient is $\Delta\rho = 0.2$ (strong narrow ITB) and relatively constant in time. In contrast, the increase of ion temperature gradient at $\rho = 0.44$ appears first and the location of the increase of ion temperature gradient moves inward to $\rho = 0.17$ in normal (negative) magnetic shear in LHD. The contour of ion temperature gradients shows the expansion of ITB region in time and the region of large ion temperature gradient is $\Delta\rho = 0.5$ (weak wide ITB), which is much larger than that in the ITB in JT-60U. In JT-60U, the ITB location moves outward during the ITB formation both in the normal (positive) magnetic shear ITB and in the strong reversed (negative) magnetic shear ITB (see Fig.27). In contrast, the ITB location moves inward in LHD, while the ITB location moves outward during the ITB formation, regardless of the sign of the magnetic shear in JT-60U. It is a mysteries why the direction of ITB region movement is
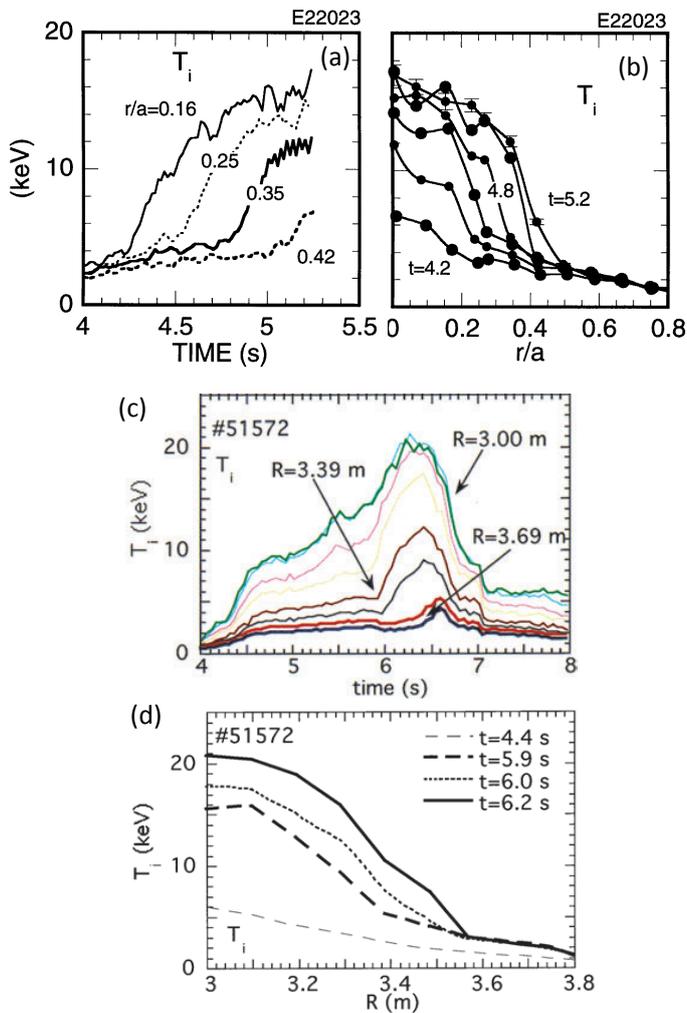
FIG. 25: (a) Time evolution and (b) radial profile ion temperature in the high β_p ITB in JT-60U (from figure 3(a) and figure 1(a) in [160]), and (c) time evolution and (d) radial profile of ion temperature in the weak magnetic shear ITB in JET (From figure 1(b) and figure 5(a) in [161]).

FIG. 26: (a) Time evolution and (b) contour of ion temperature gradients in the normal (positive) magnetic shear ITB in JT-60U (from figure 5(a) in [162]), and (c) time evolution and (d) contour of ion temperature gradients in the ion ITB in LHD (From figure 3(a) in [162], and figure 3(a) in [163]).

opposite between the ITBs in JT-60U and LHD. One of the possible mechanisms for the weak wide ITB in LHD is a large neoclassical ion transport in helical plasma. The large neoclassical transport in helical plasma limit the increase of ion temperature gradient and prevents the formation of strong narrow ITB. In the weak wide ITB, only the moderate reduction of turbulent transport is necessary where the reduced turbulent transport is still higher than the large neoclassical transport.

Figure 27(a)(b) show the time evolution of the ion temperature at various normalized radii and contour of confidence factor for identifying an ITB determined by the normalized ion temperature gradient in JET [164]. Here the confidence factor for identifying an ITB is defined by the probability of the normal distribution with the center of critical dimensionless number and the standard devi-

ation of measurement uncertainty (error bar). Then the confidence factor becomes 50 % when the normalized ion temperature gradient is equal to the critical number and 84.1, 97.7, and 99.9 % when the normalized ion temperature gradient exceeds the critical number by 1, 2, and 3 times of error bar, respectively. The critical normalized gradient, defined as the ratio of ion Larmor radius to scale length of ion temperature gradient (ρ_s/L_T), was chosen to be 1.4×10^{-2} from a discharge ITB with a perfectly

visible barrier whose emergence time was well defined and which was used as a reference. The movement of the ITB foot location outward in time is more significant at the formation of ITB. Figure 27(c)(d) shows the contour of the ion temperature gradient in time and normalized minor radius in JT-60U [163]. This is a discharge with 'narrow' and 'strong' ITB and the temperature gradient reaches 75keV/m, which corresponds to the normalized gradient of 2.4×10^{-2}. The minimum q location moves inward from 0.75 to 0.65 in time. In this discharge, the ITB appears at $\rho = 0.3$, then the maximum ion temperature location moves outward spontaneously with the increase of gradient. When the maximum ion temperature location reaches the minimum q location, the outward movement stops and ITB foot stays just inside the minimum q location.

From these experiments, the location of minimum safety factor, q_{min}, has a strong impact on transport and ITB formation in the plasma with strong reversed magnetic shear regardless of the value of q_{min}. As clearly demonstrated in JT-60U experiment, the outward movement of ITB foot stops at the minimum q location, and the ITB foot point tracks to the q_{min} location in the steady-state phase as seen in figure 10. These results are in contrast to the DIII-D experimental results in the plasma with weak magnetic shear, where the temperature gradient increases when the minimum q cross the rational surface and the JET experimental results in the plasma with positive magnetic shear where the ITB foot locates at the rotational surface as described in section II-C and II-D. These results imply that the rational surface plays an important role in determining the location of ITB foot in the plasma with positive or weakly reversed magnetic shear but not in the plasma with strong reversed magnetic shear. Note that all local transport models fail to explain the movement of ITB region, which requires the abrupt reduction and enhancement of thermal diffusivity when the ITB region moves from inner to outer side of the given radii ($\rho = 0.5$ and 0.58) as seen in figure 27(c). Therefore, the radial propagation of ITB region is strong evidence for the existence of non-locality of transport in the plasma.

The non-locality of transport is considered to exist in the L-mode plasma as well as in ITB plasma. However, it is impossible to detect the non-locality of transport from the power balance transport analysis in the steady state phase because the non-locality of transport is masked by the radial dependence of local transport coefficient. Therefore, the non-locality of transport can be identified by the dynamic transport analysis (flux gradient relation analysis in the transient phase). The simultaneous rise and decay of the electron temperature and temperature gradients in two zones is clear evidence of non-locality of transport [165–167]. By using the dynamic transport analysis, the transient heat diffusivity was evaluated from the flux-gradient relation during the expansion of electron ITB where the electron temperature rise due to the formation of ITB broadens slowly. The transient heat dif-
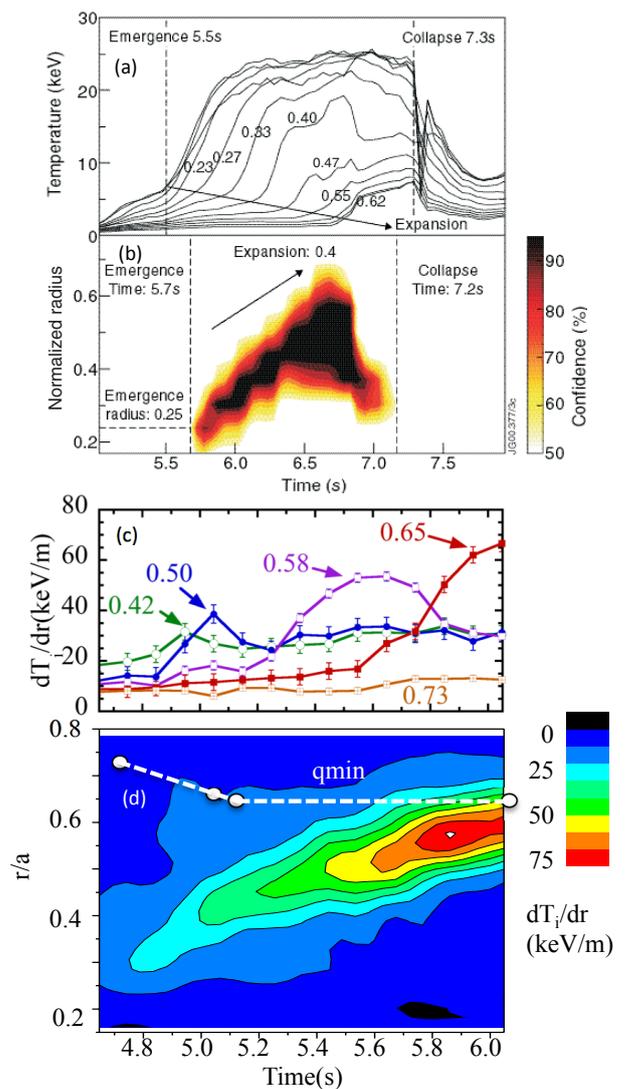
FIG. 27: (a) Time evolution of the ion temperature at various normalized radii and (b) contour of confidence factor for identifying an ITB determined by the normalized ion temperature gradient in strong reversed (negative) magnetic shear ITB in JET (from figure 2 in [164]), (c) time evolution of ion temperature gradient, and (d) contour of the ion temperature gradient in time and normalized minor radius in the strong reversed (negative) magnetic shear ITB in JT-60U (from figure 6(a) in [162] and figure 3(b) in [163]).

fusivity was low and to be 0.1 m^2/s in JT-60U [166]. It should be noted that the heat diffusivity evaluated from this method is transient (it increases again after 60 ms from the onset of ITB) and much smaller than that evaluated from the steady-state power balance analysis by a factor of more than 2 [30]. Similar result was reported in the modulation ECH experiment. The transient electron heat diffusivity evaluated from the heat pulse propagation produced by ECH is larger than that evaluated from the steady state power balance by a factor of 2 - 3 [90].

The abrupt change in heat diffusivity (decrease at the onset of ITB and increases at the onset of ECH) can not be explained by the change in local parameters, because the change of local parameter is slow in the time scale of confinement. These results imply a violation of local closure of the heat transport [168], where the heat diffusivity is not only determined by the local parameters such as temperature gradients, $E \times B$ shear, and magnetic shear.

C. Dynamics of termination of internal transport barrier: collapse event

As the temperature gradient increases due to the formation of ITB, MHD instability becomes strong and at sometimes collapse occurs [169–174]. There are various types of MHD events causing the termination of ITB event. Disruption, snakes, and tearing modes are frequently observed as a trigger of collapse events in JET [170]. The appearance of these types depends on the peaking of ion pressure. In the discharge with very high peaked pressure, the instability leads to the disruption. In the discharge with less peaked ion pressure profile, non-linear perturbation (so-called snake) at the $q = 2$ near the ITB foot location causes the collapse of ITB. The radial extent and inward movement of the snake causes a gradual erosion of the ITB. For even broader pressure profiles, the tearing modes with $n \sim 5$ affect the transport and terminate the high performance. In the case of strong ITB, the multiple harmonic modes with $n = 1$, which are not localized at certain radii, is quite common in JET [171]. In the ITB plasma with H-mode pedestal, large ELM often triggers the ITB collapse [172, 173].

As seen in figure 28(a)(b), the plasma stored energy keep increasing after the formation of ITB during the small type III ELM. The type I ELM starts after the short interval of ELM-free period preceded by type III ELM phase. At the first type I ELM, abrupt decrease of stored energy is observed, which indicates the ITB collapse. This is because when large ELMs occur, strong perturbations δT_e on electron temperature are generated and strong perturbations propagate inward on a ballistic timescale. This propagation is reminiscent of non-local transport experiments. The perturbation induced by large ELMs can reach the ITB because δT_e increases in the vicinity of the ITB before being strongly damped further inside. Such ELMs also lead to a transient increase of T_e gradient at the ITB, which then moves inwards on a diffusive timescale. In Alcator C-mod, MHD activity with m/n = 2/1 mode was observed before the collapse of ITB. As seen in figure 28(c), the rapid increase of soft x-ray emission at 1.2 sec after LHCD turned-on indicates the formation of ITB [174]. This ITB phase ended before LHCD turn-off, with the growth of MHD activity as seen in figure 28(d). The toroidal mode number of this activity was $n = 1$ based on magnetics, and the soft x-ray emission signals show that the mode has an even poloidal
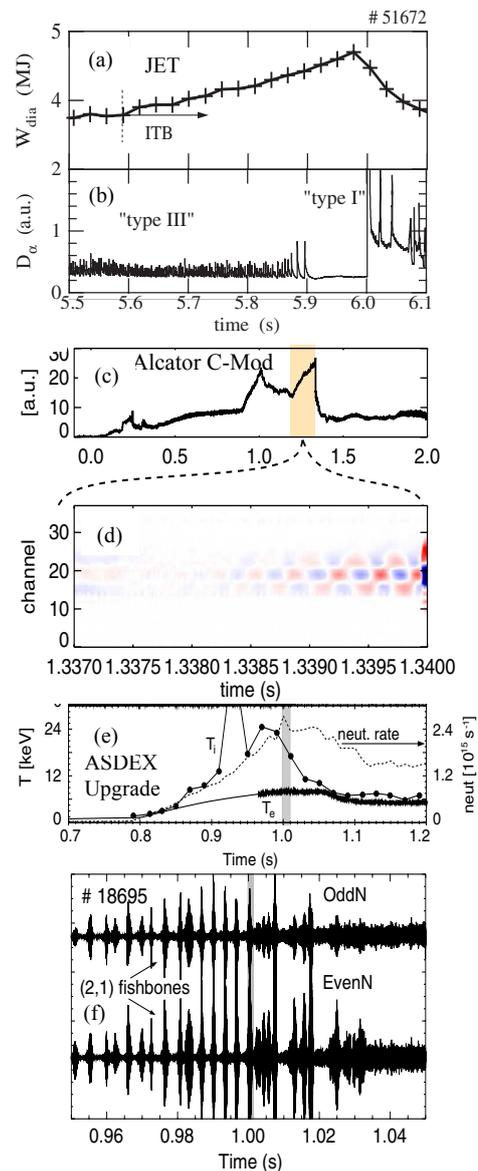
FIG. 28: (a) Time evolution of stored energy measured with diamagnetic loop, (b) D_α signal in JET (from figure 1(a) and (c) in [172]), (c) time evolution of soft X-ray emission, (d) $m/n = 2/1$ mode observed in soft x-ray emission before ITB collapse in Alcator C-Mod (from figure 1(e) and figure 1(f) in [174]), (e) time evolution of the ion temperature, electron temperature, and neutron rate, and (f) MHD activity during the ITB phase in ASDEX Upgrade (from figure 1(b) and figure 6 in [175]).

mode number. Based on the location of the mode and the q profile, this mode is considered to be an $m/n = 2/1$ mode. These experimental observations show the MHD activity causes the termination of ITBs.

However, there are experimental results which show that MHD activity does not impact the ITB collapse. In ASDEX Upgrade, ITBs are observed to collapse after

only several energy confinement times but already before the first type I ELM occurs, and the ELMs are not the cause of the confinement deterioration. Strong MHD activity, usually $m/n = 2/1$ or $3/1$, is found to limit the core energy confinement and ITBs are observed to collapse as seen in figure 28(e) [175]. Figure 28(f) shows MHD activity (fishbones and neoclassical tearing modes) at the beginning of the ITB collapse indicated by the shaded vertical region. In particular, the highest amplitude of MHD activity was observed before the ITB collapses. The MHD activity varies significantly in time due to the rapid increase in the background density and the supra-thermal ion population, and is not correlated to the trigger and termination of ITBs in the ASDEX Upgrade experiment.

V. NON-DIFFUSIVE MOMENTUM AND PARTICLE TRANSPORT IN THE ITB PLASMA

The non-diffusive term of the momentum and particle transport is expected to be more sensitive to the change in turbulence state rather than the diffusive term, because the slight change in the phase relation can change the sign of the non-diffusive term. Therefore, when the internal transport barrier (ITB) is formed, non-diifusive term of momentum transport (intrinsic torque and rotation) and non-diffusive term of particle (inward or outward convection) are expected to change. In this section, how the intrinsic torque and rotation and convection of impurity transport change after the formation of ITB in tokamak and helical plasmas is discussed.

A. Intrinsic rotation in the internal transport barrier plasmas

The intrinsic torque and rotation are commonly observed in ohmic, L-mode, H-mode and ITB plasmas in tokamak and helical plasmas [4]. The residual stress due to the symmetry breaking of turbulence is a strong candidate for the intrinsic torque and rotation [3, 176] and is supported by the experimental result in DIII-D [177]. and ASDEX Upgrade [178, 179]. Therefore, the changes in the intrinsic torque and rotation are good indications for the change in turbulence structure at the transition from L-mode to ITB plasmas.

A large increase of toroidal rotation in the counter direction in the narrow region of ITB is observed in JT-60U, which is called notched V_ϕ profile [63]. Figure 29 shows the radial profiles of ion temperature T_i and toroidal rotation velocity, V_ϕ, of carbon impurities measured by charge exchange spectroscopy, which was obtained by jogging the plasma, which was moved inwards by 0.1 m in 0.1 sec during the quasi-state phase of ITB. A steep ion temperature gradient was formed at half of the plasma minor radius, but becomes flat in the core region. Similar characteristic are observed in the radial
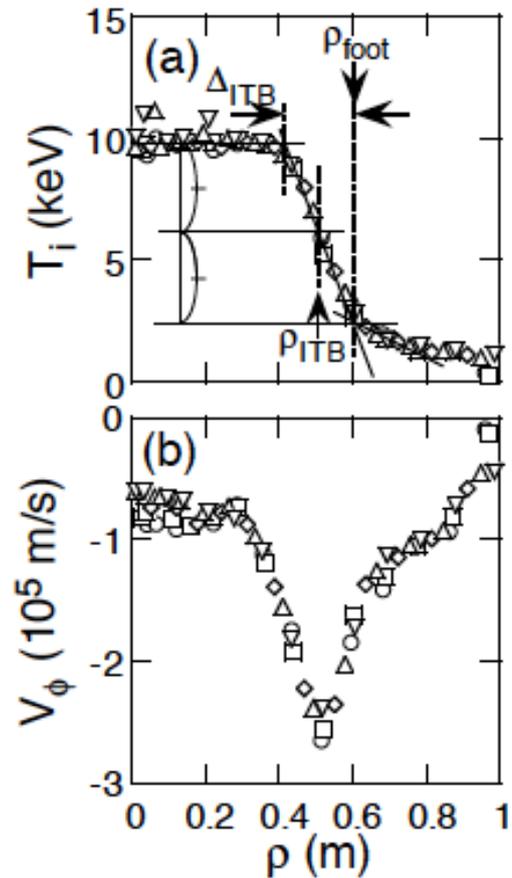

FIG. 29: Radial profiles of (a) ion temperature and (b) toroidal rotation velocity obtained by jogging the plasma in JT-60U. Different symbols indicate different times during this discharge. Here, ITB location, ITB foot point, and ITB width are indicated as ρ_{ITB}, ρ_{foot}, and Δ_{ITBt}, respectively (from figure 1 in [63]).

profiles of electron temperature and density, while the heating deposition profile is peaked at the magnetic axis. The notched feature in the V_ϕ profile was formed near the ITB, which indicates that a substantial radial electric field shear was formed in the ITB layer. The notched profile often appeared in the measured V_ϕ profile of carbon impurities in reversed magnetic shear with ITBs, mainly for balanced momentum injection. This indicates that there are non-diffusive terms in toroidal momentum transport, because the notch structure of toroidal rotation suggests the intrinsic rotation in counterdirection driven by sharp temperature gradient at the ITB region.

There is a difference in toroidal rotation velocity between the bulk ion and carbon impurity as predicted by neoclassical theory. The difference depends on the magnetic field geometry and ion temperature gradient and vanishes at the magnetic axis. Therefore it is important to investigate whether there is a disparity of toroidal ro-

tation due to the spontaneous rotation at the magnetic axis. The time evolution of the radial profiles of toroidal rotation was measured in the beam exchange experiment, where NBI direction is switched from co- to counter- to the plasma current in JFT-2M [180, 181]. It was reported that the non-diffusive term for toroidal momentum transport was increased with the increase of ion temperature gradient and is roughly inversely proportional to the poloidal magnetic field. A good correlation between the intrinsic rotation V_ϕ and the pressure gradient is most significant in the ITB plasma [182].

The intrinsic rotation in the counterdirection is also observed in the ITB plasma with ICRF hearing in Alcator C-Mod [183–187], where the changes both in particle and heat transport are significant as seen in the peaking of electron profiles and soft X-ray brightness as seen in figure 30(a)(b). The formation of ITB starts at t = 0.9 sec and there is continuous peaking both in density and soft X-ray brightness profile until t = 1.2 sec. The time evolution of toroidal rotation velocity plotted in figure 30(c) shows co-rotations in the center and at the off mid-plane (+10.4cm and -10.3cm) start to decrease (accelerated in the counter direction) at the beginning of formation of ITB (t = 0.9 sec) before the significant peaking of electron density and soft X-ray brightness is observed (t = 1.2 sec). Because the rotation velocities above and below the mid-plane show similar behavior, the effect of radial electric field (velocity perpendicular to magnetic field) to the measured rotation velocity is small and the rotation velocity measured mainly reflects toroidal rotation velocity. The large time derivative of toroidal rotation, which indicates that the appearance of intrinsic torque in counter direction, is seen only at the emergence of ITB (t = 0.9 - 0.95 sec). Therefore this experiment clearly demonstrate that the intrinsic rotation in the counter direction is not due to the change in density or temperature profiles (not due to the neoclassical effect) but is due to the appearance of intrinsic torque in counter direction associated with the change in turbulence structure.

In contrast, the intrinsic rotation in the codirection is observed in the ion-ITB plasma in LHD [120, 188], where the ITB structure appears only in ion temperature profile, and not in density and electron temperature profiles. The disparity in the toroidal rotation velocity profiles between co-NBI and counter-NBI discharge becomes weaker in the L-mode plasmas in LHD [189]). The radial profile of the toroidal rotation velocity in the plasmas with the counter-NBI dominant discharge is quite different from the one in the plasmas with the co-NBI dominant discharge. It should be noted that the plasma rotates in the codirection at the half of the plasma minor radius in plasmas with the counter-NBI dominant discharge. The spontaneous toroidal rotation measured with carbon impurity is larger than that predicted with the neoclassical theory by a factor of two, which indicates the significant contribution of spontaneous rotation driven by turbulence.

The radial flux due to the residual stress (third term
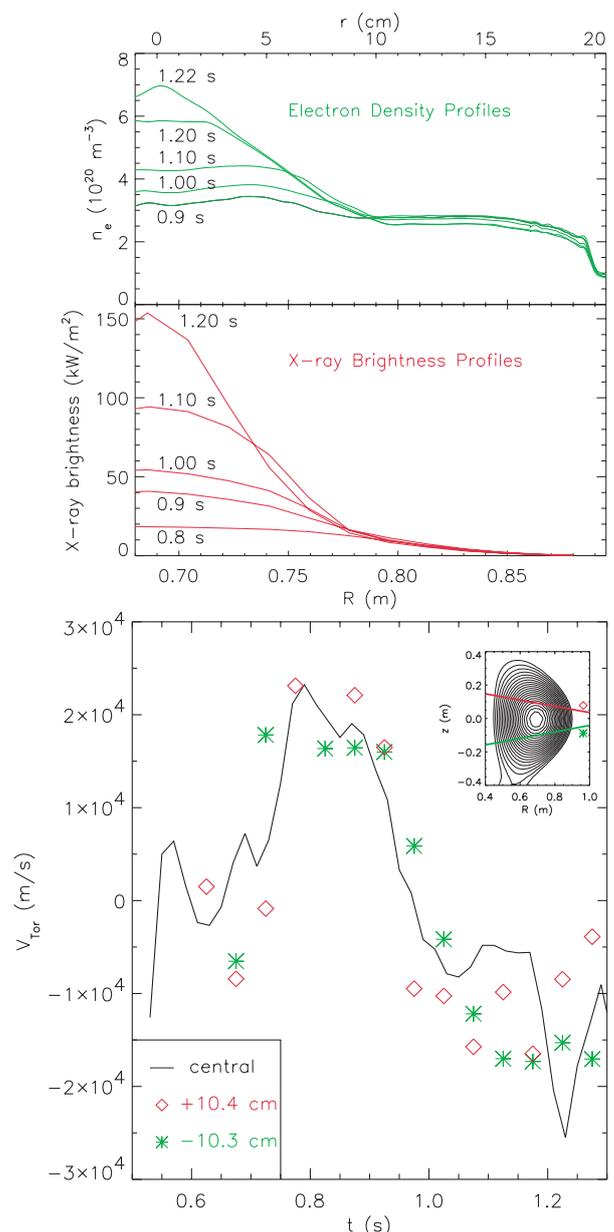
FIG. 30: Radial profiles of (a) electron density and (b) X-ray brightness, and (c) time evolution of toroidal rotation velocity at central chord, +10.4cm and -10.3cm in the ITB plasma in Alcator C-Mod (from figure 5 and figure 6 in [183]).

of the momentum transport equation (2) in page 2) does not depend on the sign of toroidal rotation. This term can be experimentally evaluated from the flux-gradient relation (P_ϕ vs $\partial V_\phi/\partial r$) of two ITB discharges with co and counter injection NBI. Here, the momentum flux in co injection ($P_\phi(\text{co})$) is positive value, while that in counter injection ($P_\phi(\text{ctr})$) is negative. This is because if the momentum viscosity is assumed to be unchanged between co-NBI and counter-NBI discharge (not be-

FIG. 31: (a) Sum (co+ctr) and difference (co-ctr) of normalized external torque as a function of velocity gradient from two ITB discharges with coinjection (co) NBI and counterinjection (ctr) NBI and (b) radial profiles of intrinsic torque in the L-mode, transition and ITB phase in LHD (from figure 4(b) and 6(b) in [120]).
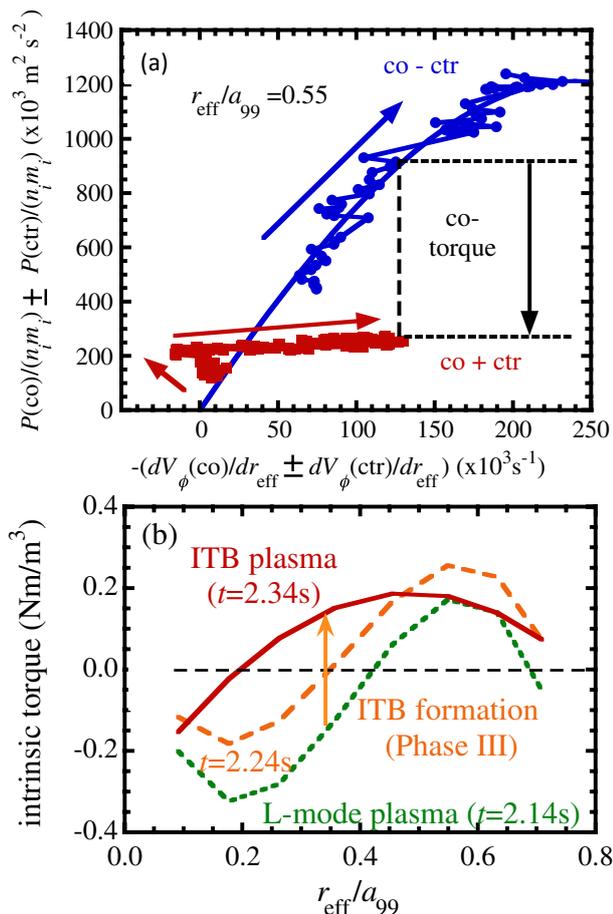
tween L-mode plasma and ITB plasma) and momentum pinch term is neglected, the difference of flux and gradient $(P_\phi(\mathrm{co})/(m_i n_i) - P_\phi(\mathrm{ctr})/(m_i n_i)$ and $\partial V_\phi/\partial r(\mathrm{co}) - \partial V_\phi/\partial r(\mathrm{ctr}))$ gives the flux-gradient relation of the diffusive term. Then the offset of sum of momentum flux (co+ctr) from the difference of momentum flux (co-ctr) gives the residual stress term of Γ_ϕ^{RS},(the third term of equation (2)). Here, the positive Γ_ϕ^{RS} is the radial flux due to the residual stress in counterdirection, while the negative Γ_ϕ^{RS} is the radial flux due to the residual stress in codirection. As seen in figure 31 (a), sum of momentum flux (co+ctr) is larger than the flux-gradient relation curve of the difference of momentum flux (co-ctr), which indicates that finite non-diffusive term in counterdirection at $r_{\mathrm{eff}}/a_{99} = 0.55$ (just inside the ion-ITB foot). The flux gradient curve of sum of momentum flux (co+ctr) is larger than the flux-gradient relation curve

of the difference of momentum flux (co-ctr) at the beginning, while the flux gradient curve of sum (co+ctr) becomes smaller than the flux gradient curve of difference (co-ctr) after the formation of ion-ITB. Then the significant non-diffusive term in codirection is required to satisfy the flux-gradient given by the difference of momentum flux (co-ctr) plotted in figure 31(a). This result indicates the finite non-diffusive term in counterdirection in L-mode phase and non-diffusive term in codirection in ITB phase

Figure 31(b) shows the radial profile of the intrinsic torque evaluated from the non-diffusive term of the momentum flux assuming the coefficient of the diffusive term (perpendicular viscosity) is identical between co-NBI dominate and counter-NBI dominant ITB discharges [120]. Before the ITB formation, the intrinsic torque is in the counterdirection in the core ($r_{\mathrm{eff}}/a_{99} < 0.4$), while it is in the codirection in the outer region ($r_{\mathrm{eff}}/a_{99} > 0.4$). The intrinsic torques in the core region change sign from the counterdirection to the codirection after the formation of the ITB, which clearly shows the strong coupling between the heat transport and the momentum transport. The intrinsic torque in the L-mode region is in the counterdirection, while it reverses to the codirection inside the ITB. The reversal of intrinsic torque from counterdirection to codirection is observed to be associated with the formation of ion ITB, where the ITG mode is expected to be unstable and the TEM is considered to be stabilized due to the increase of ion temperature gradient and flattening of electron density profile. The reversal of intrinsic torque is strong evidence of the change in turbulence state. The precise measurements of turbulence characteristics at the reversal of intrinsic torque are necessary to investigate the dominant unstable mode and understand the mechanism driving this intrinsic torque.

B. Impurity accumulation in tokamak plasmas

Impurity transport has been studied especially in the ITB plasma in tokamaks [190–193]. Although the ITB can contribute to the significant improvement of core confinement, maintaining the ITB plasmas in steady conditions with high plasma purity is challenging due to MHD instabilities, impurity accumulation, and high core radiations [194, 195]. The impurity accumulation in the ITB plasma has been recognized to be a serious problem especially for the steady-state operation in tokamak especially with the tungsten wall [196–199].

The accumulation is due to inwardly directed drift velocities inside the ITB radius. The strength of the impurity peaking increases with the impurity charge and is low for the low-Z elements C and Ne. Transport calculations show that the observed behavior is consistent with dominant neoclassical impurity transport inside the ITB plasma in JET [200]. In figure 32, various profiles for three time points during the ITB phase $t = 6.2, 6.6,$ and 6.8 s are shown and compared with measurements. As
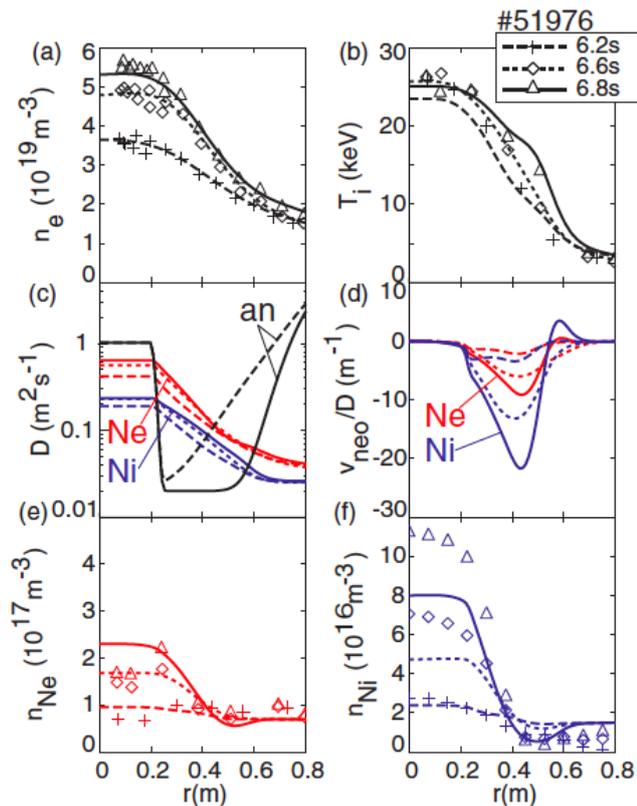
FIG. 32: Three radial profiles of (a) electron density, (b) ion temperature, (c) neoclassical and anomalous diffusion coefficient, D_{neo}, D_{an}, (d) neoclassical convection velocity normalized total diffusion coefficient $v_{neo}/(D_{neo} + D_{an})$, (e) neon (Ne) density, and (f) nickel (Ni) density from the impurity transport simulation in the ITB plasma in JET. The overlaid symbols give experimentally measured profiles (from figure 4 in [200]).
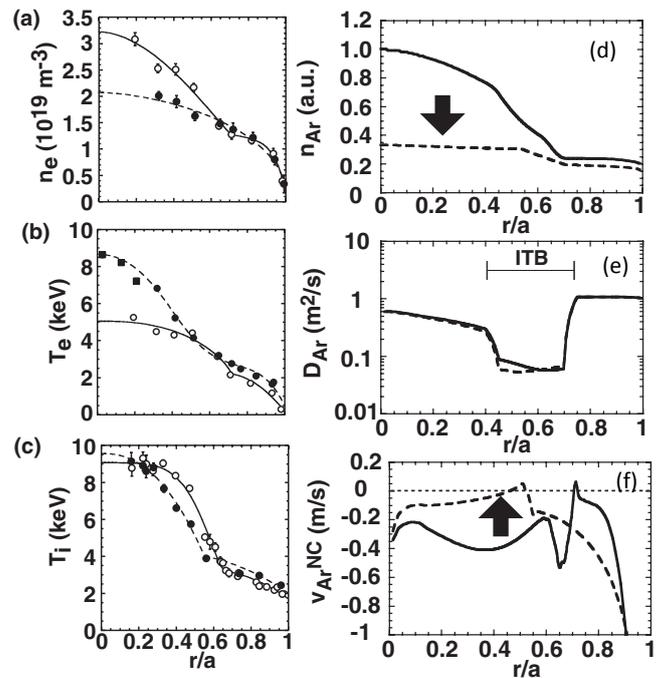
FIG. 33: Radial profiles of (a) electron density (b) electron temperature, (c) ion temperature, (d) calculated argon density which gives the soft X-ray emission profiles consistent with the measurements, (e) anomalous diffusion coefficient, and (f) neoclassical convention velocities of the high β_p ITB plasma before (solid lines) and during (dashed lines) the ECH in JT-60U (from figure 9(a)(b)(c) and figure 10 (c)(b)(a) in [204]).

seen in the density profile and ion temperature profiles in figure 32 (a)(b), the ITB structures are observed both in particle and ion heat transport. For neon (Ne) and nickel (Ni), the diffusion coefficients D_{neo} are shown in figure 32 (c) while the ratio $v_{neo}/(D_{neo} + D_{an})$ is depicted in figure 32(d). The value of anomalous diffusion coefficient, D_{an}, which is assumed to be equal for all species, is set ad hoc. Close to the axis the poloidal field becomes very low, the orbits of trapped particles are very large, and standard neoclassical theory may not be applied. Here, the measured profiles are flat and a high value of $D_{an} = 1$ m^2 s^{-1} is used to describe this situation. For $r > 0.2$ m, the anomalous diffusion coefficient is chosen to be below D_{neo} with $D_{an} = 0.02$ m^2 s^{-1} for radii inside the radius of the ITB and to increase from the ITB radius towards the edge. The plot of v_{neo}/D demonstrates that transport is more convective for Ni, the element with higher Z compared to Ne, and stronger peaking is expected for Ni. The peaking increases with the impurity charge and is low for the low-Z elements C and Ne as expected from

neoclassical convection [201]. These z-dependences of convection observed in ITB plasma in JET are consistent with that observed in the H-mode plasma in PBX [202]. This can be seen in figures 32 (e) and (f), where the simulated density profile of Ni evolves a much stronger peaking than Ne. While the measured Ne densities are well described by the model, there is still not enough peaking of Ni in the simulation. The central density at $t = 6.8$s is $n_{Ni} = 8\times 10^{16}$m^{-3}, i.e., 27 % below the measured value. The turbulence driven convection velocity is also the candidate to explain the discrepancy between the measurements and predictions by neoclassical model. Theoretical predictions of the turbulent convection velocity including recent quasilinear gyrokinetic results are in qualitative agreement with a dedicated experiment [203].

In contrast, the diffusion coefficient of impurity (carbon and argon) estimated assuming the neoclassical inward convection velocity were found to be 4 - 5 times larger than the neoclassical value in the ITB plasma in JT-60U [204]. The diffusion coefficient of both argon and carbon estimated assuming the neoclassical inward convection velocity are also 4 - 5 times larger than the neoclassical value. Helium and carbon are not accumulated inside the ITB even with ion heat transport close to

a neoclassical level, while the argon impurity shows accumulation [205]. The helium diffusivity (D_{He}) and the ion thermal diffusivity (χ_i) are 5 - 15 times higher than the neoclassical level in the high β_p ITB plasma. Therefore, there are clear discrepancies between the impurity profile measured and predicted by neoclassical convention velocity and diffusion coefficient.

Argon impurity can be exhausted from inside the ITB region by applying ECH in the high β_p ITB plasma associated with the flattening of electron density [204]. Figure 33 shows the radial profile of electron density, electron temperature, ion temperature, neoclassical convention velocity, anomalous diffusion coefficients, and simulated argon profiles that matched the observed soft X-ray emission. When the ECH is applied, electron temperature profile is peaked due to the central electron heating and both electron density and argon density profile show flattening, while the ion temperature profile is almost unchanged. The flattening of argon profile inferred from the soft x-ray emission is consistent with the prediction of decreases of neoclassical convection velocity due to the flattening of electron density with almost identical anomalous diffusion coefficient profile. There is no impurity exhaust observed by ECH in the reversed magnetic shear ITB plasma, where there is no flattening of electron density due to ECH This is due to the fact that ECH does not cause the flattening of electron density in the reversed shear ITB. These results imply that density peaking is a cause of impurity accumulation of argon. However, these results can not exclude the possible mechanism that the increase the electron temperature gradient enhance the outward convection of both bulk ion and impurity ions as predicted by so-called temperature screening effect [206].

The relation between the density peaking and impurity peaking is an interesting topic, because there is no impurity accumulation in the helical plasma, where the density profile is flat even in the plasma with ITB of heat transport. It should be also noted that the tokamak ITB plasma with pure electron heating does not have serious impurity accumulation [207]. The other mechanism to prevent the impurity accumulation is MHD activity. The sawtooth activity in the core region causes the flattening of impurity density inside $q = 1$ surface [208]. In some cases a sudden expulsion of impurity is observed associated with the $m/n = 1/1$ MHD activity even before the sawtooth starts or even in the plasma without sawtooth. The sudden expulsion of impurity has been observed in various tokamaks in DIII-D ('type-O' discharge) [209], in PBX ('impurity crash' [69]), and in JET [210], regardless of the confinement mode.

C. Temperature screening in tokamak and impurity hole in helical plasmas

It is an interesting topics whether the neoclassical process is dominant or not in the impurity transport in the helical plasma with ITB where the turbulent transport is suppressed. Various experiments on impurity transport in helical plasmas have been reported. Since the neoclassical transport in helical plasma is larger than that in tokamak, the impurity transport in helical plasma has been considered to be dominated by neoclassical transport rather than turbulent transport. However, the recent observation of impurity hole was found to be inconsistent with the neoclassical prediction. The very hollow impurity density profile, namely, the impurity hole, has been observed associated with the formation of ITB in LHD [211, 212]. It is interesting to compare the carbon impurity profiles in the plasma with ion ITB and with flat electron density profiles in tokamak and helical plasmas. Figure 34 shows the radial profiles of ion temperature, electron temperature, electron density, and carbon density of the ion ITB plasmas in DIII-D [206] and LHD [212].

In DIII-D, the impurity density profiles are measured with charge exchange spectroscopy in the VH-mode, where the strong ion temperature gradient is observed up to near the magnetic axis in $\rho < 0.5$ with flat electron density profiles and with almost zero electron density gradients. In this discharge, both the carbon and neon density profiles are observed to quickly reorganize from a centrally peaked profile to a strongly hollow profile during the VH-mode phase. The very hollow carbon profile measured provides clear evidence that a strong outward convective component of the impurity particle flux is present. Comparing the measurements with theoretical predictions of collisional (neoclassical) transport indicates that the observed outward convection results from an effect known as temperature screening.

In LHD, precise measurement of ion temperature and carbon density are given by the charge exchange spectroscopy. In this discharge, the sharp ion temperature gradient is observed up to near the magnetic axis, while the electron temperature gradient decreases in the core region and is much smaller than that of ions. The electron density profile is flat and only the small density gradient exists in the plasma core of $\rho < 0.9$, which is a typical electron density profile in LHD. The carbon profile is very hollow and it has a peak near the plasm edge $\rho = 0.7 - 0.8$, which is called 'impurity hole'. Although the observed radial profile of carbon density is very similar to that observed in DIII-D, the hollow carbon density profile and the strong outward convective component of the impurity particle flux is not due to the collisional (neoclassical) transport. In the helical plasma, the convective component by radial electric field is more dominant than the component of the temperature gradient. In this plasma, the neoclassical convection component of the impurity particle flux is inward due to the negative electric field, which is confirmed by the measurements of HIBP in LHD [213].

Therefore, the hollow impurity profile observed in LHD is not consistent with the neoclassical prediction. Comprehensive electrostatic gyrokinetic linear stability calculations for ion-scale microinstabilities in an LHD plasma
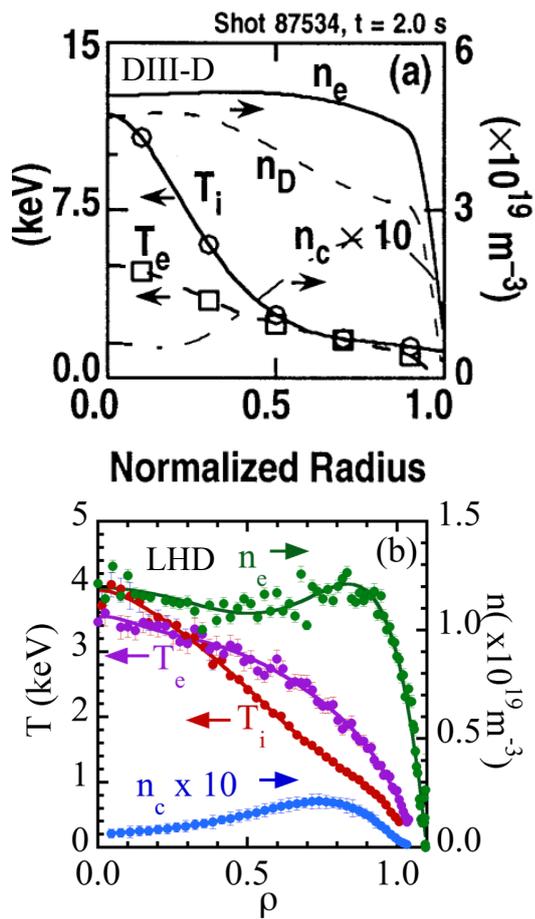
FIG. 34: Radial profiles of ion temperature, electron temperature, electron density, and carbon density of the ion ITB plasmas in (a) DIII-D and (b) LHD (from figure 2(a) [206] and figure 2 in [212] modified).

FIG. 35: Time evolution of (a) ion temperature, electron temperature, and density at plasma center, (b) carbon density at various radii, and (c) flux-gradient relation in the impurity transport at the formation of ITB in LHD. Vertical lines show the timing at which the carbon density near the plasma core changes from increasing to decreasing. (from figure 1(b)(d) and figure 2 in [215]).

with an ITB and carbon impurity hole were used to make quasilinear estimates of particle flux to explore whether microturbulence can explain the observed outward carbon fluxes that flow 'up' the impurity density gradient. As the carbon density gradient is scanned between the measured value and zero, the quasilinear carbon flux is invariably inward when the carbon density profile is hollow, thus turbulent transport due to the instabilities considered here does not explain the observed outward flux of impurities in impurity hole plasmas [214].

Figure 35(a)(b) shows the time evolution of ion temperature, electron temperature and density, and carbon density at various radii at the formation of ITB in LHD [215]. Although the increase of ion and electron temperature are gradual, the change in electron density and carbon density is abrupt. Before the formation of ITB, both electron density and carbon density increase. However, both densities suddenly start to decrease after the formation of ITB. As seen in figure 35(b), the decrease of

impurity starts from center ($\rho = 0.1$) and propagates to the edge ($\rho = 0.89$). The radial flux is evaluated from the change in carbon density ($\partial n_c/\partial t$). Figure 35(c) shows a relationship between the radial particle flux of carbon normalized by the carbon density and the gradient of the carbon density normalized by the carbon density during impurity hole formation at the normalized minor radius $\rho = 0.74$ where the gradient of the carbon density varies widely from positive to negative. The flux changes from

inward (negative) to outward (positive) dynamically over time. The diffusion coefficient of 0.12 m^{2}s^{-1} (slope of the line) and outward convective flow velocity (y-intercept of the line) are observed late in the discharge as the dotted line in figure 35(c). It is clear that the radial carbon flux changes its sign from negative (inward) to positive (outward) in the time scale of 100 ms (from $t = 3.93$ to 4.03 sec), where there is not much change in plasma parameters. The abrupt change of radial carbon flux can not be explained by neoclassical convection, because the temperature and density gradient that determine the flux can change gradually in time and the NBI heated plasma in this discharge is in the ion root (negative E_r) and no transition to electron root (positive E_r) is expected [213]. This experiment shows the strong non-linearity in the convection component of the impurity transport. One of the candidates of the non-linear process is a modification of the dominant underlying instability [216].

VI. NON-LOCALITY OF INTERNAL TRANSPORT BARRIER PLASMAS

A. Transport coupling between inside and outside the internal transport barrier

The core and edge transport coupling has been observed in the plasma as a sudden change of core transport associated with the transition from L-mode to H-mode transition [217–219] and the model of non-local transport was proposed [220, 221]. Non-locality of transport was observed as an interplay between the edge transport barrier and the internal transport barrier in the transient phase. The coupling of transport between inside and outside the ITB region is another example of non-locality of transport.

Figure 36 shows the time evolution of electron temperature measured with ECE at various radii in JT-60U [222]. In this discharge, the back-transition from H-mode to L-mode occurs at $t = 6.08$ sec and the electron temperature at half radius ($r/a = 0.57$) starts to decrease. The formation of ITB starts at $t = 6.3$ sec and the electron temperature in the core region ($r/a = 0.28$ - 0.57) starts to increase. The L-mode to H-mode transition occurs during the formation of the ITB at $t = 6.4$ sec and transient small decrease of electron temperature is observed at half radius, which implies the degradation of ITB associated with the transition from L-mode to H-mode. These electron temperature responses were interpreted as the transient increase of thermal diffusivity in the ITB region at the time of transport transition at the edge. Although the degradation of ITB is small and only in the narrow region in radius, this result gives the experimental evidence for the transport coupling between the edge and core region.

The other coupling of transport between inside and outside the ITB region is observed as simultaneous increase and decrease of temperature gradient inside and
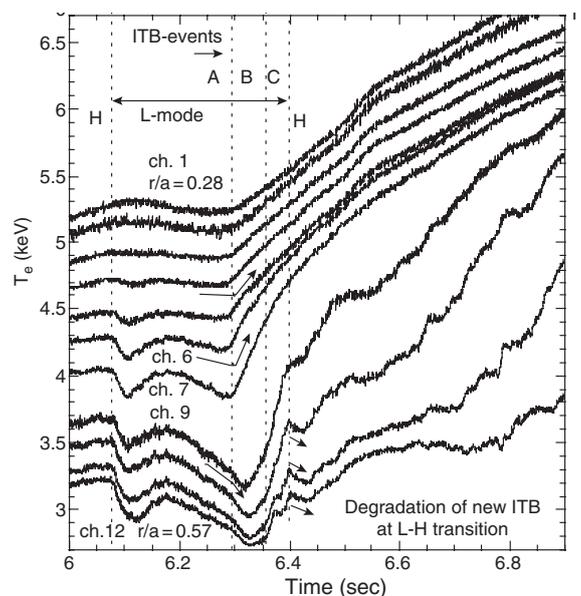

FIG. 36: Time evolution of electron temperature measured with ECE at various radii during the ITB formation ($t > 6.3$ sec) with L-H transition ($t = 6.4$ sec) in JT-60U (from figure 4 in [222]).

outside (inner side of shoulder or outer side of foot) ITB region. Figure 37(a)(b) shows the time evolution of the electron temperature gradients during the formation of electron ITBs in LHD and JT-60U after the ECH pulse is turned on in the NBI heated plasmas. In LHD, the temperature gradient at $\rho = 0.17$ and $\rho = 0.3$ increases on a transport time scale (~ 35 ms) after the ECH pulse is turned on. The temperature gradient keeps increasing at $\rho = 0.3$, which becomes the high gradient ITB region, while the temperature gradient starts to decrease at $\rho = 0.17$, which becomes the 'shoulder' of the ITB. Similar behavior is observed during the formation of the parabolic-shaped ITB in JT-60U with a positive magnetic shear, where the central q value is low enough not to cause the degradation of the transport. In both discharges, the simultaneous changes in temperature gradient (increase of the temperature gradient inside ITB and decrease of the temperature gradient just on the inner side of shoulder) are observed at the transition from L-mode phase to ITB phase (1.335 sec in LHD and 5.105 sec in JT-60U).

The decrease of temperature gradients on the outer side of ITB foot is observed at the transition from L-mode phase to ITB phase in HL-2A as seen in figure 37(c) [57]. In the L-mode phase, the ion temperature gradients at both $\rho = 0.2$ and $\rho = 0.5$ increase in time. The normalized ion temperature R/L_{Ti}, where the R is major radius and L_{Ti} is scale length of ion temperature defined by -$T_i(\partial T_i/\partial r)^{-1}$, increases from L-mode level (~ 5) to the marginal level (~ 10). After the transition

FIG. 38: Radial profiles of (a) ion temperature (T_i), (b) first derivative ($\partial T_i/\partial r$), and (c) second derivative ($\partial^2 T_i/\partial r^2$) of ion temperature profile of ITB plasma in HL-2A (from figure 2 (a)(c)(d) in [57]).
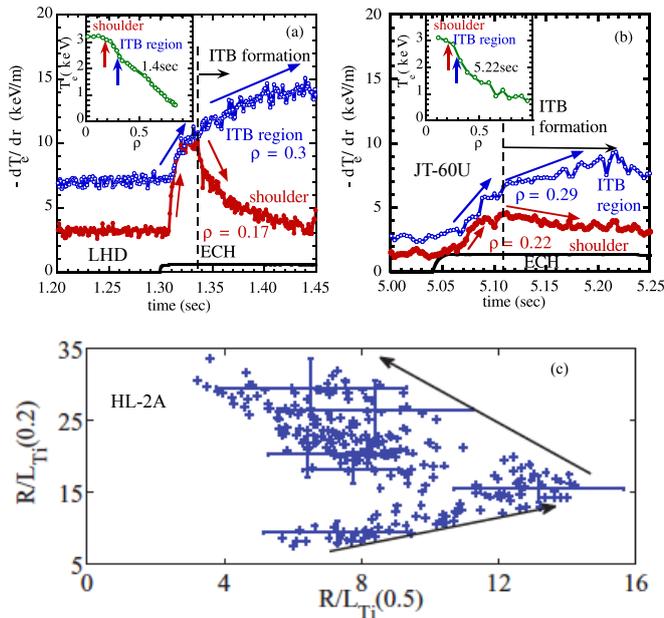
FIG. 37: Time evolution of electron temperature gradient at ITB region and shoulder in (a) LHD and (b) JT-60U and relation between the ion temperature gradient at $\rho = 0.2$ and $\rho = 0.5$ in HL-2A (from figure 3(a)(b) in [167] and figure 8(b) in [57]).

from L-mode to ITB mode, the normalized ion temperature gradient at $\rho = 0.2$ (ITB region) keeps increasing and reaches the ITB level (~ 30). However, the normalized ion temperature gradient at $\rho = 0.5$ (just on the outer side of ITB foot) starts to decrease to low level of ~ 6. This result clearly demonstrates the degradation of transport outside ITB region associated with the development of ITB [57]. Similar behavior is observed after the formation of ITB in the helical plasma and the increase of thermal diffusivity outside ITB region after the formation of ITB is reported in LHD [223].

B. Curvature of ion temperature inside internal transport barrier and its transition

The precise measurements of ion temperature profiles with charge exchange spectroscopy can provide the radial profiles of first derivative (gradient) and second derivative (curvature) of ion temperature profiles [224, 225]. The second derivative of ion temperature ($\partial^2 T_i/\partial r^2$) is positive at the foot point, while it is negative at the shoulder. Therefore, it is important to evaluate the radial profile of second derivative of ion temperature in the ITB region to study the shoulder and foot position and its sharpness.

Figure 38 shows the radial profiles of ion temperature and first and second derivative of ion temperature. The first derivative of ion temperature can be up to -

17 keV/m at the center of ITB regions. The second derivative of ion temperature has positive peak at the foot point and negative peak at the shoulder. The radial profile of second derivative is symmetry (magnitude of positive peak $\sim$ magnitude of negative peak) and the magnitude of second derivative of ion temperature is (0.2 - 0.3 MeV/m^2). The ITB foot location is determined from the peak of second derivative of ion temperature in this experiment. The location of ITB foot moves a little inward after the formation of ITB in this discharge. Because the relation of the location of the ITB foot to the rational surface is a key issue to understand the mechanisms of formation of this ITB, the quantitative comparison of ITB foot location with $q = 1$ location is necessary.

The non-locality of transport is also observed even just inside the ITB region alone and it determines the curvature of temperature profile inside ITB. When the radial structure of ITB is like a hyperbolic tangent shape, the region with positive second derivative is equal to the region with negative second derivative of ion temperature (symmetric ITB). However, the ITB can be asymmetric. Depending on whether the width with positive second derivative ($\partial^2 T_i/\partial r^2 > 0$) or negative second derivative ($\partial^2 T_i/\partial r^2 < 0$) is wider, there are two types of ITBs. One is concave ITB where $W_{\partial^2 T_i/\partial r^2 > 0} > W_{\partial^2 T_i/\partial r^2 < 0}$ and the other is convex ITB where $W_{\partial^2 T_i/\partial r^2 < 0} > W_{\partial^2 T_i/\partial r^2 > 0}$.

A spontaneous transition phenomena between two states of a plasma with an internal transport barrier (ITB) is observed in the steady-state phase of the magnetic shear in the negative magnetic shear plasma in the JT-60U tokamak. These two ITB states are characterized by different profiles of the second radial derivative of the ion temperature inside the ITB region (one has a weak concave shape and the other has a strong convex shape) and by different degrees of sharpness of the interfaces
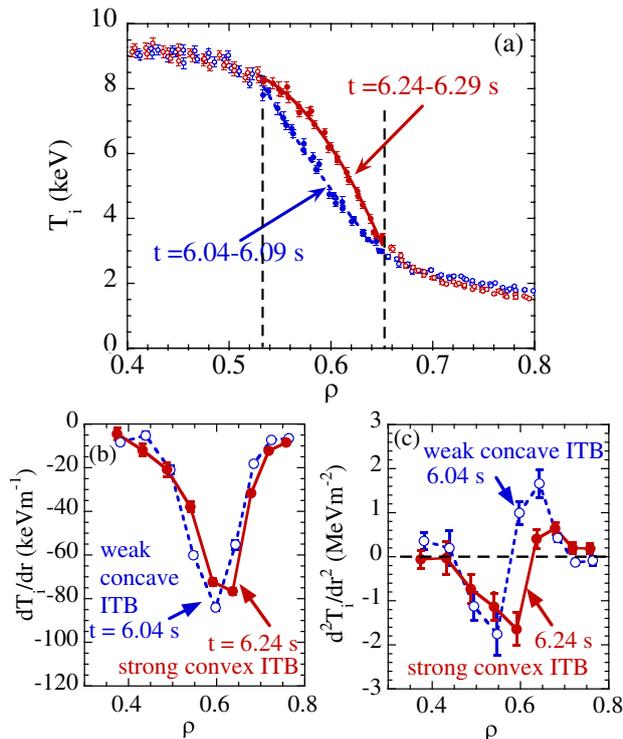
FIG. 39: Radial profiles of (a) ion temperature (T_i), (b) first derivative, ($\partial T_i/\partial r$), and (c) second derivative ($\partial^2 T_i/\partial r^2$) of ion temperature profile of ITB plasmas in JT-60U (from figure 1(a) and figure 2(b)(c) in [226]).

between the L mode and the ITB region, which is determined by the turbulence penetration into the ITB region [226]. These two ITB states are characterized by different curvatures of ion temperature as seen in the temperature profiles at $t = 6.04$ - 6.09 sec and $t = 6.24$ - 6.29 sec in figure 39(a). Clear differences in the curvatures of ion temperature profiles between these two time slices are observed in the ITB region ($0.53 < \rho < 0.65$). On the other hand, the ion temperature outside the ITB region is identical within the error bar between these two states. The change in curvature of the temperature profile is observed in both ion temperature and the electron temperature measured with electron cyclotron emission (ECE). The change in the curvature of the ion temperature profile is not due to the change in the safety factor q profiles, because the q profiles measured with motional stark effect spectroscopy are identical within the error bar between the two ITB states. For both ITB states, the ITB region appears near the minimum q location ($q_{min} = 3.3$).

The radial profiles of the first and second derivatives are plotted in figure 39(b) and (c), respectively. The maximum of first derivative of ion temperature is 80 keV/m in both of these ITBs. The radial profile of second derivative is almost symmetry (magnitude of positive peak $\sim$ magnitude of negative peak) and the magnitude of second derivative of ion temperature is ~ 1.5 MeV/m^2 at $t = 6.04$ sec. The width with positive second derivative is slightly wider than that with negative derivative, and this ITB state is called a weak concave ITB. In contrast, the radial profile of second derivative is asymmetry at $t = 6.24$ sec and the positive peak is ~ 0.5 MeV/m^2, which is only one-third of the negative peak of ~ 1.5 MeV/m^2. The width with negative second derivative is much wider that that with positive second derivative and this ITB state is called a strong convex ITB. In the plasma with curvature transition, the location of foot and shoulder location can be derived more precisely as the inner and outer boundaries of the region ($\rho = 0.53$ and 0.65) where the transition of ion temperature is observed as seen in figure 39(a).

VII. KEY PARAMETER OF INTERNAL TRANSPORT BARRIER CONTROL AND FUTURE PROSPECTS

A. Stable sustainment of internal transport barrier

Sustaining the plasma with internal transport barrier in the steady-state is an important issue [227–229]. The strong coupling between the bootstrap current and ITB dynamics as discussed in section II-E can cause oscillation in the buildup and collapse of ITB. It is shown that oscillations in pressure gradient associated with repetitive internal transport barrier (ITB) buildup and collapse occur with ion-cyclotron resonance heating (ICRH), neutral-beam injection (NBI), and lower-hybrid current drive (LHCD) in JET. As seen in the figure 40(a)(b), the periodic increases and decreases of bootstrap current and plasma pressure occurs when the foot of the ITB is roughly coincident with the magnetic shear reversal radius [230]. This periodic change in pressure and its gradient indicates the periodic process of buildup and collapse of ITB. When the pressure profile is peaked, the sheared $E \times B$ flow suppress the turbulence and, furthermore, the significant off-axis bootstrap current appears with the peak at $\rho = 0.5$, enhances the negative magnetic shear, and opposes the growth of drift-wave instabilities.

The other type of oscillation is observed in the curvature of ITB, namely, between the concave and convex ITB. Figure 40(c) shows the spontaneous transitions between a concave ITB with a positive curvature ($|\partial T_i/\partial r(0.58)| > |\partial T_i/\partial r(0.71)|$) and a convex ITB with a negative curvature ($|\partial T_i/\partial r(0.58)| < |\partial T_i/\partial r(0.71)|$) observed in JT-60U. The transition from convex ITB to concave ITB is observed at $t = 5.27$ - 5.41 sec, while the transition from concave ITB to convex ITB is observed at $t = 5.55$ - 5.62 sec and the minor collapse is observed at $t = 5.68$ sec [167]. The minor collapse occurs when the ion temperature gradient near the foot point $\rho = 0.71$ increases, not near the shoulder point $\rho = 0.58$. Therefore the collapse of the ITB occurs during the phase of ITB
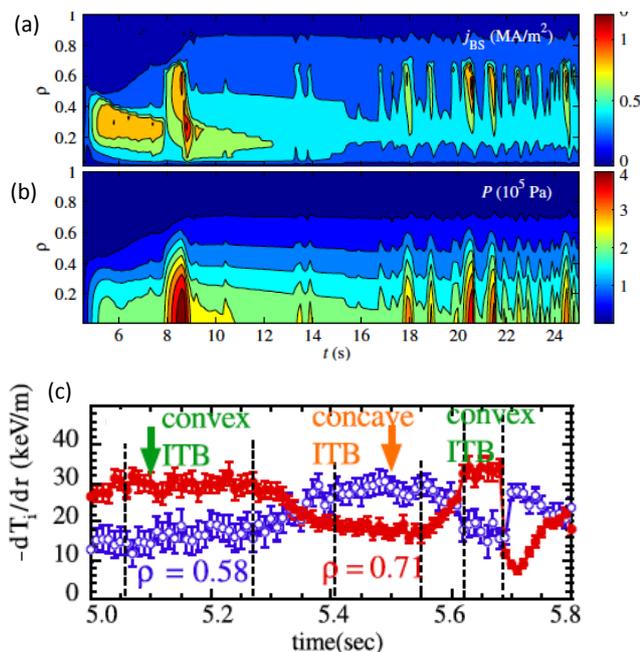
FIG. 40: Contour of (a) bootstrap current and (b) plasma pressure in time and normalized minor radius (t and ρ) in JET (from figure 3 in [230]) and (c) time evolution of ion temperature gradient at two locations ($\rho = 0.58$ and $\rho = 0.71$) in the ITB region in JT-60U (from figure 4(a) in [167]).

with a negative curvature and the ITB with positive curvature is more preferable to sustain the ITB state longer without collapse.

The difference in time scale of change in $E \times B$ flow due to the change in pressure gradient and the change in magnetic shear by the bootstrap current can cause the oscillation of ITB buildup and collapse. The oscillation of ITB buildup and collapse in JET can be reproduced by the transport model iterated with given ICRH profiles and self-consistently with NBI and LHCD calculation and with the stabilizing turbulence by the $E \times B$ flow shear being combined with that of reversed magnetic shear in the simulation of ITB dynamics. However, there is no transport model which reproduces the oscillation of curvature of ITB observed in JT-60U, because the q profiles are almost unchanged during the oscillation of ITB curvature. In order to clarify the mechanism causing the ITB curvature oscillation, the understanding of non-local transport is necessary.

B. Avoidance of MHD instability

The performance of ITB is limited by the MHD activity, not by the transport, due to the significant suppression of electro-static turbulence. The bursting MHD activities due to the unstable resistive interchange mode ap-

pears in the negative central magnetic shear plasmas and sometimes trigger the disruption in D-IIID [231]. Avoidance of MHD instability is a crucial issue for sustaining the ITB plasma in the steady-state because the MHD activity localized in the sharp pressure gradient limits the increase of pressure gradients or causes the termination of ITB [232]. The Mercier criterion can be violated from the plasma centre to the region with the large pressure gradient in the ITB region when the $(q_0-q_{min})/q_{min}$ is high in JT-60U [233].

Because the foot point of ITB often locates near the rational surface, the ITB plasma with convex curvature is more dangerous due to the larger pressure gradient near the foot point of ITB. In contrast, the ITB plasma with concave curvature, where the pressure gradient is smaller near the foot point of ITB, is more preferable for avoiding the MHD activity localized at the ITB region. In fact, the minor MHD collapse appears at the convex ITB phase but not in the concave ITB phase in JT-60U as seen in figure 40(c). In the plasmas without ITB, the control of local current profile is important to satisfy the Mercier criterion in the stable region, and modulated ECCD associated with the phase of magnetic island has been the useful tool to stabilize the NTM activity [234]. However, in the plasmas with ITB, the control of pressure gradient near the rational surface is more important because the pressure gradient near the foot point (in many cases near the rational surface) itself is closely related to the stability. The strong non-linearity of the transport, which sometimes causes the oscillation of temperature gradient, has a strong impact on the trigger of MHD stability in the plasma with ITB. These results suggest the importance of understanding non-local transport which causes curvature transition. The deeper understanding of non-local transport is necessary for avoiding the MHD collapse or disruptions [235–237] and for sustaining the stable steady-state ITB plasmas in future tokamak device.

The candidate of the mechanism causing MHD collapse in the ITB plasma even at low β is resistive interchange mode [238] or barrier localized mode [239]. The effect of the toroidal flow shear profile on the dynamics of ITB evolution is investigated. It is found that the decorrelation between meso-scale modes and ITG driven modes due to the toroidal flow shear can prevent global relaxation [240]. Detailed study for the avoidance of MHD collapse by controlling the input torque of NBI has been done in JT-60U. It was found that the MHD collapse occurs when the q_{min} becomes integer (2,3,4) [63] and it is important to reduce the pressure gradient at the rational surface or increase the MHD stability limit. The discharges with co-NBI or counter-NBI were considered to be most preferable to the avoidance of MHD collapse because fast toroidal rotations would contribute to the stability of MHD modes through the wall stabilization [241].

Two techniques have been developed to avoid this termination event: a reduction of the heating power level
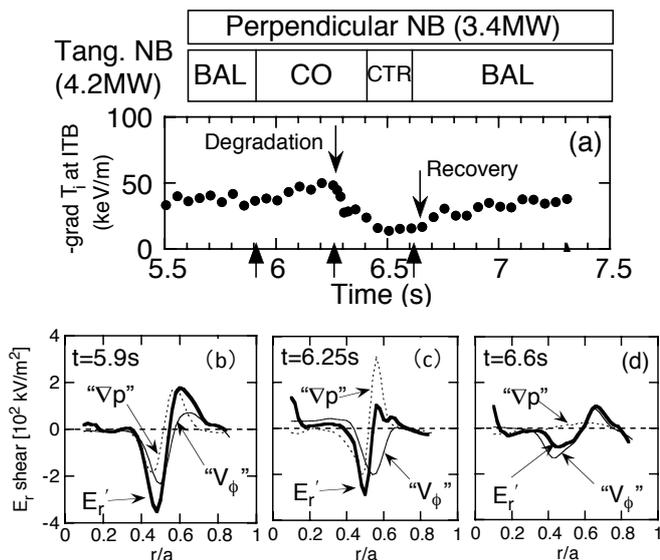
FIG. 41: (a) Time evolution of ion temperature gradient at ITB and radial profiles of radial electric field shear (E_r shear) in (b) balanced NBI ($t = 5.9$ s), (c) co-NBI ($t = 6.25$ s), and (d) counter-NBI ($t = 6.6$ s) phase in the negative magnetic shear plasma in JT-60U. Here "∇p" and "∇V_ϕ" are the pressure gradient term and the toroidal rotation term of radial electric field shear of E_r', respectively (from figure 6(a) and figure 7(a)(b)(d) in [63]).

to control the pressure gradient directly, as in JET and JT-60U, and a transition to H-mode where an edge pressure gradient develops and makes the pressure profile less peaked [242]. Although the coexistence of H-mode pedestal helps to avoid the ITB termination due to the sharp pressure gradient, if the ELM activity becomes large enough, the ELM crash also triggers the ITB collapse. The torque control is considered to be a useful tool to reduce the temperature gradient (weaken the ITB at the rational surface) through E_r shear control as well as heating power control, because the plasma toroidal rotation has significant contribution to the formation of radial electric field. Figure 41(a) shows an example of E_r shear modification in the ITB region through torque control in JT-60U [63]. It is an important characteristic that the radial profiles of E_r shear due to the toroidal rotation shear are quite different for balanced, co- and counter-NBI due to the shape and sign difference in the toroidal rotation velocity. When the NBI torque input is switched from balanced to co-injection, the ion temperature gradient suddenly starts to show the degradation at $t = 6.25$ s and it recovers gradually after the NBI torque input is returned to balanced. As seen in the figure 41(b), the large E_r shear is sustained at balanced NBI phase ($t = 5.9$ s) in the wide range of plasma ($r/a = 0.4$ - 0.7) because the sign of the E_r shear due to the second derivative of ion pressure and that due to the toroidal rotation velocity shear matches. In contrast, the magnitude of E_r

shear decreases and the width of the E_r shear becomes narrow at co-NBI phase ($t = 6.25$ s) because the sign of the E_r shear due to the second derivative of ion pressure and that due to the toroidal rotation shear becomes opposite at the outer half of the ITB region ($r/a = 0.5$ - 0.65) as seen in figure 41 (c). In the counter-NBI phase ($t = 6.6$ s), both the E_r shear due to the second derivative of ion pressure and that due to the toroidal rotation becomes small as seen in figure 41(d).

It was reported that the MHD collapse can be avoided by controlling the torque input in the ITB plasma with $q_{min} = 4$ [80, 243] or by reducing the heating power in the ITB plasma with $q_{min} = 3$ [232]. However, the MHD collapse at $q_{min} = 2$ can not be avoided for large ITB by either control of torque input or power input, and it was found that the steady-state sustainment of the ITB plasma with low safety factor is more difficult [244]. It was also demonstrated that the lower hybrid current drive (LHCD) can contribute to maintaining the q profile, which is suitable for the large ITB with longer time duration in tokamaks [81–85]. The q profile achieved in the long-lasting ITB is consistent with the simulation results which include the spectral broadening induced by parametric instability [245]. Non-disruptive β collapses with a regular intermittency have been observed after a forced turn-off of neutral beam current drive (NBCD) in JT-60U fully non-inductive, reversed shear (RS) discharges [246]. These experiments show that the careful control of q profiles is necessary to sustain the ITB plasma in steady-state in tokamak.

C. Electron and ion temperature ratio

In the future device with nuclear fusion reaction, the electron heating due to the alpha particle will be dominant. Therefore the effect of electron heating on the ion transport in the ITB plasma will be an important issue. In order to have prospects for the achievement of high performance in the nuclear fusion device in future, where the electron heating by α-particles becomes dominant, the effect of electron heating to the ion transport has been investigated by adding the ECH heating to the NBI heated plasma [247–249]. As seen in figure 42(a)(b), there is no degradation of ion transport observed after the electron temperature increases due to the electron heating by ECH in JT-60U negative magnetic shear plasma. However, in the positive magnetic shear plasma in JT-60U, the degradation of ion transport occurs after the ECH was applied as seen in the decrease of ion temperature gradient at the $\rho = 0.4$ - 0.5 in figure 42 (c)(d). This degradation of ion transport is due to the increase of the T_e/T_i ratio due to electron heating. It is an interesting observation that the impact of the T_e/T_i ratio to the ion transport is quite different between the plasmas with negative and positive magnetic shear in tokamaks. Similar behavior is also observed in the negative central magnetic shear plasma in DIII-D. These observa-
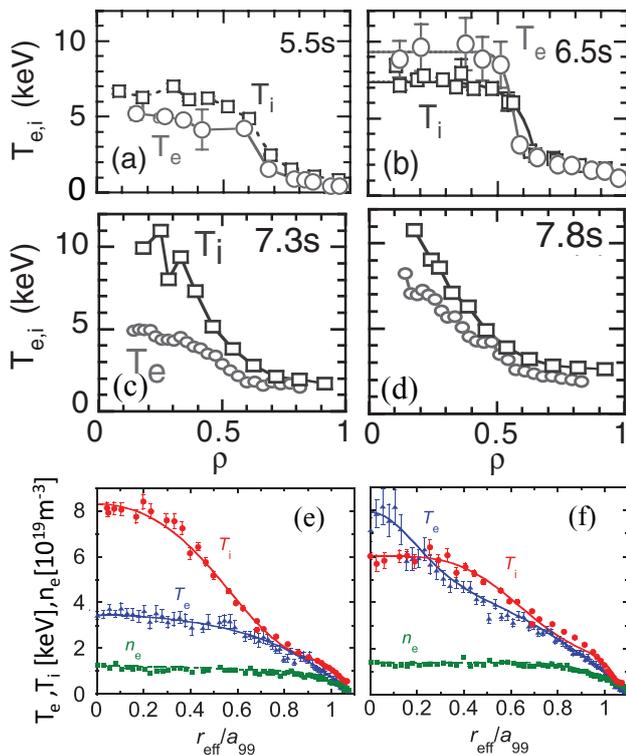
FIG. 42: Radial profiles of electron and ion temperature in the negative magnetic shear plasma in JT-60U (a) before and (b) after the ECH is applied, in the positive magnetic shear plasma in JT-60U (c) before and (d) after the ECH is applied (from figure 2(a) and figure 7(a)(c) in [248]), and electron and ion temperature and electron density in the negative shear (normal shear) in LHD (e) before and (f) after the ECH is applied (from figure 3(c)(g) in [249]).

tions are consistent with gyrokinetic simulations, which show a smaller increase of the growth rates of the ion temperature gradient mode with increasing T_e/T_i in the negative magnetic shear plasma [250].

The degradation of ion transport due to ECH is more visible in the helical plasmas, where the magnetic shear is negative in the normal configuration, when the T_e/T_i ratio exceeds critical value (~ 1). As seen in figure 42(e)(f), the ion temperature gradient in the core region of r_{eff}/a_{99} = 0.2 - 0.4 significantly decreases associated with the increase of the T_e/T_i ratio due to the additional ECH. The impact of T_e/T_i ratio on ion transport commonly observed both in tokamak and helical plasma suggests that the turbulence determining the ion transport (ITG is one of the candidates) is sensitive to the T_e/T_i ratio and it sharply increases as the T_e/T_i ratio exceeds a critical value (≥ 1). However, the different response of the T_e/T_i ratio to the ion transport is unclear, because the difference in magnetic shear alone can not explain the experimental results observed in the differences in positive/negative magnetic shear in tokamak and nega-

tive magnetic shear plasma in helical system consistently. These experiments imply the importance of the control of T_e/T_i ratio not be too high (not exceeding a critical value) in order to sustain the good property of ion ITB.

VIII. DISCUSSION AND SUMMARY

In this section, the definition and identification of the ITB is discussed. In this review paper, when the plasma has a bifurcation of flux gradient relation between enhanced transport and reduced transport as illustrated in figure 43 (a), the plasma is categorized to ITB plasma. In the linear transport, the heat flux normalized by density is proportional to the temperature gradient and the thermal diffusivity defined by the ratio of normalized heat flux to temperature gradient has constant value. In the L-mode plasmas, the thermal diffusivity increases as the temperature gradient is increased due to the non-linear increase of turbulence level, which is called the enhancement of transport. In contrast, the thermal diffusivity can decrease as the temperature gradient is increased in the improved mode by turbulence suppression, which is recognized as reduced transport. This bifurcation causes the discontinuity of temperature gradient for a given heat flux as seen in figure 43(b), hence the discontinuity of the temperature gradient in radius. The ITB region can be defined as the region where the thermal diffusivity decreases as the temperature gradient is increased. In the plasma with ITB, there is L-mode region, where the thermal diffusivity increases as the temperature gradient is increased. A discontinuity of temperature gradient appears at the interface between the ITB region and the L-mode region, and this interface point is usually called ITB foot.

In general, there are two locations that show the discontinuity of temperature gradient in radius: one is a foot point, where the temperature gradient is larger inside and smaller outside and the other is a shoulder point, where the temperature gradient is smaller inside and larger outside. At the lower heat flux, the discontinuity of temperature gradient in radius becomes small. In this case the change in temperature gradient (or thermal diffusivity) between low heating power (L-mode plasma) and high heating power give us the information of the foot and the shoulder point, because thermal diffusivity should decrease in the ITB region (outside shoulder point and inside foot point) and slightly increase in the L-mode region (inside shoulder point and outside foot point) as the heat flux is increased. Because the discontinuity of transport near the magnetic axis is hardly detected due to the lack of sufficient heat flux, the shoulder is not always observed in the ITB plasmas.

The identification of ITB using the flux-gradient relation was done in LHD plasma, where the foot point and time of the transition from L-mode to improved mode (the timing of formation of ion ITB) is not so clear compared with the ion-ITB in tokamaks. Figure 44 shows
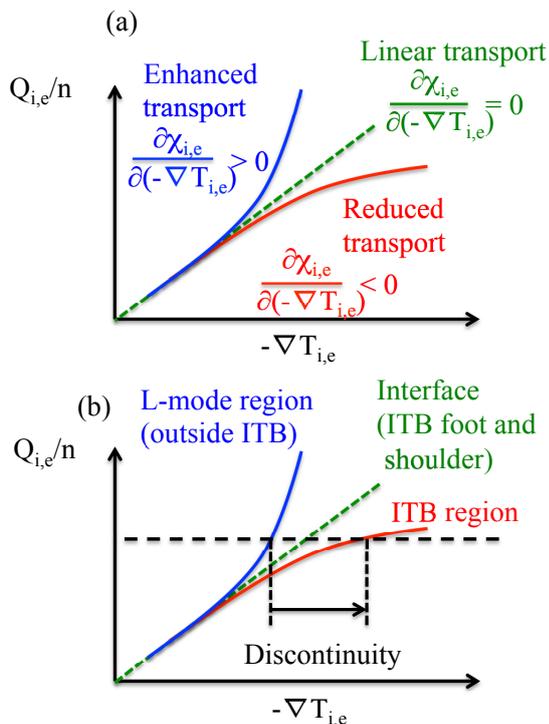
FIG. 43: Flux gradient relation of heat transport in (a) toroidal plasma and (b) the plasma with internal transport barrier (ITB).
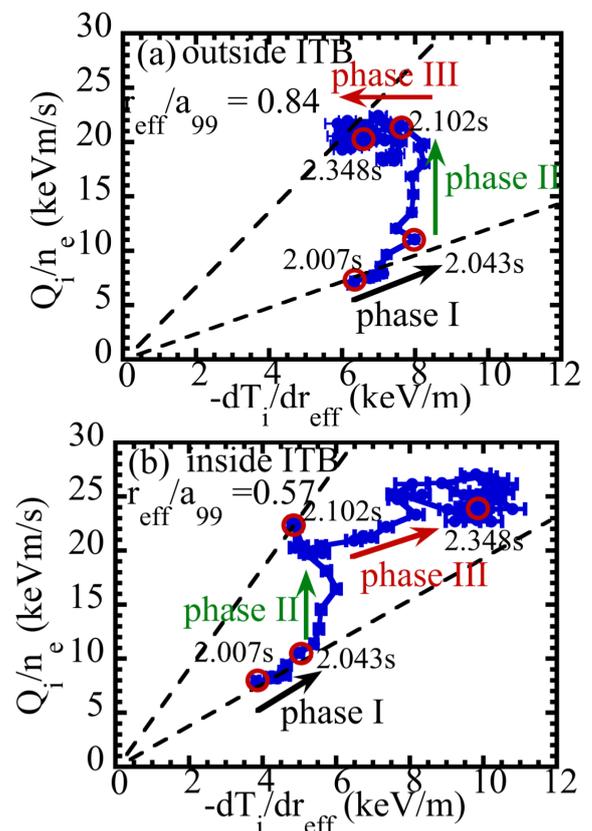

FIG. 44: Flux gradient relation between ion heat flux normalized by density and ion temperature gradients at the normalized minor radius of (a) 0.84 (outside the ITB) and (b) 0.57 (inside the ITB) (from figure 2(a)(b) in [120]).

the flux-gradient relation during the linear confinement mode (phase I), L-mode (phase II), and ITB formation (phase III) in the outer region ($r_{\text{eft}}/a_{99} = 0.84$) and inner region ($r_{\text{eft}}/a_{99} = 0.57$) of ITB foot. In phase I, the ion heat flux normalized by density increases linearly as the ion temperature gradient is increased in both the inner and outer regions of ITB foot. In phase II, the normalized ion heat flux sharply increases even with the small increase of ion temperature gradient in both the inner and outer regions of ITB foot, which indicates that the plasma is in the L-mode phase. In phase III, associated with the increases of normalized ion heat flux, the ion temperature gradient inner region of ITB foot shows significant increase while that outer region of ITB foot shows decreases. The flux-gradient relation clearly shows the timing when the ITB formation starts (It is 2.102 sec in this example.) and where the ITB foot locates. These results clearly demonstrate that the precise evaluation of the timing of formation/termination and location of foot/shoulder points of the ITB requires the time dependent flux-gradient relation analysis at various position of the plasma, because the evaluation from the radial profile of temperature and density alone is sometimes difficult, especially for the weak ITB plasma.

In summary, the characteristics of ion and electron heat transport and electron and impurity particle transport of the ITB plasmas in tokamak and helical devices

are reviewed. The ITB is defined as the appearance of discontinuity of temperature, flow velocity, or density gradient in radius. These gradients become larger in the ITB region, although the heat, momentum or particle flux are almost unchanged between inside and outside ITB at the ITB boundary where the discontinuity of gradients appear. From the radial profiles of temperature, flow velocity and density the ITB is characterized by three parameters of normalized temperature gradient, R/L_T, the location, ρ_{ITB}, and the width, W/a and can be expressed by 'weak' ITB (small R/L_T) or 'strong' (large R/L_T), 'small' ITB (small ρ_{ITB}) or 'large' ITB (large ρ_{ITB}), and 'narrow' (small W/a) or 'wide' (large W/a). There is a wide variety of the magnitude of gradient, location, and width of ITB. The 'strong' ITB tends to be 'narrow' and the 'weak' ITB tends to be 'wide'. Therefore in many cases the central parameter (temperature, flow velocity and density) in the 'strong' ITB plasma is not always higher than that in the 'weak' ITB plasma. From the stability point of view, the 'weak' and 'wide' ITB is preferable and 'large' ITB is desirable for the high performance of confinement.

The difference of ITB profiles between tokamak and

helical ITB plasmas is summarized in table 1. Although there are wide varieties of the temperature profile in tokamak ITB plasma, the temperature profile in helical plasma does not have variety. The electron ITB in helical plasma is usually strong, narrow, and small, while that in tokamak plasma can be weak or strong, narrow or wide, and medium or large. The ion ITB in helical plasma is weak wide and large, while that in tokamak plasma can be weak or strong, narrow or wide, and medium or large. These differences are attributed to the freedom of current profile and hence magnetic shear, which is very restricted in the helical plasmas where the magnetic field structure is mainly determined by the external coil current. The clear differences are observed in electron density and impurity density profiles. The density profile becomes peaked in tokamak ion-ITB plasma, while it is flat and almost unchanged in the ion-ITB plasma and becomes hollow in the electron ITB in helical plasmas. The impurity density profile becomes peaked in tokamak electron and ion-ITB plasma, but it is usually hollow in the electron and ion-ITB in helical plasmas.

Table 1: Comparison of ITB profiles between tokamak and helical plasmas.

Profile	Tokamak	Helical
e-ITB strength (R/L_T)	weak~strong	strong
e-ITB width (W/a)	narrow~wide	narrow
e-ITB region (ρ_{ITB})	medium~large	small
ion-ITB strength	weak~strong	weak
ion-ITB width	narrow~wide	wide
ion-ITB region	medium~large	large
density in e- and ion-ITB	flat~peaked	flat~hollow
impurity in e- and ion-ITB	flat~peaked	flat~hollow

There are three key physics elements for the ITB formation, radial electric field shear, magnetic shear, and rational surface (and/or magnetic island). The $E \times B$ shear, or the so-called radial electric field (E_r) shear, can suppress the turbulence and contribute to the formation of ITB. Both the steady state macro-scale $E \times B$ shear (mean flow shear) and oscillating meso scale $E \times B$ shear (zonal flow) have a strong impact on tilting and breaking the turbulence eddy. Recent detailed analysis of the radial electric field revealed that the second derivative of radial electric field $E \times B$ curvature is also important when the scale length of radial electric field is comparable to the size of turbulence eddy. The ITB foot, where the discontinuity of temperature or density gradient appears, often appears near the rational surface. In the monotonic magnetic shear the ITB foot is observed near the rational surface. There are experimental results that demonstrate the role of magnetic island on the formation of ITB. Although the pressure profile becomes flat at the O-point of magnetic island, the reduction of turbulence and hence the reduction of transport are expected at the bound-ary of magnetic island. In the reversed magnetic shear plasmas, the ITB foot often appears near the q_{min} location, when q_{min} crosses the rotational surface. However, there are experimental results which demonstrate that the q_{min} at the rational surface is not always required for the formation of ITB. Since the contribution of bootstrap current can be significant in the plasma with ITB, a strong positive feedback process between the change in magnetic shear due to the generation of bootstrap current and the change in pressure gradient due to reduction or enhancement of transport is considered to be a crucial issue.

The characteristics of electron and ion heat transport and electron (nearly equal to the bulk ion in the plasma with low impurity content due to the quasi-neutrality) and impurity transport are reviewed. There are significant differences in ion heat transport and electron heat transport. The difference of electron heat, ion heat, and particle, and transport coupling between tokamak and helical ITB plasmas are summarized in table 2. There is almost no correlation between the electron heat transport and the ion heat transport in helical plasmas, which is in contrast to the strong correlation of electron and ion heat transport in many cases in tokamak plasma. For example, only the electron heat transport or only ion heat transport or both heat transport are improved, which suggests that the simple concept of turbulence suppression by radial electric field shear can not explain the variety of ion and election heat transport or electron and impurity transport. In many cases, transport improvement is observed in all transport channels, ion heat, election heat, particle, and impurity transport in tokamak. However, only electron heat or ion heat or particle transport is improved in helical plasmas. The mechanism that causes the difference in the characteristics of ITB between tokamak plasmas and helical plasmas is open to discussion. The existence of the plasma current is the most likely reason to explain the difference in tokamak and helical plasma, because the turbulent transport is dominant rather than the neoclassical transport at the emerging of the ITB, where the feedback loop of the suppression of turbulence starts. It is also an important difference that the radial electric field is mainly determined by poloidal rotation velocity in helical plasma, while there is a significant contribution of toroidal rotation on the radial electric field in tokamak. Therefore, the coupling between toroidal rotation on the radial electric field is strong in tokamak ITB plasma but it is relatively weak in helical ITB plasma. The understanding of the physics mechanism causing the different characteristics between tokamak and helical ITB is important for improving the prospect for the simultaneous ITB formation of ion and electron heat transport and particle transport for the future device.

Table 2: Comparison of transport coupling between tokamak and helical ITB plasmas.

Transport coupling	Tokamak	Helical
χ_i and χ_e	strong correlation	no correlation
$\chi_{i,e}$ and D	strong correlation	anti-correlation
V_ϕ and E_r	strong	weak

It is also an important finding that the non-diffusive terms in momentum transport and impurity transport become more dominant in the plasma with ITB. It is an interesting question whether this is because of the decrease of the diffusive term or the change in non-diffusive term. The difference of non-diffusive terms in momentum transport between tokamak and helical ITB plasmas is summarized in table 3. The non-diffusive terms in momentum transport can be co- or counterdirection depending on the turbulence state in both tokamak and helical plasmas. Associated with the transition from L-mode plasma to ITB plasma, the toroidal rotation velocity is accelerated to the counterdirection in tokamak plasma, while it is accelerated to the codirection in helical plasma. The reversal of the sign of non-diffusive terms in momentum transport and impurity transport associated with the formation of ITB reported in helical plasma is an important finding. These results suggest that the non-diffusive terms are very sensitive to the turbulent state compared to the diffusive term. The change in non-diffusive terms can be used as a sensitive indication for the change in turbulence state when one would search for the new operation scenario with the improved confinement mode. The other important finding is the sign difference of non-diffusive term of impurity. The convention of impurity is inward and impurity accumulation is observed in most of the ITB plasma in tokamak, while it is outward and impurity hole is observed in helical plasmas. The gyro-kinetic simulation fails to explain the outward convection of impurity in helical plasma, and further theoretical work is necessary in order to explain the sign difference in the convection term of impurity in tokamak and helical plasmas.

Table 3: Comparison of non-diffusive terms inside ITB region between tokamak and helical ITB plasmas.

Non-diffusive term	Tokamak	Helical
momentum transport	counterdirection	codirection
impurity transport	inward	outward

The dynamics of ITB formation and termination have been studied in various devices both in tokamak and helical plasmas. The difference of dynamics between tokamak and helical ITB plasmas is summarized in table 4. In some discharges, the emergence location of ITB is far inside the ITB foot in the steady state phase. The ITB region shows the radial propagation during the formation of ITB. It is an interesting fact that the radial propagation of ion ITB is usually outward in tokamak plasma, while it is inward in LHD helical plasma. The physics mechanism causing this difference in the direction of radial propagation is open to question, and should be clarified in future. The outward propagation in tokamak stops at the minimum q (q_{min}) location and the ITB foot point tracks to the q_{min} location in the steady-state phase in the plasma with strong reversed magnetic shear, while it stops at rational surfaces in the plasma with positive magnetic shear. These results show the important role of minimum q and rational surface in determining the location of the ITB foot. These experimental results suggest that the role of the rational surface is not only triggering the formation of ITB but also controlling the radial propagation of ITB region and regulating the final state of formation of ITB (steady-state ITB).

Table 4: Comparison of dynamics between tokamak and helical ITB plasmas.

Dynamics	Tokamak	Helical
radial propagation during formation	outward	inward
termination in e- or ion-ITB	yes	no
termination in particle-ITB	yes	yes

The also are the differences in the termination of ITB between tokamak and helical ITB plasmas. MHD event often (but not always) triggers the termination of ion ITB in tokamak plasma, but not in helical plasma. One of the reasons for this difference is due to the fact that ion ITB plasma in helical plasma is restricted in the low β region. The particle ITB plasma with high β is often terminated by MHD event in helical plasma.

The non-local transport plays an important role in determining the radial profile of temperature and density. The finding of the spontaneous change in temperature curvature (second radial derivative of temperature) in the ITB region is important because the curvature change in the ITB region has a strong impact on the gradient near the foot point of ITB. The pressure gradient becomes significantly large (sometimes exceeding the limit for MHD stability) just inside the ITB foot in the ITB plasma with convex shape, while it can be moderate (well below the MHD limit) in the ITB plasma with concave shape. Therefore the non-local transport and the curvature of ITB is an important issue to predict the MHD limit and sustainment of high beta steady-state ITB plasmas.

The formation mechanism of ITB is much more complicated than the formation mechanism of edge transport barrier (ETB) such as H-mode. Therefore the H-mode power threshold database has been well developed, but not the ITB power threshold. This is because the heat flux at the location where the ITB is formed strongly depends on its location for the given total heating power. An analysis of the data for the formation of an ITB with dominant ion heating in different tokamaks was performed for the purpose of creating the database of ITB [196]. However, only the expression for the power required to form an ITB is given using global variables, because of the complicity of the formation mechanism of

ITB.

Here it is interesting to discuss the critical physics issues in the ITB plasmas [9]. The understanding of radial propagation of ITB is a crucial issue because the mechanism of the radial propagation of ITB region is strongly coupled with the non-local transport, which has not been well understood yet. There are many studies on how the radial electric field shear and magnetic field shear affect on the suppression of turbulence and the improvement of transport. Since there is a strong positive feedback process between the development of radial electric field shear and magnetic field shear and increase of pressure gradient due to the improvement of confinement, the understanding of each physics element is required to provide a good prospect for the property of ITB plasmas in future devices.

Acknowledgements

[1] Itoh S.I. 1992 *Phys. Fluids B* **4** 796.
[2] Hoang G.T. *et al* 2004 *Phys. Rev. Lett.* **93** 135003.
[3] Diamond P.H. *et al* 2013 *Nucl. Fusion* **53** 104019.
[4] Ida K. and Rice J.E. 2014 *Nucl. Fusion* **54** 045001.
[5] Luce T.C. *et al* 1992 *Phys. Rev. Lett.* **68** 52.
[6] Mantica P. *et al* 2000 *Phys. Rev. Lett.* **85** 4534.
[7] Fujita T. 2002 *Plasma Phys. Control. Fusion* **44** A19.
[8] Wolf R.C. 2003 *Plasma Phys. Control. Fusion* **45** R1.
[9] Litaudon X. 2006 *Plasma Phys. Contr. Fusion* **48** A1.
[10] Connor J.W. *et al* 2004 *Nucl. Fusion* **44** R1.
[11] Wagner F. *et al* 1982 *Phys. Rev. Lett.* **49** 1408.
[12] Itoh S.I. and Itoh K.1988 *Phys. Rev. Lett.* **60** 2276.
[13] Groebner R. *et al* 1990 *Phys. Rev. Lett.* **64** 3015.
[14] Ida K. *et al* 1990 *Phys. Rev. Lett.* **65** 1364.
[15] Biglari H. Diamond P.H. and Terry P.W. 1990 *Phys. Fluids B* **2** 1.
[16] Diamond P.H. *et al* 1994 *Phys. Rev. Lett.* **72** 2565.
[17] Bush C.E. *et al* 1990 *Phys. Rev. Lett.* **65** 424.
[18] Kamada Y. *et al* 1991 *Nucl. Fusion* **31** 23.
[19] Tubbing B.J.D. *et al* 1991 *Nucl. Fusion* **31** 839.
[20] Hugon M. *et al* 1992 *Nucl. Fusion* **32** 33.
[21] Levinton F.M. *et al* 1995 *Phys. Rev. Lett.* **75** 4417.
[22] Koide Y. *et al* 1994 *Phys. Rev. Lett.* **72** 3662.
[23] Bell R.E. *et al* 1998 *Phys. Rev. Lett.* **81** 1429.
[24] Bell R.E. *et al* 1998 *Plasma Phys. Control. Fusion* **40** 609.
[25] Bell R.E. *et al* 1999 *Plasma Phys. Control. Fusion* **41** A719.
[26] Mazzucato E. *et al* 1996 *Phys. Rev. Lett.* **77** 3145.
[27] Synakowski E.J. *et al* 1997 *Phys. Rev. Lett.* **78** 2972.
[28] Tala T.J.J. *et al* 2001 *Plasma Phys. Control. Fusion* **43** 507.
[29] Doyle E.J. *et al* 2002 *Nucl. Fusion* **42** 333.
[30] Sakamoto Y. *et al* 2004 *Nucl. Fusion* **44** 876.
[31] Shirai H. *et al* 2000 *Plasma Phys. Control. Fusion* **42** A109.
[32] Bundy R.V. *et al* 2002 *Plasma Phys. Control. Fusion* **44** 1215.
[33] Staebler G.M. *et al* 2016 *Phys. Plasmas* **23** 062518.
[34] Gohil P. *et al* 2003 *Nucl. Fusion* **43** 708.
[35] Cromb K. *et al* 2005 *Phys. Rev. Lett.* **95** 155003.
[36] Conway G.D. *et al* 2000 *Phys. Rev. Lett.* **84** 1463.
[37] Fujisawa A. *et al* 2006 *Plasma Phys. Control. Fusion* **48** S205.
[38] Diamond P.H. and Hahm T.S. 1995 *Phys. Plasmas* **2** 3640.
[39] Diamond P.H. *et al* 1997 *Phys. Rev. Lett.* **78** 1472.
[40] Shaing K.C. *et al* 1999 *Phys. Rev. Lett.* **83** 3840.
[41] Hidalgo C. *et al* 2000 *Plasma Phys. Contr. Fusion* **42** A153.
[42] Fujisawa A. *et al* 2004 *Phys. Rev. Lett.* **93** 165002.
[43] Diamond P.H. *et al* 2005 *Plasma Phys. Control. Fusion* **47** R35.
[44] Itoh K. *et al* *Phys. Plasmas* **14** 020702.
[45] Fujisawa A. *et al* 2007 *J. Phys. Soc. Jpn.* **76** 033501.
[46] Fujisawa A. 2009 *Nucl. Fusion* **49** 013001.
[47] Kamiya K. *et al* 2016 *Sci. Rep.* **6** 30585.
[48] Garofalo A.M. *et al* 2015 *Nucl. Fusion* **55** 023025.
[49] Pan C. *et al* 2017 *Nucl. Fusion* **57** 036018.
[50] Ding S. *et al* 2017 *Phys. Plasmas* **24** 056114.
[51] Joffrin E. *et al* 2002 *Plasma Phys. Control. Fusion* **44** 1203.
[52] Challis C.D. *et al* 2001 *Plasma Phys. Control. Fusion* **43** 861.
[53] Challis C.D. *et al* 2002 *Plasma Phys. Control. Fusion* **44** 1031.
[54] Joffrin E. *et al* 2002 *Plasma Phys. Control. Fusion* **44** 1739.
[55] Joffrin E. *et al* 2002 *Nucl. Fusion* **42** 235.
[56] Kamada Y. *et al* 2002 *Fusion Sci. Tech.* **42** 185.
[57] Yu D.L. *et al* 2016 *Nucl. Fusion* **56** 056003.
[58] Chung J. *et al* 2017 *Nucl. Fusion* **57**
[59] Joffrin E. *et al* 2003 *Nucl. Fusion* **43** 1167.
[60] Austin M.E. *et al* 2006 *Phys. Plasmas* **13** 082502.
[61] Waltz R.E. *et al* 2006 *Phys. Plasmas* **13** 052301.
[62] Parail V.V. *et al* 1999 *Nucl. Fusion* **39** 429.
[63] Sakamoto Y. *et al* 2001 *Nucl. Fusion* **41** 865.
[64] Kishimoto Y. *et al* 1998 *Plasma Phys. Control. Fusion* **40** A663.
[65] Kishimoto Y. *et al* 2000 *Nucl. Fusion* **40** 667.
[66] Firpo N.-C. *et al* 2011 *Phys. Plasmas* **18** 032506.
[67] Neudatchin Y. *et al* 2004 *Nucl. Fusion* **44** 945.
[68] Greenfield Y. *et al* 1999 *Nucl. Fusion* **39** 1713.
[69] Ida K.. *et al* 1986 *Plasma Phys. Control. Fusion* **28** 879.
[70] Weller A. *et al* 1987 *Phys. Rev. Lett.* **59** 2303.
[71] Ida K. *et al* 2012 *Phys. Rev. Lett.* **109** 065001.
[72] Bardóczi L. *et al* 2016 *Phys. Plasmas* **23** 052507.
[73] Bardóczi L. *et al* 2016 *Phys. Rev. Lett.* **116** 215001.
[74] Inagaki S. *et al* 2004 *Phys. Rev. Lett.* **92** 055002.
[75] Ida K. *et al* 2015 *Sci. Rep.* **5** 16165.
[76] Ida K. *et al* 2004 *Phys. Plasmas* **11** 2551.
[77] Rice B.W. *et al* 1996 *Plasma Phys. Contr. Fusion* **38**

869.
[78] Fujita T. *et al* 2001 *Phys. Rev. Lett.* **87** 085001.
[79] Politzer P.A. *et al* 2005 *Nucl. Fusion* **45** 417.
[80] Sakamoto Y. *et al* 2007 *Nucl. Fusion* **47** 1506.
[81] Litaudon X. *et al* 1996 *Plasma Phys. Contr. Fusion* **38** 1603.
[82] Ide S. *et al* 2000 *Nucl. Fusion* **40** 445.
[83] Baranov Yu. F. *et al* 2005 *Plasma Phys. Contr. Fusion* **47** 975.
[84] Tala T. *et al* 2006 *Nucl. Fusion* **46** 548.
[85] Cataldo C. *et al* 2002 *Phys. Plasmas* **9** 3205.
[86] Fujita T. *et al* 1997 *Phys. Rev. Lett.* **78** 2377.
[87] Fujita T. *et al* 2004 *Plasma Phys. Contr. Fusion* **46** A35.
[88] Goddman T.P. *et al* 2005 *Plasma Phys. Contr. Fusion* **47** B107.
[89] Ida K. *et al* 2004 *Plasma Phys. Contr. Fusion* **46** A45.
[90] Inagaki S. *et al* 2006 *Nucl. Fusion* **46** 133.
[91] Fujisawa A. *et al* 1999 *Phys. Rev. Lett.* **82** 2669.
[92] Ida K. *et al* 2003 *Phys. Rev. Lett.* **91** 085003.
[93] Shimozuma T. *et al* 2003 *Plasma Phys. Contr. Fusion* **45** 1183.
[94] Takeiri Y. *et al* 2003 *Phys. Plasmas* **10** 1788.
[95] Estrada T. *et al* 2004 *Plasma Phys. Contr. Fusion* **46** 277.
[96] Takahashi H. *et al* 2014 *Phys. Plasmas* **21** 061506.
[97] Nagaoka K. *et al* 2015 *Nucl. Fusion* **55** 113020.
[98] Tsujimura T.Ii *et al* 2015 *Nucl. Fusion* **55** 123019.
[99] Kenmochi N. *et al* 2017 *Plasma Phys. Contr. Fusion* **59** 055013.
[100] Stroth U. *et al* 2001 *Phys. Rev. Lett.* **86** 5910.
[101] Minami T. *et al* 2002 *Plasma Phys. Contr. Fusion* **44** A197.
[102] Minami T. *et al* 2004 *Plasma Phys. Contr. Fusion* **46** A285.
[103] Minami T. *et al* 2004 *Nucl. Fusion* **44** 342.
[104] Yokoyama M. *et al* 2007 *Nucl. Fusion* **47** 1213.
[105] Velasco J.L. *et al* 2008 *Nucl. Fusion* **48** 065008.
[106] Inagaki S. *et al* 2004 *Plasma Phys. Contr. Fusion* **46** A71.
[107] Lorenzin R. *et al* 2009 *Nat. Phys.* **5** 570.
[108] Puiatti M.E. *et al* 2011 *Nat. Phys.* **51** 073038.
[109] Lorenzin R. *et al* 2012 *Nucl. Fusion* **52** 062004.
[110] Rice B.W. *et al* 1996 *Phys. Plasmas* **3** 1983.
[111] Hoang G.T. *et al* 2000 *Phys. Rev. Lett.* **84** 4593.
[112] Chechkin V.V. *et al* 2006 *Plasma Phys. Contr. Fusion* **48** A241.
[113] Zushi H. *et al* 2005 *Nucl. Fusion* **45** S142.
[114] Mailloux J. *et al* 2002 *Phys. Plasmas* **9** 2156.
[115] Garofalo A.M. *et al* 2006 *Phys. Plasmas* **13** 056110.
[116] Takahashi H. *et al* 2013 *Nucl. Fusion* **52** 073034.
[117] Ida K. *et al* 1991 *Phys. Rev. Lett.* **67** 58.
[118] Ida K. *et al* 1997 *Phys. Plasmas* **4** 310.
[119] Nagaoka K. *et al* 2011 *Nucl. Fusion* **51** 083022.
[120] Ida K. *et al* 2013 *Phys. Rev. Lett.* **111** 055001.
[121] Gruber O. *et al* 1999 *Phys. Rev. Lett.* **83** 1787.
[122] Wolf R.C. *et al* 1999 *Plasma Phys. Contr. Fusion* **41** B93.
[123] Greenfield C.M. *et al* 1997 *Phys. Plasmas* **4** 1596.
[124] Meyer H. *et al* 2004 *Plasma Phys. Contr. Fusion* **46** A291.
[125] Koide Y. *et al* 1998 *Plasma Phys. Contr. Fusion* **40** 641.
[126] Fujita T. *et al* 1999 *Nucl. Fusion* **39** 1627.
[127] Kamada Y. *et al* 2002 *Plasma Phys. Contr. Fusion* **44** A279.
[128] Turnbull A.D. *et al* 1995 *Phys. Rev. Lett.* **74** 718.
[129] Strait E.J. *et al* 1994 *Phys. Plasmas* **1** 1415.
[130] Strait E.J. *et al* 1997 *Phys. Plasmas* **4** 1783.
[131] Doyle E.J. *et al* 2001 *Plasma Phys. Contr. Fusion* **43** A95.
[132] Rice J.E. *et al* 2002 *Nucl. Fusion* **42** 510.
[133] Kamiya K. *et al* 2004 *Plasma Phys. Contr. Fusion* **46** A157.
[134] Gormezano C. *et al* 1998 *Phys. Rev. Lett.* **80** 5544.
[135] Scott S.D. *et al* 1995 *Phys. Plasmas* **2** 2299.
[136] Ernst D.R. *et al* 2004 *Phys. Plasmas* **11** 2637.
[137] Nunami M. *et al* 2012 *Phys. Plasmas* **19** 042504.
[138] Maget P. *et al* 1999 *Nucl. Fusion* **39** 949.
[139] Takase Y. *et al* 1997 *Phys. Plasmas* **4** 1647.
[140] Baylor L.R. *et al* 2000 *Phys. Plasmas* **7** 1878.
[141] Fiore C.L. *et al* 2001 *Phys. Plasmas* **8** 2023.
[142] Efthimion P.C. *et al* 1998 *Phys. Plasmas* **5** 1832.
[143] Ohyabu N. *et al* 2006 *Phys. Rev. Lett.* **97** 055002.
[144] Ohyabu N. *et al* 2006 *Plasma Phys. Contr. Fusion* **48** B383.
[145] Morisaki T. *et al* 2007 *Phys. Plasmas* **14** 056113.
[146] Yang Y. *et al* 2017 *Plasma Phys. Contr. Fusion* **59** 085003.
[147] Gao X. *et al* 2017 *Nucl. Fusion* **57** 056021.
[148] Eriksson L.-G. *et al* 2002 *Phys. Rev. Lett.* **88** 145001.
[149] Romanelli M. *et al* 2010 *Plasma Phys. Contr. Fusion* **52** 045007.
[150] Bourdelle C. *et al* 2002 *Nucl. Fusion* **42** 892.
[151] Eriksson L.-G. *et al* 1993 *Nucl. Fusion* **33** 1037.
[152] Zhurovich K. *et al* 2007 *Nucl. Fusion* **47** 1220.
[153] Tala T.J.J. *et al* 2002 *Plasma Phys. Contr. Fusion* **44** A495.
[154] Newman D.E. *et al* 1998 *Phys. Plasmas* **5** 938.
[155] Staebler G.M. *et al* 1998 *Plasma Phys. Contr. Fusion* **40** 569.
[156] Dong J.Q. *et al* 2004 *Phys. Plasmas* **11** 5673.
[157] Fukuyama A. *et al* 2000 *Nucl. Fusion* **40** 685.
[158] Gohil P. *et al* 2002 *Plasma Phys. Contr. Fusion* **44** A37.
[159] Mantica P. *et al* 2002 *Plasma Phys. Contr. Fusion* **44** 2185.
[160] Koide Y. *et al* 1996 *Plasma Phys. Contr. Fusion* **38** 1011.
[161] Esposito B. *et al* 2003 *Plasma Phys. Contr. Fusion* **45** 933.
[162] Ida K. *et al* 2009 *Nucl. Fusion* **49** 095024.
[163] Ida K. *et al* 2010 *Contrib. Plasma Phys.* **50** 558.
[164] Tresset G. *et al* 2002 *Nucl. Fusion* **42** 520.
[165] Neidatchin S.V. *et al* 1999 *Plasma Phys. Contr. Fusion* **41** L39.
[166] Neudatchin S.V. *et al* 2001 *Plasma Phys. Contr. Fusion* **43** 661.
[167] Ida K. *et al* 2009 *Nucl. Fusion* **49** 015005.
[168] Ida K. *et al* 2015 *Nucl. Fusion* **55** 013022.
[169] Rice B.W. *et al* 1999 *Nucl. Fusion* **39** 1855.
[170] Bécoulet A. *et al* 2000 *Nucl. Fusion* **40** 1113.
[171] Hender T.C. *et al* 2002 *Plasma Phys. Contr. Fusion* **44** 1143.
[172] Sarazin Y. *et al* 2002 *Plasma Phys. Contr. Fusion* **44** 2445.
[173] Ding S. *et al* 2017 *Nucl. Fusion* **57** 022016.
[174] Shiraiwa S. *et al* 2013 *Nucl. Fusion* **53** 113028.
[175] Tardini G. *et al* 2007 *Nucl. Fusion* **47** 280.
[176] Gürcan O.D. Diamond P.H. and Hahm T.S. 2008 *Phys. Rev. Lett.* **100** 135001.

[177] Solomon W.M. *et al* 2009 *Nucl. Fusion* **49** 085005.
[178] McDermott R.M. *et al* 2011 *Plasma Phys. Control. Fusion* **53** 035007.
[179] McDermott R.M. *et al* 2011 *Plasma Phys. Control. Fusion* **53** 124013.
[180] Ida K. *et al* 1995 *Phys. Rev. Lett.* **74** 1990.
[181] Ida K. *et al* 1998 *J. Phys. Soc. Japan* **67** 4089.
[182] Yoshida M. *et al* 2008 *Phys. Rev. Lett.* **100** 105002.
[183] Rice J.E. *et al* 2001 *Nucl. Fusion* **41** 277.
[184] Rice J.E. *et al* 2003 *Nucl. Fusion* **43** 781.
[185] Lee W.D. *et al* 2003 *Phys. Rev. Lett.* **91** 205003.
[186] Rice J.E. *et al* 2004 *Nucl. Fusion* **44** 379.
[187] Fiore C.L. *et al* 2010 *Nucl. Fusion* **50** 064008.
[188] Ida K. *et al* 2010 *Nucl. Fusion* **50** 064007.
[189] Yoshinuma M. *et al* 2009 *Nucl. Fusion* **49** 075036.
[190] Carraro L. *et al* 2004 *Plasma Phys. Contr. Fusion* **46** 389.
[191] Takenaga H. *et al* 2006 *Fusion Sci. Technol.* **50** 503.
[192] Rice J.E. *et al* 2007 *Fusion Sci. Technol.* **51** 357.
[193] Rowan W.L. *et al* 2008 *Nucl. Fusion* **48** 105005.
[194] Challis C.D. *et al* 2004 *Plasma Phys. Contr. Fusion* **46** B23.
[195] Takenaga H. *et al* 2005 *Nucl. Fusion* **45** 1618.
[196] Sips A.C.C. *et al* 2002 *Plasma Phys. Contr. Fusion* **44** B69.
[197] Neu R. *et al* 2002 *Plasma Phys. Contr. Fusion* **44** 811.
[198] Leonov V.M. *et al* 2005 *Plasma Phys. Contr. Fusion* **47** 903.
[199] Neu R. *et al* 2005 *Nucl. Fusion* **45** 209.
[200] Dux R. *et al* 2004 *Nucl. Fusion* **44** 260.
[201] Dix R. *et al* 2003 *J. Nucl. Mater.* **313-316** 1150.
[202] Ida K. *et al* 1987 *Phys. Rev. Lett.* **58** 116.
[203] Guirlet R. *et al* 2006 *Plasma Phys. Contr. Fusion* **48** B63.
[204] Takenaga H. *et al* 2003 *Nucl. Fusion* **43** 1235.
[205] Kubo H. *et al* 2003 *J. Nucl. Mater.* **313-316** 1197.
[206] Wade M.R. *et al* 2000 *Phys. Rev. Lett.* **84** 282.
[207] Ridulfini V. *et al* 2003 *Nucl. Fusion* **43** 469.
[208] Seguin K. *et al* 1983 *Phys. Rev. Lett.* **51** 455.
[209] Jahns G.L. *et al* 1982 *Nucl. Fusion* **22** 1049.
[210] Crisanti F. *et al* 2002 *Phys. Rev. Lett.* **88** 145004.
[211] Yoshinuma M. *et al* 2093 *Nucl. Fusion* **49** 062002 .
[212] Ida K. *et al* 2009 *Phys. Plasmas* **16** 056111.
[213] Ido T. *et al* 2010 *Plasma Phys. Contr. Fusion* **52** 124025.
[214] Mikkelsen D.R. *et al* 2014 *Phys. Plasmas* **21** 082302.
[215] Yoshinuma M. *et al* 2015 *Nucl. Fusion* **55** 083017.
[216] Futatani S. *et al* 2010 *Phys. Rev. Lett.* **104** 015003.
[217] Cordey J.G. *et al* 1994 *Plasma Phys. Contr. Fusion* **36** A267.
[218] Cordey J.G. *et al* 1995 *Nucl. Fusion* **35** 505.
[219] Parail V.V. *et al* 1997 *Nucl. Fusion* **37** 481.
[220] Minardi E. *et al* 1996 *J. Phys. Soc. Jpn.* **67** 1891.
[221] Callen J.D. *et al* 1997 *Plasma Phys. Contr. Fusion* **39** B173.
[222] Neudatchin S.V. *et al* 2002 *Plasma Phys. Contr. Fusion* **44** A383.
[223] Ide S. *et al* 2007 *Nucl. Fusion* **47** 1499.
[224] Yoshinuma M. *et al* 2010 *Fusion. Sci. Technol.* **58** 375.
[225] Ida K. *et al* 2008 *Phys. Sci. Instrum.* **79** 053506.
[226] Ida K. *et al* 2008 *Phys. Rev. Lett.* **101** 055003.
[227] Litaudon X. *et al* 2003 *Nucl. Fusion* **43** 565.
[228] Litaudon X. *et al* 2011 *Fusion. Sci. Technol.* **59** 469.
[229] Garcia J. and Giruzzi G. 2012 *Plasma Phys. Contr. Fusion* **54** 015009.
[230] Bizarro J.P.S. *et al* 2007 *Nucl. Fusion* **47** L41.
[231] Chu M.S. *et al* 1996 *Phys. Rev. Lett.* **77** 2710.
[232] Ishida S. *et al* 1997 *Phys. Rev. Lett.* **79** 3917.
[233] Ozeki T. *et al* 1998 *Plasma Phys. Contr. Fusion* **40** 871.
[234] Zohm H. *et al* 2007 *Nucl. Fusion* **47** 228.
[235] Riccardo V. *et al* 2003 *Plasma Phys. Contr. Fusion* **45** A269.
[236] Riccardo V. *et al* 2005 *Nucl. Fusion* **45** 1427.
[237] Paley J.I. *et al* 2005 *J. Nucl. Mater.* **337-339** 702.
[238] Takeji S. *et al* 2002 *Nucl. Fusion* **42** 5.
[239] Takeji S. *et al* 1997 *Phys. Plasmas* **4** 4283.
[240] Tokunaga S. *et al* 2009 *Nucl. Fusion* **49** 075023.
[241] Sakamoto Y. *et al* 2009 *Nucl. Fusion* **49** 095017.
[242] Gormezano C. 1999 *Plasma Phys. Contr. Fusion* **41** B367.
[243] Sakamoto Y. *et al* 2005 *Nucl. Fusion* **45** 574.
[244] Fujita T. 2000 *J. Plasma Fusion Res. Series* **3** 87.
[245] Cesario R. *et al* 2004 *Phys. Rev. Lett.* **92** 175002.
[246] Takei N. *et al* 2007 *Plasma Phys. Contr. Fusion* **49** 335.
[247] Ide S. *et al* 2002 *Plasma Phys. Contr. Fusion* **44** A137.
[248] Ide S. *et al* 2004 *Nucl. Fusion* **44** 87.
[249] Takahashi H. *et al* 2017 *Nucl. Fusion* **57** 086029.
[250] Yoshida M. *et al* 2017 *Nucl. Fusion* **57** 056027.